

Room-Temperature Synthesis and Characterization of Highly Monodisperse Transition Metal-Doped ZnO Nanocrystals

by

Adrian G. Parra Palomino

Thesis submitted in partial fulfillment of the requirements for the degree of

MASTER OF SCIENCE

In

PHYSICS

**UNIVERSITY OF PUERTO RICO
MAYAGÜEZ CAMPUS
2006**

Approved by:

Oscar Perales Pérez, PhD
President, Graduate Committee

Date

Maharaj S. Tomar, PhD
Member, Graduate Committee

Date

Héctor Jiménez PhD
Member, Graduate Committee.

Date

Héctor Jiménez PhD
Chairperson of the Department

Date

Silvestre Colon PhD
Representative of Graduate Studies

Date

ABSTRACT

Recent experimental verifications of predicted intrinsic room-temperature ferromagnetism in transition metal doped-ZnO nanostructures have increased their attractiveness as promising candidates for optoelectronic and spintronics-based devices. A control over dopant speciation and the determination of the size-dependence of functional properties at the nanoscale become then indispensable. We present here the results of our current efforts on size-controlled synthesis of bare and TM-doped ZnO nanocrystals. Stable suspensions of these materials were produced in ethanol solutions at room-temperature. XRD characterization of produced materials verified the fast and direct formation of ZnO nanocrystals after 10 minutes of contact time at room-temperature. Although the actual incorporation of TM atoms into the ZnO host structure was also evidenced by the XRD analyses, the presence of dopant ions in starting solutions delayed the formation of the oxide. Well-crystallized doped ZnO structures were produced only after aging of the nanocrystals in their mother liquors at ambient temperature. The length of this aging period was found to be dependent on the fraction of TM in the solids. HRTEM analyses of the suspensions revealed the high monodispersity and crystallinity of the 6-9 nm nanocrystals. UV-visible measurements confirmed not only the nanocrystalline nature of the samples but also evidenced the continuous growth of the nanocrystals when aged in their mother liquors. UV-visible analyses also confirmed the inhibition of crystal growth when the nanocrystals were coagulated by n-heptane and redispersed in fresh ethanol solutions. The application of this coagulation-redispersion process at different aging times allowed the production of highly monodisperse nanocrystals of different mean size. SQUID measurements indicated that doped ZnO nanocrystals were paramagnetic or ferromagnetic at room-temperature in contrast with the diamagnetic nature of bare ZnO.

This work is dedicated to God, to my wonderful parents Henry and Elizabeth who formed part of my vision and taught me the good things that really matter in life. I am grateful for my five brothers Marcelo, Henriko, Leonardo, Juvenal and Diana, for rendering me the sense and the value of brotherhood. I am glad to be one of them.

ACKNOWLEDGEMENTS

This thesis is the result of one and half years of work whereby I have been accompanied and supported by many people. It is a pleasant aspect that I have now the opportunity to express my gratitude for all of them.

The first person I would like to thank is my direct supervisor Dr. Oscar Perales. During these years I have known to him as a sympathetic and principle-centered person. His overly enthusiasm and integral view on research and his mission for providing 'only high-quality work and not less', has made a deep impression on me. I owe him lots of gratitude for having me shown this way of research. Besides of being an excellent supervisor was as close as a relative and a good friend to me. I thank you all.

I would like to thank to Dr. Maharaj Tomar for give me the opportunity to work with this excellent group of investigation. I would like to thank to Dr. Hector Jimenez who also has monitored my work and took effort in reading and providing me with valuable comments on earlier versions of this thesis.

I would especially like to thank to Sandra Liliana Dussan to share and to offer support and I animate in all these years in special in this stage of my life. Finally, I would like to thank all whose direct and indirect support helped me completing my thesis in time.

This research has been supported and funded by various organizations including IDEAS-NASA (Grant NCC55-595PR NASA-EPSCoR), NSF-EPSCoR (Grant EPS-0223152; CFDA # es 47.076), and NSF-PREM. I would also like to thank to Dr. Paul Voyles of the Department of Materials Science at University of Wisconsin Madison for the TEM pictures.

TABLE OF CONTENTS

ABSTRACT	ii
TABLE LIST	vii
FIGURE LIST	viii
CHAPTER 1. INTRODUCCION.....	1
1.1 MOTIVATION	1
1.2 OBJECTIVES	7
1.3 SUMMARY OF THIS THESIS	7
CHAPTER 2. BACKGROUND	8
2.1 SPINTRONICS	8
2.2 SPINTRONICS DEVICES	9
2.2.1 Magnetic Tunnel Junction and MRAM	11
2.2.2 Spin FET:.....	12
2.2.3 Spin LED.....	14
2.3 DILUTED MAGNETIC SEMICONDUCTORS (DMS).....	15
2.4 OXIDE-BASED SEMICONDUCTORS.....	21
2.4.1 ZnO- based DMS	21
i) Mn- doped ZnO.....	24
ii) Co- Doped ZnO.....	27
iii) Other TM- doped ZnO systems.....	29
2.4.2 TiO ₂ – based DMSs'	30
CHAPTER 3. EXPERIMENTAL	32
3.1. MATERIALS	32
3.2. SYNTHESIS OF BARE ZnO AND TM ²⁺ DOPED ZnO NANOCRYSTALS..	32
.....	32
3.3 CHARACTERIZATION TECHNIQUES.....	33
CHAPTER 4. RESULTS AND DISCUSSION	35
4.1 XRD CHARACTERIZATION.....	35

4.1.1 Bare ZnO nanocrystals	35
4.1.2 TM- doped ZnO nanocrystals, (TM = Mn, Co, Ni, Cu, Fe).....	37
4.2 HRTEM ANALYSES OF SYNTHESIZED NANOCRYSTALS	52
4.3 FT-IR MEASUREMENTS	55
4.3.1 FT-IR measurements for bare ZnO nanocrystals.....	55
4.3.2 Doped ZnO nanocrystals	57
<i>i) Effect of type of dopant.....</i>	<i>57</i>
<i>ii) Effect of aging time: the case of Mn-ZnO</i>	<i>57</i>
4.4 ULTRAVIOLET-VISIBLE ABSORPTION SPECTROSCOPY	60
4.4.1 Crystal growth monitoring.	60
4.4.2 Excitonic properties and the Bohr radius	68
4.5 SQUID CHARACTERIZATION	75
4.5.1 M-H measurement for bare ZnO nanocrystals.....	76
4.5.2 M-H measurement for doped ZnO nanocrystals	77
<i>i) Mn-doped ZnO nanocrystals</i>	<i>77</i>
<i>ii) Co- doped ZnO (x=0.01, 0.02).....</i>	<i>78</i>
<i>iii) Ni- doped ZnO (x=0.02).....</i>	<i>82</i>
<i>iv) Cu- doped and Fe- doped ZnO nanocrystals.....</i>	<i>84</i>
4.5.3 ZFC/FC for Mn- doped ZnO nanocrystals.....	87
CHAPTER 5. CONCLUSIONS.....	94
6. REFERENCES	96

TABLE LIST

Table 1. Average crystallite size of bare ZnO nanocrystals synthesized at different aging times.....	36
Table 2. Average crystallite size at different nominal Mn fraction, 'x', in ZnO and 24 hours of aging.	41
Table 3. Average crystallite size for Co- doped ZnO for different 'x' values and aging time of 24 hours.	43
Table 4. Average crystallite size for of Ni- doped ZnO for different 'x' values and 144 hours of aging.	46
Table 5. Average crystallite size of Fe- doped ZnO for different 'x' values and 30 minutes of aging.....	46
Table 6. Average crystallite size of Cu- doped ZnO for different 'x' values and aging time of 30 minutes.....	47
Table 7. Estimated band gap energies and corresponding nanocrystal sizes as a function of aging time. A marked decrease in confinement energy by increasing particle size became evident.....	63
Table 8. Calculated Excitonic Bohr Radii for Various Materials.....	71
Table 9. Curie-Weiss parameter determined from $\frac{I}{\chi}$ vs. T curves for Mn-doped ZnO nanocrystals. The applied field was 100 Oe.....	92

FIGURE LIST

Figure 1. Three type of semiconductors: (A) a magnetic semiconductor, in which a periodic array of element is present; (B) a nonmagnetic semiconductor, which no contain magnetic ions; (B) a dilute magnetic semiconductor and magnetic element.....	4
Figure 2. GMR structure	10
Figure 3. Schematic representation of a MRAM with MTJ.	12
Figure 4. Scheme of the Datta-Das spin field-effect transistor (SFET)	13
Figure 5. A schematic spin LED	14
Figure 6. Estimated values of the Curie temperature T_c for various p-type semiconductors containing 5% of Mn and 3.5×10^{20} holes per cm^3 [16, 26].....	17
Figure 7. Stability of the ferromagnetic states in (a) ZnO-, (b) ZnS-, (c) ZnSe- and (d) ZnTe-based DMSs. V, Cr, Mn, Fe, Co or Ni is doped as a magnetic impurity. The vertical axis is the energy difference per formula unit between the ferromagnetic state and the spin-glass state. A positive energy difference indicates that the ferromagnetic state is more stable than the spin-glass state [28].....	19
Figure 8. Stability of the ferromagnetic state in (a) GaAs- and (b) GaN-based DMSs	20
Figure 9. a) Schematic representation of a wurtzite ZnO structure having lattice constant a in the basal plane and c along the basal direction. b) Tetrahedral coordination. In each atoms of Zinc is surrounded by four cations of oxygen at the corners of a tetrahedron and vice versa.....	22
Figure 10. Flow chart of synthesis procedure of ZnO nanocrystals.....	34
Figure 11. XRD patterns for bare ZnO synthesized at different aging times. All peaks correspond to ZnO wurtzite structure. ZnO was rapidly formed even right after 10 minutes of mixing without aging. The broadness of the XRD peaks reveals the nanocrystalline nature of the ZnO powders. The average crystallite size was estimated to be ~ 6 nm after 24 hours of aging using Scherrer's equation.	35

Figure 12. XRD of Mn- doped ZnO nanocrystals synthesized at different 'x' values (where 'x' is the nominal Mn fraction in starting solutions) and 30 minutes of aging at room temperature. The XRD spectra evidenced that an increase in the 'x' value delayed the formation of the ZnO host structure. The solid produced for $x = 0.08$ consisted of incipient ZnO coexisting with the precursor compound, for which XRD peaks are identified with a mark. The precursor compound can be considered to be $Zn(OH)_2$ or a basic Zn acetate.38

Figure 13. X-ray diffraction patterns of Mn- doped ZnO synthesized at different 'x' values and 24 hours of aging at room temperature. The complete formation of the wurtzite structure was achieved only after prolonging aging time. The XRD pattern of bulk ZnO is included only for comparison.39

Figure 14. XRD patterns for Mn- doped ZnO nanocrystals synthesized at different aging times. The complete development of the host ZnO structure took place after 24 hours of aging for $x = 0.08$. For shorter aging times, incipient ZnO coexisted with precursor basic Zn acetate (XRD peaks are identified with arrows).....40

Figure 15. XRD patterns for Co- doped ZnO synthesized at different nominal atomic fractions of Co, 'x', and 24 hours of aging. Bare ZnO was formed even with no need of aging. However, a delay on the formation of host ZnO was observed when Co (II) ions were contained in starting solutions ('x' is the fraction of dopant ions in starting solutions). The precursor compound (indicated by arrows) co-existed with ZnO for $x = 0.08$ even after 24 hours of aging.42

Figure 16. The delay in the complete conversion of the intermediate (black arrows) into ZnO host was even longer for $x=0.08$. Incipient ZnO coexisted with the intermediate even after 48 hours of aging at room temperature.42

Figure 17. XRD patterns of Ni- doped ZnO nanocrystals synthesized at different 'x' values and aging times. The ZnO host structure was delayed when 'x' was increased. The complete formation of the wurtzite structure no achieved after prolonging aging (6 day). For higher 'x' values, longer aging time required to fully develop the zinc oxide structure.....44

Figure 18. XRD patterns of Fe- doped ZnO nanocrystals synthesized at different 'x' values and aging times. The complete formation of the Fe- doped ZnO wurtzite structure took place even after an aging time as short as 30 minutes. The formation of intermediate phases was not evidenced for this time of aging. 45

Figure 19. XRD patterns for Cu- doped ZnO synthesized at different 'x' values and aging times. The formation of intermediate phases was not evidenced for this time of aging.....45

Figure 20. Lattice parameters a and c for wurtzite phase determined from XRD patterns for TM-doped ZnO nanocrystals. Lattice parameters for bare ZnO were $a = 3.250 \text{ \AA}$ and $c = 5.20 \text{ \AA}$.	48
Figure 21. HRTEM micrograph of ZnO nanocrystals produced after 20 minutes of aging time. The picture evidenced the high monodispersity of the 5-8 nm nanocrystals.	52
Figure 22. HRTEM pictures of 24 hours-aged Mn- doped ZnO ($x=0.05$) nanocrystals. The high monodispersity is also observed in the 3-5nm particles.	53
Figure 23. HRTEM micrograph evidences the highly crystalline nature of a single ZnO crystal; the lattice image can be clearly observed.	54
Figure 24. The high monodispersity exhibited by bare and doped-ZnO nanocrystals can be attributed to the acetate species strongly adsorbed on the surface of the nanocrystals.	56
Figure 25. FT- IR spectra of two types of zinc acetate.	56
Figure 26. a) FT-IR spectra ZnO nanoparticles. b) FT-IR measurement of TM- doped ZnO. The presence of acetate species coexisted even after intense washed for bare and TM- doped ZnO.	58
Figure 27. FT-IR spectra of Mn- doped ZnO nanocrystals ($x = 0.08$) synthesized at different aging times. As seen, prolonged aging favored the development of the ZnO structure. The bands of acetate species were detected even after intensive washing of the solids, suggesting the acetate is present as adsorbed species.	59
Figure 28 (a) and (b). ZnO absorption spectra taken at various aging time. Red-shift in the absorption pick was observed between interval time 0 minutes and 24 hours (the change between two absorption position pick was $E=0.249 \text{ eV}$), which indicated a fast particle growth for early stage of formation of the nanocrystals.	62
Figure 29. UV-visible analyses confirmed the inhibition of crystal growth when the ZnO nanocrystals were rapidly coagulated by n-heptane and redispersed in fresh ethanol solutions.	64
Figure 30 a. UV-Vis spectra absorption spectra of suspension of TM- doped ZnO nanocrystals for a dopant atomic fraction of 1% and 24 hours of aging.	65
Figure 30 b. Variation of band gap with aging time in TM- doped ZnO nanocrystals. Large energy gap was observed as a consequence direct from the	

strong quantum confinement of the electron due to the reduced particle size. After of 24 hours of aging an abrupt change in the optical band gap to lower energy was observed for all systems. This change correspond to a blue shift with respect to the energy of the bulk material, which can be attributed to the slowly growth of the particle.....65

Figure 31. Variation of band gap with the percentage of TM doping in nanocrystals.....67

Figure 32. Representation of the gradual change of the electronic properties when the size of a semiconductor decreases (from left to right). The left correspond the energy band diagram for a microcrystalline semiconductor. The middle picture, the size of the semiconductor is comparable to the size of the exciton while the picture of the right represents the situation when de dimensions of the semiconductor are smaller than those of the exciton.72

Figure 33. The quantum size confinement can be qualitatively understood like a particle-in-a-box, the energy levels spacing decreases with increasing box size. Therefore, as the number of atoms increase from a single atom or molecule to a cluster o particle of atom and finally bulk solid, the special size of the system increases and the energy level spacing decreases.....73

Figure 34. Components of SQUID ("Superconducting Quantum Interference Device") Quantum Design MPMS ("Magnetic Property Measurement System") Model XL576

Figure 35. *M vs H* curves measured at 2 K and 300 K temperatures for bare ZnO nanocrystals.....77

Figure 36. *M-H* curves at room temperature of Mn- doped ZnO nanocrystals. A linear paramagnetic behavior is observed, which could be attributed to the incorporation of the Mn atoms.78

Figure 37. Room temperature *M-H* loop for as-synthesized Co-doped ZnO nanocrystals ($x = 0.01$, 30 min aging) at 300 K. The inset is a magnification of figure at the origin showing a small hysteresis, which suggests a weak ferromagnetism at room temperature.....80

Figure 38. Room temperature *M-H* loop for Co-doped ZnO sample ($x=0.02$). The inset shows the *M-H* plot at the origin. Hysteresis is clearly observed in this curve at low magnetic fields.....80

Figure 39. Room-temperature *M-H* curve for Ni- doped ZnO ($x=0.02$). Hysteresis is clearly observed at low magnetic fields.83

Figure 40. Room temperature M-H loops of Cu- doped ZnO ($x= 0.05$ and 0.08) aged for 24 hours and 96 hours, respectively.86

Figure 41. Room temperature M-H loop for Fe- doped ZnO ($x=0.1$). The inset shows the M-H data around the origin.86

Figure 42. a) Magnetization versus Temperature curve for Mn- doped ZnO nanocrystals synthesized at different 'x' values and 100 Oe of external applied field; b) M vs T and $1/\chi$ vs T curves. The solid lines represent the fitting using the Curie-Weiss' law.89

Figure 43. The inverse of χ as a function of T for systems exhibiting Curie ($\chi = C/T$) and Curie-Weiss behavior ($\chi = C/(T - \theta)$). When $\theta > 0$ the interaction between moment helps to align neighboring moment in the same direction and when $\theta < 0$ moment are aligned in opposite directions. When $\theta = 0$ the moment act completely independent of one another.91

1. INTRODUCCION

1.1 MOTIVATION

Recently many investigations have been oriented to the study of the material at nano-scale. But to begin, what is nano? Without provide a definitive answer to this question nano is a popular (emergent) area of science and technology today. It has attracted of attention of research of the entire world. Today the word nano describes physical length scales that are on the order of a billionth of a meter of long.

The continuous interest by the nanomaterials is due to the infinite possibilities that they can offer when they are manipulated on atoms scale such as or molecules. The interest of these materials is that represent several mechanical and chemical unique properties, very different in comparison with material of the micrometer size and the same composition. In this respect different areas like physics, chemistry, biology and engineering, tried to give explanation to many phenomenon that these material exhibit.

In the past years the material science consisted basically in utilize the elements that the nature provide (iron, silicon, etc.) for develop new compounds. As a result of that the scientists have learning to make devices using artificial structures in which the atoms are deposited layer by layer and after they are structured laterally following redesigned architectures and manipulate molecules individually. This allows making system with novel and different properties. With these technological advances it is possible to make artificial nanometer systems in where the effects of the quantum confinement in two space dimension can be observed (2D like quantum wells), in one (1D like wires and tubes), o in cero dimension (0D) like the case of a dot.

The transition to nanoscience begins when we ask how these nanoscale materials might be exploited to improve our lives. For example in the present medicine it is investigated how to incorporate the nanoparticle within the cells of the human body so that they work like sensors of the size of a molecule for detecting some problem like for example a tumor or cancer. On the other hand the investigation on nanoparticles also has contributed in another field like electronic devices. The devices today continue to diminish in size in order to achieve higher speeds. Several alternative concepts are being investigated that would reduce the device size, power consumption, and make use of multifunction properties of material. One of the hot topics today is to use, the spin of electrons, holes, nuclei, or ions to expand new functionalities in both analog and digital electronics. The mass, charge, and spin of the electron form the foundation of present information technology we use today. Integrated circuit and high-frequency devices have been constructed on the basis of semiconducting material where only the charge of the electron has had great advantage. On the other hand the devices for mass storage of information are carried out by magnetic recording (hard disks, magnetic tapes, optical disk, etc.) using spin of an electron in a ferromagnetic metal [1, 2].

Although so far is used separately in most cases, the combination of two degrees of freedom can result in enhanced performance of the existing devices. It may also make it possible to realize functionalities not available by using only one of the two. We may then be able to use the capability of mass storage and processing of information at the same time. On the other hand, we may be able to inject spin-polarized current into semiconductors to control the spin state of carriers, which may allow us to carry out qubit (quantum bit) operation required for quantum computing. This branch of electronics that tries to combine these two degrees of freedom in a single device is known now as "spintronics" [3].

The reason why this material has not yet been made is due to the semiconductor used so far for devices and integrated circuits, such as silicon (Si)

and gallium arsenide (GaAs), these does not contain magnetic ions and are nonmagnetic properties. Moreover in order to obtain a useful difference in the energy between the two possibilities of the orientation of spin (up and down), the magnetic field that would have to be applied are too high for everyday use [4]. However, the crystal structure, lattice parameters, and physical and chemical properties, of magnetic material are usually very different from that of the material semiconductor used in electronic, this make both material incompatible with each other.

Indeed, magnetism and semiconducting properties are know to coexist in some ferromagnetic semiconductors materials, such as europium chalcogenides [5, 6] and ferrimagnetic and ferromagnetic semiconducting spinel, that have a periodic array of magnetic element (Figure 1A) but these semiconductors are difficult to grow and are incompatible with the semiconductor material such as Si, and GaAs because its crystalline structure is absolutely different and have low curie temperatures (T_c s) about 100 K [7, 8].

In order to achieve a ferromagnetic semiconductor (Figure 1C) consist in introduce different atoms of impurity, such as Mn, Cr, Co, Ni, Fe and Cu into the structure of non-magnetic semiconductors (Figure 1B). This category of semiconductor is then called dilute magnetic semiconductor or (DMSs) [8].

The introduction of the magnetic ion in different semiconductor compound it provide the possibility of using and study a variety of magnetic and magnetic-optical phenomena not present in conventional non-magnetic semiconductor. Recently a big number of investigations have been focused in the elaboration of news DMSs material in different semiconductor host. Indeed, these investigations have been oriented to the find to develop ferromagnetism to room temperature to realize a new class of spintronics devices such as spin valves, transistors, spins Light emitting diodes, magnetic sensors, non-volatile memory, logic devices, optical isolators and ultra-fast optical switches. The potential

advantages of these spintronics devices will be higher speed, greater efficiency, and better stability, in addition to the low energy required to flip a spin.

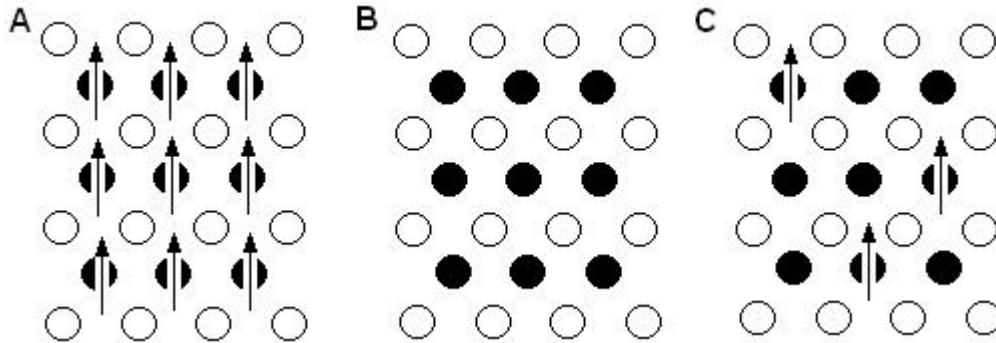


Figure 1. Three type of semiconductors: (A) a magnetic semiconductor, in which a periodic array of element is present; (B) a nonmagnetic semiconductor, which no contain magnetic ions; (B) a dilute magnetic semiconductor and magnetic element.

One of the system dilute magnetic semiconductors (DMS) investigated previously was base on III-V semiconductor, such as $\text{In}_{1-x}\text{Mn}_x\text{As}$ and $\text{Ga}_{1-x}\text{Mn}_x\text{As}$ discovered and studied by Munekata et al. [8] and Ohno et al. [9]. In these systems grow by MBE a small concentration of Mn atoms, or in general of transition metal atoms (TM), with typical concentration of 3 – 8 % are randomly distributed on the cationic sites. Nevertheless, a problem of these DMS systems is that the Curie temperature is well below room temperature, ranging between 35 and 172 K.

On the other hand, the magnetism in III-V and II-VI compound-based DMS has been investigated recently by H. Katayama and K. Sato [10], considering that the principal mechanism of the carrier induce ferromagnetism in DMSs has not been understood, a systematic study on the magnetic properties in GaN- based was elaborated on the base *ab initio* electronic structure calculation based on the LSDA (Local Spin Density Approximation) using the KKR-CPA (Korringa-Kohn-Rostoker combine with Coherent Potential Approximation) method, where

previous result predicted ferromagnetism in these compound-base in particular, the magnetism of 3d transition metal doped GaN where was investigated systematically. GaN is a material that has wide band gap energy and has been one of the most promising materials for information processing with short wavelength optic and view point of industrial application has great importance. Dietl *et al.* have calculated T_c using the Zener model and mean field model for various DMS, and obtained two important results [11]. (i) The T_c of (Ga,Mn)N is above room temperature; and (ii) T_c increases with the p-type carrier density. The first result has been realized in experiments, and the second result also has been verified by a large number of experimental. The Zener's model is the most successful one among these models.

In this model, the temperature dependence of the magnetic susceptibility above the transition temperature is assumed to be given by the Curie-Weiss law, and the *sp-d* interactions are regarded as the effective magnetic field acting on the carrier system. When spontaneous magnetization and hole are present, spin-splitting occurs in the valence band and the energy of the carrier system decrease as result at the same time, the spontaneous magnetization increase the free energy of the localized magnetic spins. This free energy penalty decreases with lowering temperature and at a certain temperature the energy gain and loss balances. This is T_c by the mean field model. This is known as Zener's ferromagnetism.

The 3d-TMs doped II-IV compound semiconductor with zinc-blend type, such as (Zn, Mn)Se, (Cd, Mn)Te or (Zn, Mn)Te have high potentiality as magneto-optical and semiconductor-spintronics materials, because the solubility of the 3d-TMs' in II-VI compound semiconductor is extremely higher than that in the III-V compound semiconductor such as (Ga, Mn)As or (In, Mn)As. The transition metals doped II-VI compound semiconductor can profit of the higher solubility of the TMs impurities (around 10 or 25% in thermal equilibrium) [12]. Several researchers have since then reported observation of room temperature

ferromagnetism in doped semiconductors. A considerable attention has been paid to semiconductors doped with ferromagnetic metals (Co, Fe, and Ni). In these types of systems, the fundamental issue of much concern is that the ferromagnetic ordering could be a result of metal precipitates e.g., Co in Co doped TiO_2 and Co doped ZnO [6, 13, 14, 15]. Moreover, a definite picture regarding the actual mechanism of ferromagnetic ordering in these systems has not been established.

The present thesis was focused on the determination of the structural, optics and magnetic properties, of the synthesis of bare and transition metal doped ZnO nanocrystals, synthesized. One of the main advances of this method is that permit the manipulation of matter at the molecular level. Due to its versatility in feasibility, this method it allow us control the size, shape, and size distribution of our nanoparticles, which cannot be done by some high-temperature vacuum deposition and solid-state synthesis techniques, which often use dopant source material that are themselves undesirable contaminants, which become necessary high temperature that may promote segregation of metallic precipitates. Solution processing routes are based on low cost, no toxicity, friendly and easily scalable methods. Until recently, there has been a great interest to synthesize and develop diluted magnetic semiconductor nanocrystal from the chemical methods, given that direct chemical approaches are generally compatible with large-scale production, and the resulting colloidal suspensions are ready for application in self-assembly strategies that have become a mainstay of nanotechnology. Despite uncertainty in the mechanism of ferromagnetism in doped semiconductors with different transition metal ion, and the fact that the obtained magnetization is lower than the theoretically predicted value in most of the reports appearing in literature, the results reported thus far, provide a pathway for exploring the different alternative synthesis preparation for achieve the prediction proposals. It is however, imperative to understand the phenomenon and the factors affecting the magnetization value in order to realize commercially applicable devices.

1.2 OBJECTIVES

The objective of the present research can be summarized as follows.

1) Determination of the size-controlled synthesis conditions for bare and transition metal ions doped- ZnO nanocrystals in ethanol media at room-temperature.

2) Determination of the corresponding functional properties as a function of composition and crystallite size at the nanoscale.

3) Verification of the theoretical expectations of room-temperature ferromagnetism in transition metal doped-ZnO nanocrystals.

1.3 SUMMARY OF THIS THESIS

A brief outline of the content of this thesis is as follows. Chapter 2 consists of a bibliographical revision of related works on ZnO-based nanostructures and the theoretical predictions of room temperature ferromagnetism. Chapter 3 details the experimental procedures to produce high quality ZnO nanocrystals as well as a brief description of the different techniques used to characterize our products. Chapter 4 is focused on the analysis and interpretation of the obtained results. Chapters 5 present the concluding remarks of our research. Finally, Chapter 6 lists the references consulted.

2. BACKGROUND

2.1 SPINTRONICS

How we talk about previously, two the most important successfully technologies today in the world has been the Si integrated circuit (ICs) and the data storage industry. Both continue to advance at a rapid pace. In the case of the integrated circuit obey to the Moore law that predicts that the number of the transistor of a chip double about every 18 months. On the other hands the data storage industry has had a great and significant advance in the elaboration of different devices for this end. For example for magnetic hard disk driver technology, a typical desk-top computer drive today has a 40 GB, whereas in 1995 this capacity was approximately 1GB [2].

All integrate circuit operate controlling the flow of the carrier of charge in this case (electron and hole) through the semiconductor when we applied an electric field. This is the dominant parameter in this type of devices. For the case of magnetic data storage, the dominant parameter is the spin of the electron where this characteristic intrinsic can be consider as the fundamental origin of the magnetic moment.

Into of the characteristic more important of ICs consist in your high speed signal processing and excellent trustworthy, but the memory element are volatile (the stored information is lost when the power is switched-off, as data is stored in capacitors, i.e. DRAMs). A big advantage of magnetic memories technologies is that these are non-volatile since they employ ferromagnetic materials which by nature have remanence.

A new field of the electronic opens the possibility for the study and understands of the properties a new material that tries combining these two

promise characteristic (charge and spin). This branch of the electronic is know like, semiconductor “*spin transfer electronics*” (spintronics). Spintronics, or spin electronics, consist in the study of actives control and manipulation of spin degrees of freedom in solid state system. On this base several group of investigator in the world is trying looking for material which combining both properties, to create an amazing new generation of electronic devices.

This characteristic open the possibility of developing spintronics devices that could be much smaller, (less than 100 nanometers) with consume less electricity and be more powerful for certain types of computations than is possible with electron-charge based system. The scientific community hope understand the behavior of electron spin in these kind of material, in order to provide something foundations new about solid state physics that will lead to a new generation of electronic devices based on the flow of spin in addition of the flow of charge.

2.2 SPINTRONICS DEVICES

There are a number of requirement for achieving practical spintronics devices. One these is the capability to transport the carriers with high transmission efficiency within the host semiconductor or conducting oxide, the capability to detect or collect the spin-polarized carriers and to be capable of controlling transport through external means such as biasing of a gate contact on a transistor structure. These type aspects of spin injection, spin-dependent transport, manipulation and detection form the basis of current research and future technology.

The spintronics devices has taken high interest after the discovery of the “*Giant Magnetoresistive or GMR*” in late 1980 by M. N. Baibich [17] and Grunberg’s group [18] in MBE-grown epitaxial Fe/Co multilayers at low temperature and high magnetic fields, as well as work by Parkin et al. [19] on

sputtered polycrystalline multilayers. The first significant GMR device was the spin valve [20] Figure 2. this consist in tri-layered sandwich structure, where a 'soft' ferromagnetic layer responds to a magnetic field, while a pinned ferromagnetic layer does not. A thin conductor layer (this layer is nonmagnetic normally cooper) is placed between the two ferromagnetic layers.

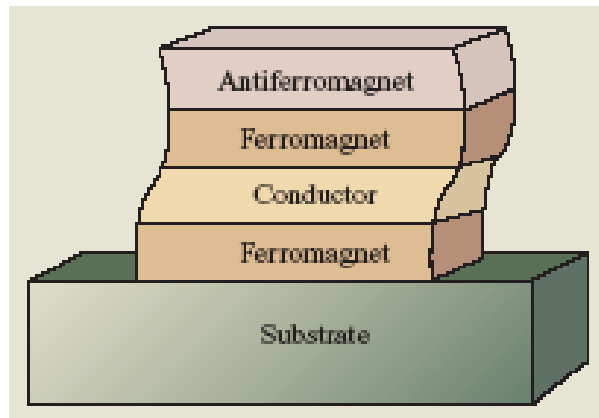


Figure 2. GMR structure [20]

When the magnetizations in the two ferromagnetic layers are parallel, conduction electron pass between them more freely than when the magnetizations are anti-parallel, and thus the resistance is lower in the parallel magnetization case than in the anti-parallel case. This change in resistance (also called magnetoresistance) is used to sense changes in magnetic fields. Almost ever these devices are accomplished through coupling to an antiferromagnetic layer (typically constructed from iron and manganese), as show in the picture. This structure can be configured as a magnetic field sensor, for example in automobile braking system, hysteretic memory device (non-volatile memory chips) or as a magnetic tunnel junction device where have attracted considerable interest in magnetic random access memories (MRAMS) as we see later.

One of the most important profits of this technology was applied by company IBM. In 1997 IBM scientist from the laboratory of Almaden Research Center of

IBM introduces to the market the first hard disk product using GMR heads. These have capacities of up to 75 GB and real densities of approximately 10 to 15 Gbits/in², in the 2000, the same laboratory has already produced GMR heads with a real density of 35 Gbits/in², which indicate more storage capacity around 200 GB [22]. The GMR heads are more superior and powerful to conventional MR heads for the reason that they are more super-sensitive, can detect weaker and smaller signals, which does to increase a *real density* (also called bit density) and thus capacity and performance.

2.2.1 Magnetic Tunnel Junction and MRAM

The magnetic tunnel junction (MTJ) is the second type of spintronics device that will have soon important application. A MJT is a structure that consists in two ferromagnetic layers (electrodes) that they are separate by a very thin insulating layer, commonly aluminum oxide. The electrons can tunnel through the insulating layer and additionally the probability, of tunneling from a ferromagnetic electrode depends of the spin direction, the resistance of the MTJ is different for the parallel and antiparallel orientation of the magnetic moments of the electrodes.

MTJ are very small size, below the micron range and can be fabricated by lithographic techniques. An important application of this small size MTJ will be for a new type of computer memory. As we show in the Figure 3, each junction can store one bit of data, "0" for the parallel configuration of the magnetic moments of the electrodes, and "1" for the antiparallel configuration. These MRAM is presently in development and it is expected to reach similar densities and access times as the current DRAM or SRAM, but the their main objective on these volatile semiconductor-base memories is that they can retain data after the power is turned off, possibly eliminating the long boot-up time when the computer is switched on.

The diversity of physical phenomena that control the operation of these magnetoresistive devices also makes MTJs very attractive from a fundamental physics perspective. Today the physics of spin dependent tunneling is still not clearly understood. This attention has stimulated remarkable activity in the experimental and theoretical investigations of the electronic, magnetic and transport of the MTJs.

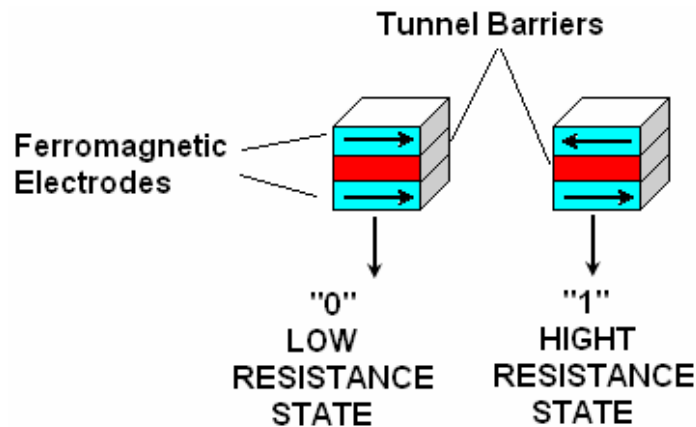


Figure 3. Schematic representation of a MRAM with MTJ.

2.2.2 Spin FET:

The common goal in many spintronics devices is to maximize the spin detection sensitivity to the point that it detects not the spin itself, but changes in the spin states. In 1990 Datta and Das [23] proposed a design for a spin-polarized field-effect transistor, or spin FET, maybe was the first idea of a spintronic device. Figures 4a and 4b, illustrate the scheme of the structure of the usual FET, with a drain, a source, a narrow channel, and a gate for controlling the current. The gate allows the current to flow (ON) or does not (OFF). In the Datta-Das SFET the source and the drain are ferromagnets acting as injector and detector of the electron spin, the drain injects electrons with spins parallel to

the transport direction. The electrons are transported ballistically through the channel. When they arrive at the drain, their spin is detected.

The electron can enter the drain (ON) if its spin points in the same direction as of the spin in the drain, if not it is scattered away (OFF). The role of the gate is generating an effective magnetic field in the direction of show in the picture. This effective magnetic field causes the electron spins to precess. By modifying the voltage, one can cause the precession to lead to either parallel or antiparallel electron spin at the drain, effectively controlling the current.

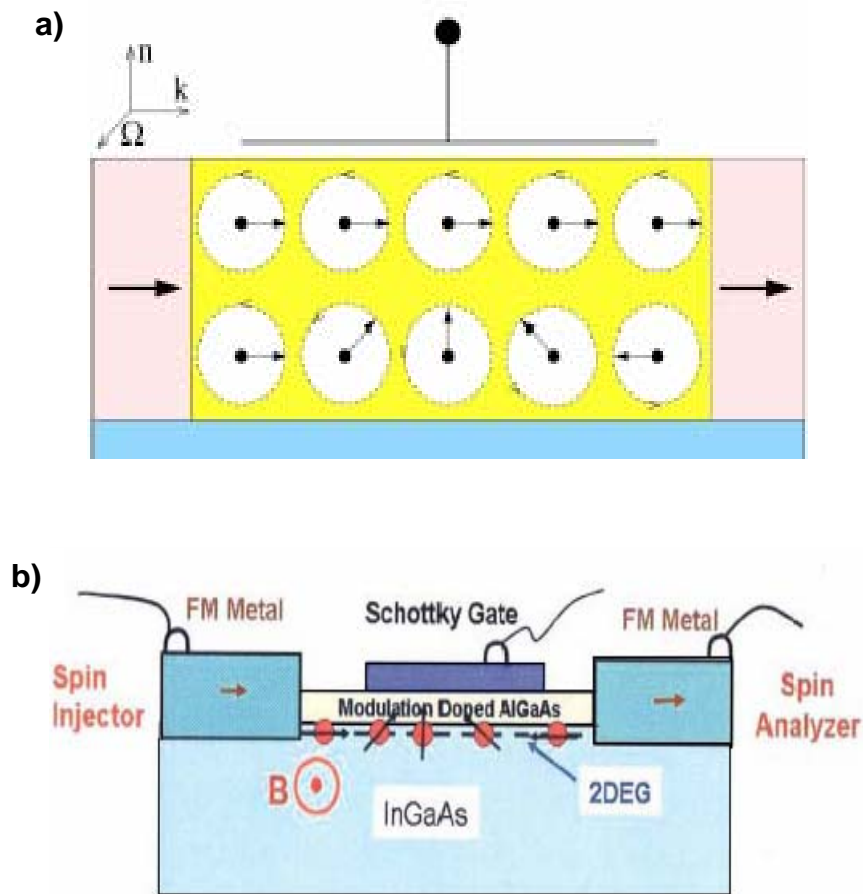


Figure 4. Scheme of the Datta-Das spin field-effect transistor (SFET) [23].

2.2.3 Spin LED

Efficient spin injection from the ferromagnetic metal and dilute magnetic semiconductor into semiconductor is the fundamental requirement of the semiconductor-based spintronics device.

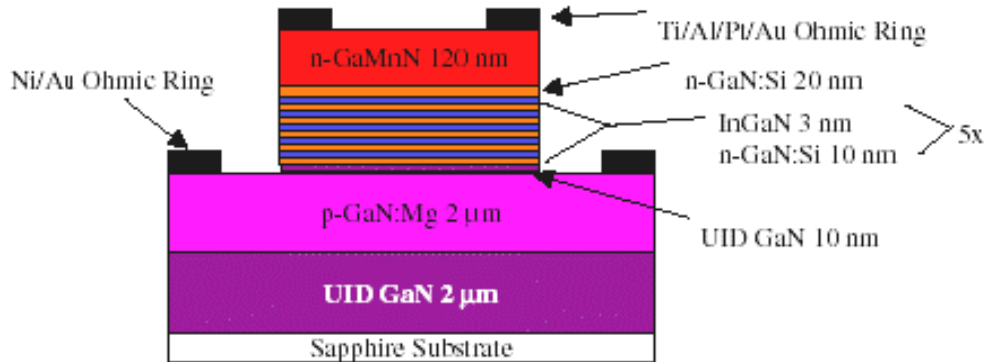


Figure 5. A schematic spin LED [24]

Spin-LED is used to measure the spin injection efficiency into materials. In a spin LED circularly polarized light is emitted after the recombination of spin-polarized carriers that are electrically injected into semiconductor structure. Such a device should allow us to modulate the polarization of the light emitted by the spin LED by application of an external magnetic field (Figure 5). The most straightforward approach to achieve this goal would be to implant Mn into the top contact p-GaN layer of the standard GaN/InGaN LED.

In conclusion today everyone already has a spintronics device on their desktop, as all modern computers use the spin valve in order to read and write data on their hard drive. It was followed immediately by the discovery of Tunneling Magnetoresistance (TMR) leading to the magnetic tunnel junction that has been utilized for the next generation computer memory known as Magnetic Random Access Memory (MRAM), another spintronics device for computers.

Therefore, the initial driving force for spintronics has been the improvement of computer technology.

2.3 DILUTED MAGNETIC SEMICONDUCTORS (DMS)

Diluted Magnetic Semiconductor (DMSs) makes reference to semimagnetic semiconductors, whose lattice is made up in part of substitution magnetic ions or appropriated rare earth. These semiconductor heterostructures have been intensively studied for many investigators in the world, due to the application in spintronics, which offers big opportunities for the next generation of microelectronic-nanoelectronic devices as well as spin dependent effect.

the most structure study today, have been focused to the $A_{1-x}^{II}TM_xB^{IV}$ alloy (where the TM = Sc^{2+} , Ti^{2+} , V^{2+} , Cr^{2+} , Mn^{2+} , Fe^{2+} , Co^{2+} , Ni^{2+} and Cu^{2+} or rare earth as Eu, Gd, Er) in which a fraction of the group II sub-lattice are replaced at random by this elements, given rise to localized magnetic moments in the semiconductor host.

These diluted magnetic semiconductors of the $A_{1-x}^{II}TM_xB^{IV}$ type are of interest for several distinct reasons [12]:

- a) *Their ternary nature gives us the possibility of “tuning” the lattice constant and band parameters by varying the composition of the material.*
- b) *The random distribution of magnetic ions over the cation sub-lattice leads to important magnetic effects, e.g., the formation of the spin-glass- like phase at low temperatures.*
- c) *The substitution transition metal ions like Mn atoms in the $A^{II}B^{IV}$ structure are also characterized by highly efficient electroluminescence, which make dilute*

magnetic semiconductor alloy important in the context of optical flat panel display application.

d) The spin dependent properties leads to dramatic effects physics, such as the giant Faraday rotation, the magnetic field induce metal-insulator transition, and the formation of bound magnetic polarons.

e) Due of the tenability of their lattice parameter and their energy gaps, the $A_{1-x}^{II}TM_xB^{IV}$ alloy are excellent candidate for the preparation of quantum wells, superlattices and another configuration that involve band-gap engineering.

One of the most important aspects in the DMSs structures this focused to the necessity of show evidence of ferromagnetism at room temperature in order to have practical application in spintronics devices. Several investigation has been oriented to study of II-IV compound, such as CdTe, ZnSe, CdSe, CdS, etc, doped with transition metal ion substituting their original cation [10,25], where the prediction suggested *high- T_c* for the V and Cr-doped ZnS, ZnSe, ZnTe. In this group of semiconductors materials the present of these magnetic ions influence the free carrier behavior through the *sp-d* exchange interaction between the localized magnetic moment and the spin of itinerant carriers [12].

On the other hand several search for achieve high T_c ferromagnetism at room temperature have been focused in a wide variety of oxides semiconductor as well as nitrides. Due to necessity that the DMS material must exhibit a critical T_c at room temperature Diet *et al.* [25] develop the theory based on mean-field theory which originates in the original Zener's model which predict that of hole-mediated ferromagnetism in tetrahedral coordinated semiconductor in special in p-type zinc blende and wurtzite structure which contain a sizable concentration of magnetic ions. In agreement with this theory the Figure 6 presents some potential candidates to achieve high T_c ferromagnetism at room temperature.

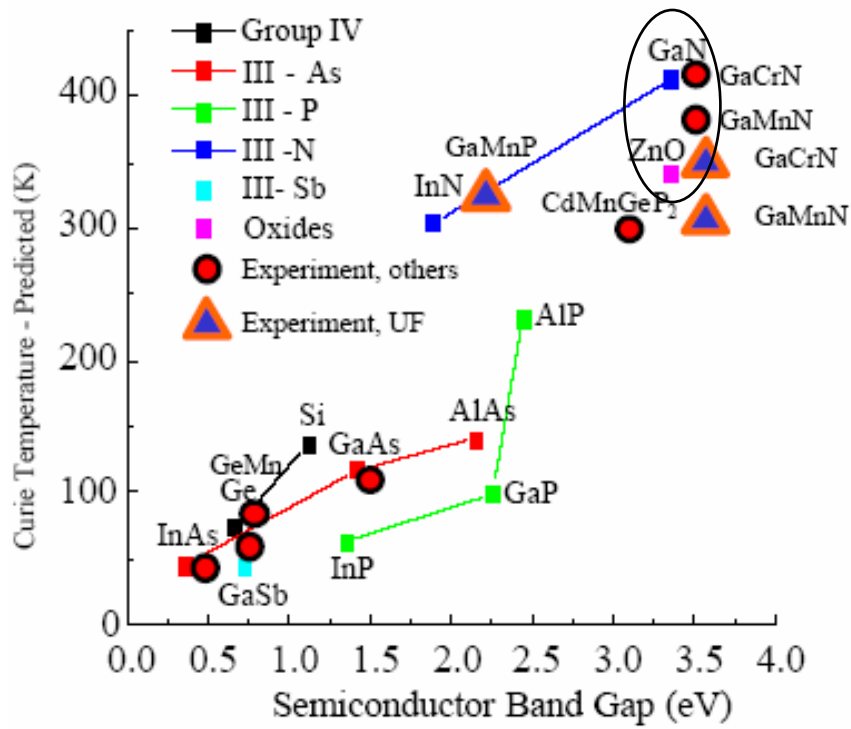
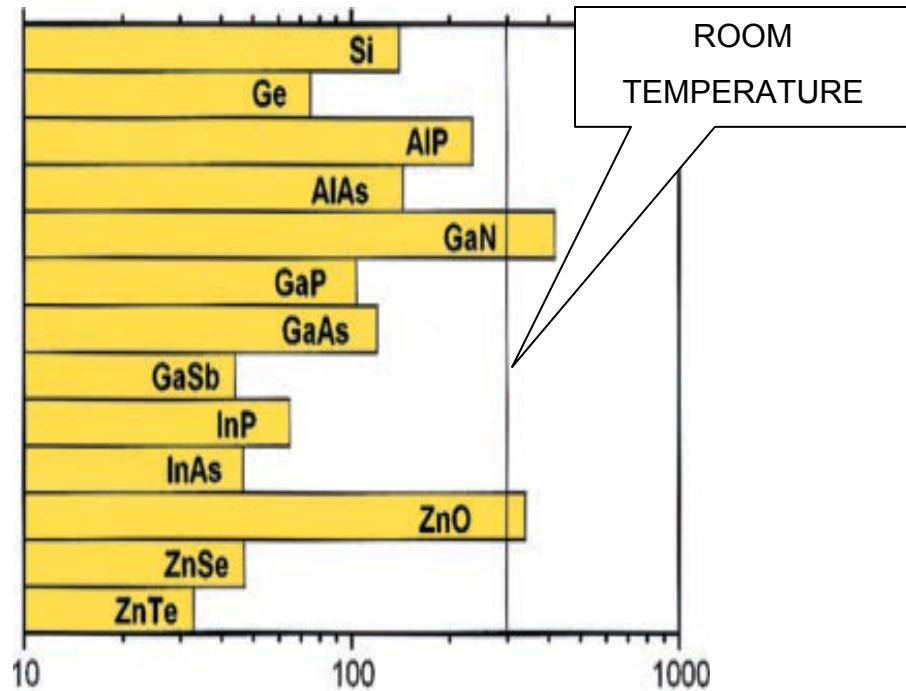


Figure 6. Estimated values of the Curie temperature T_c for various p-type semiconductors containing 5% of Mn and 3.5×10^{20} holes per cm^3 [16, 26]

The model take into account the anisotropy of the carrier-mediated exchange interaction related to the strong spin-orbit and $k.p$ coupling in the valence band and the influence of strain upon the hole density. This theory about ferromagnetic correlation mediated holes from shallow acceptors in the ensemble of the localized spins in doped magnetic semiconductor is suggest to the gallium nitride (GaN) and to zinc oxide (ZnO) which make possible candidates that could present ferromagnetism above room temperature upon doping with transition elements such as Mn (on the order of 5% or more) in p -type (on the order 10^{20} cm^{-3}) material [26].

Sato and Katayama-Yoshida [10,27-28] performed first *ab initio* calculation to simulate the random distribution of the dopant ion and predict the spin state interaction in different host semiconductor materials of the group II-IV and group III-V when are doped with transition metal ions such as V^{2+} , Cr^{2+} , Fe^{2+} , Co^{2+} and Ni^{2+} . These semiconducting materials demonstrate ferromagnetism without any additional carrier doping state when the concentration of this is increased from 5 to a 25%. As we can see the Figure 7. show the result obtained by using the KKR-CPA method to calculate the total energy difference between ferromagnetic state and the antiferromagnetic spin glass state.

For a positive energy difference indicates that the ferromagnetic state is more stable for V^{2+} -, Cr^{2+} - doped ZnO whereas Fe^{2+} -, Co^{2+} - and Ni^{2+} - doped ZnO show more stable ferromagnetism when increased TM in the semiconductor matrix whereas Mn shows spin-glass state. In these last systems the ferromagnetic state is much more stabilized by electron doping.

Considering that the n-type ZnO is easily available and the intrinsic defects such as the O-Vacancies and Zn- interstitial work as donor it is conclude that the (Zn,Fe)O, (Zn,Co)O and (Zn,Ni)O are promising candidates for achieve high-Tc ferromagnetism as well as suggested that the (Zn,Mn,Fe)O, (Zn, Mn,Co)O or (Zn,Mn,Ni)O may show carrier-induce ferromagnetism under electron doping

adjusting ratio of Mn to Fe, Co, Ni [28]. In the case for Mn^{2+} -, Fe^{2+} -, Co^{2+} -, or Ni^{2+} -doped ZnS (Figure 7b), ZnSe (Figure 7c) and ZnTe (Figure 7d) exhibits a spin glass state. The energy differences show a local minimum at Mn^{2+} (d^5) because the anti-ferromagnetic super-exchange interactions become dominant without the contribution of the ferromagnetic double-exchange interaction for insulator or semiconductor.

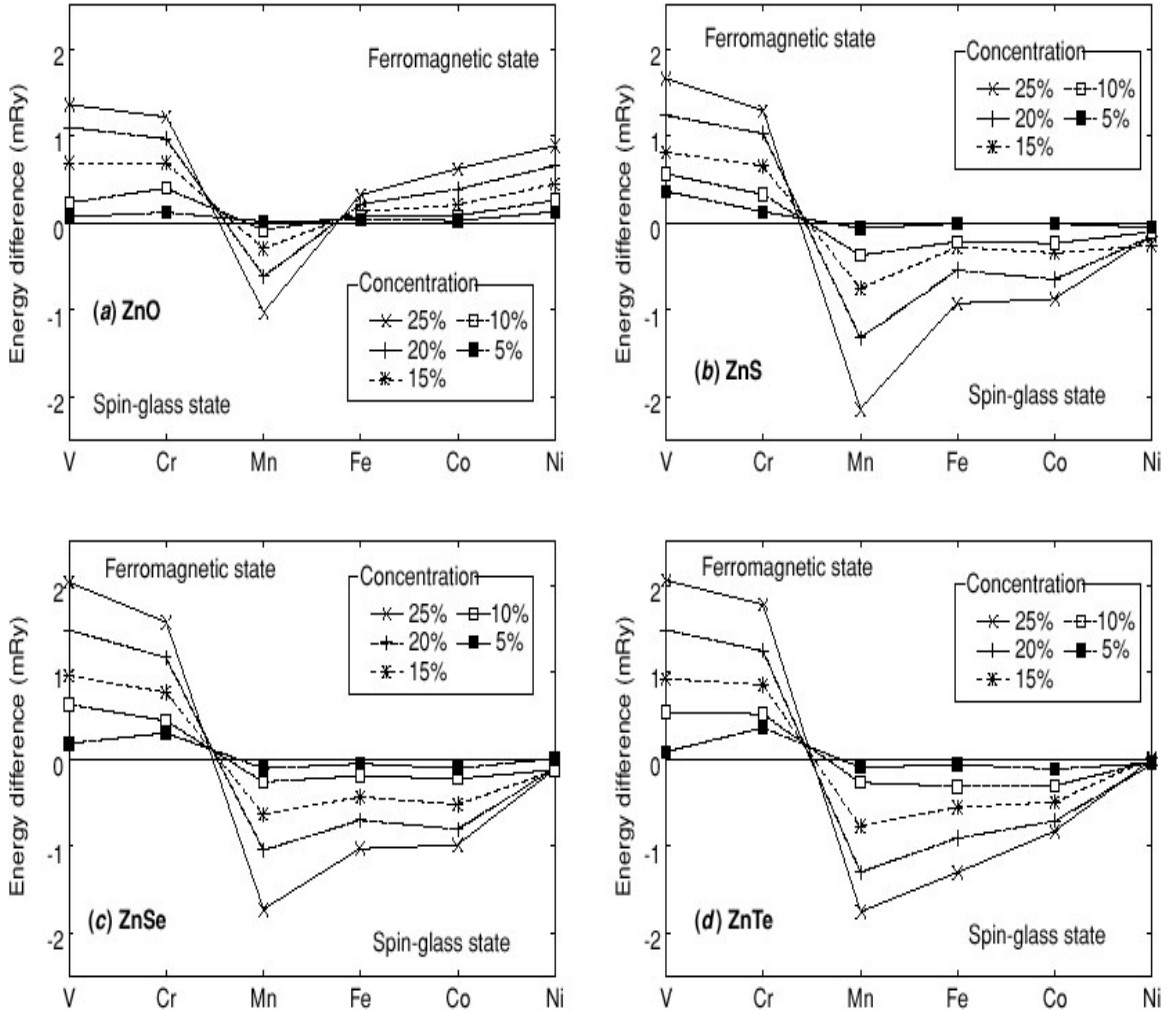


Figure 7. Stability of the ferromagnetic states in (a) ZnO-, (b) ZnS-, (c) ZnSe- and (d) ZnTe-based DMSs. V, Cr, Mn, Fe, Co or Ni is doped as a magnetic impurity. The vertical axis is the energy difference per formula unit between the ferromagnetic state and the spin-glass state. A positive energy difference indicates that the ferromagnetic state is more stable than the spin-glass state [28].

For the case of GaAs- and GaN- based DMSs is also investigate by [27]. Previous calculus predicts that these systems can be candidates to design DMSs. In the Figure 8, show the stability of the ferromagnetic state in GaAs and GaN based DMSs' and there are similar features between these two systems. First, spin-glass is more stable for Fe²⁺ is doped as a magnetic impurity. Also it is observe for Co²⁺- and Ni²⁺- doped ones, the energy difference is going to small, but the ferromagnetism is not still stable due to the presence of the spin glass state.

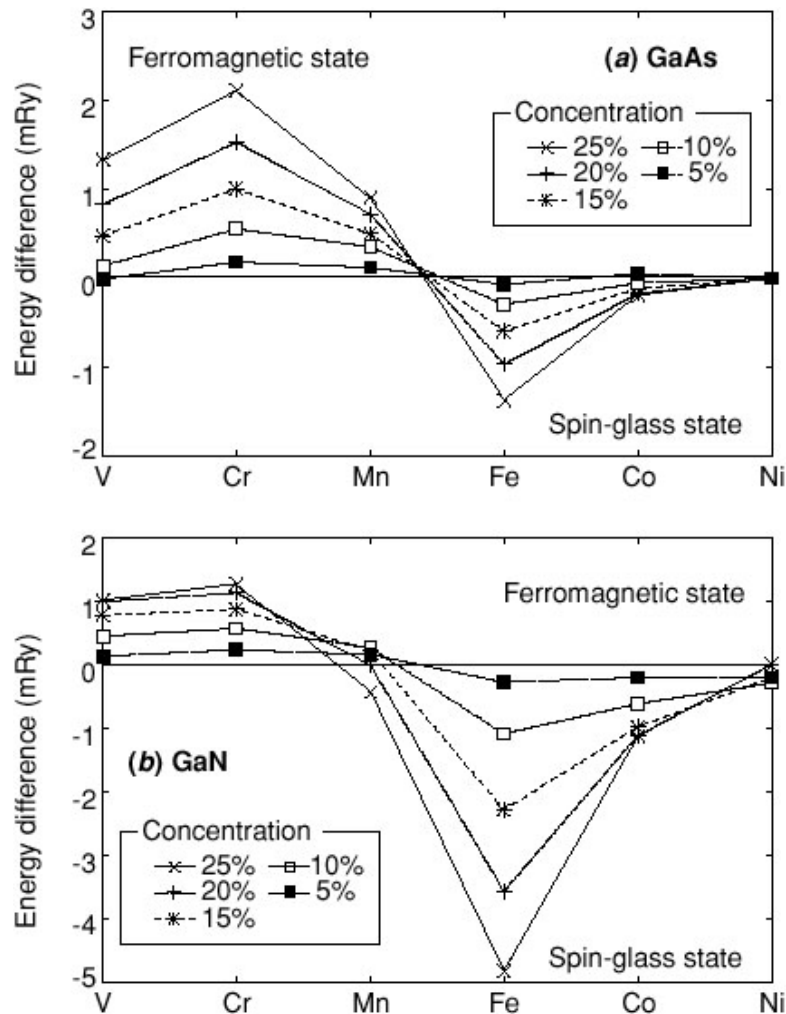


Figure 8. Stability of the ferromagnetic state in (a) GaAs- and (b) GaN-based DMSs [27].

Finally for V^{2+} -, Cr^{2+} -, Mn^{2+} - doped ones, the ferromagnetic state are more stable than the spin-glass state, except for Mn-doped GaN. In agreement with de Figure 8, the promising candidate for present high- T_c ferromagnetism is Cr-doped GaAs and GaN DMSs'. On the base of these theoretical prediction presented previously, there has been great interest in these class of material in special oxides semiconductor due to its application in transparent electronic, UV light emission, gas sensing, varistors and surface acoustic wave devices and for adding spin functionality to produce magnetic FETs.

2.4 OXIDE-BASED SEMICONDUCTORS

In contrast to non-oxide semiconductors, the oxide semiconductors have many advantages. Their wide band gap makes them transparent and also suitable for applications with short wavelength. They can be easily grown at low temperature even on a plastic substrate and are ecologically safe and durable besides being low in cost. In addition, the strong electronegativity of oxygen is expected to produce strong $p-d$ exchange coupling between band carriers and localized spins, and prerequisite for DMS. Summarized below are some of the report on oxide semiconductor based DMS.

2.4.1 ZnO- based DMS

Nanostructured ZnO materials have received broad attention due to their distinguished performance in electronic, optics and photonics. Synthesis of ZnO thin film has been received an active field because of their application as sensor, traducers and catalysts. ZnO is a semiconductor material of II-VI compound of the periodic table whose ionicity resides at the borderline between covalent and ionic semiconductor. The electronegative difference between zinc and oxygen produce a high degree of ionicity in its bond, which is considered in ones of the compound much ionics of this family.

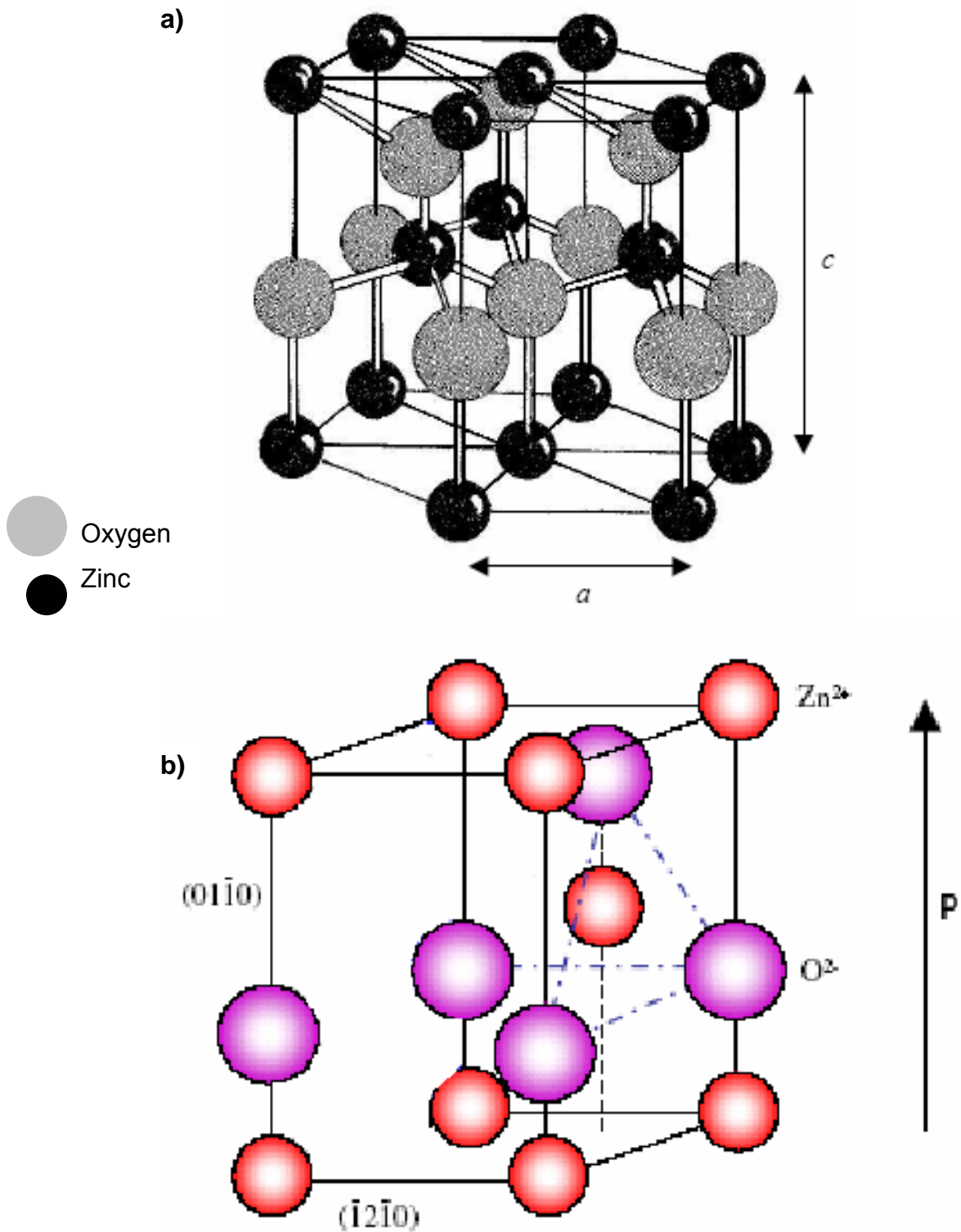


Figure 9. a) Schematic representation of a wurtzite ZnO structure having lattice constant a in the basal plane and c along the basal direction. b) Tetrahedral coordination. In each atoms of Zinc is surrounded by four cations of oxygen at the corners of a tetrahedron and vice versa.

This characteristic causes a considerable repulsion of its electronic clouds of charge, causing that their electronic structure more stable is wurtzite (Figure 9a). In this structure the atoms are completely remote to be able to compensate this repulsion. Thus, each atoms of Zinc is surrounded by four cations of oxygen at the corners of a tetrahedron and vice versa (see Figure 9b). This tetrahedral coordination is typical of sp^3 covalent bonding but don't forget that these materials also have a substantial ionic character as we did say before. This characteristic we can appreciate in the next picture. This crystalline structure is know as wurtzite structure and has a hexagonal unit cell with two lattice parameters, a and c in the ratio of $c/a = \sqrt{8/3} = 1.633$ and belongs to the space group of C_{6v}^4 or $P6_3mc$. This structure can be described as a combination alternate of hexagonal-close-packed (hcp) sublattices, each of which consist of one type of atom displaced each other along c -axis by the amount of $u = 3/8 = 0.375$ (in a ideal wurtzite structure) in fractional coordinates (the u parameter is defined as the length of the bond parallel to the c axis, in units of c).

Each one sublattice includes four atoms per unit cell and every atom of one kind (group-II atom) is surrounded by four atoms of the other kind (group VI), or vice versa, which are coordinated at edge of tetrahedron.

It should be pointed out that a strong correlation exists between the c/a ratio and the u parameter is that when the c/a decreases, the parameter u parameter increases in such a way that those four tetrahedral distances remain nearly constant through a distortion of tetrahedral angles due to long range polar interactions. These two slightly different bond lengths will be equal if the following relation holds [29]:

$$u = \left(\frac{1}{3}\right)\left(\frac{a^2}{c^2}\right) + \frac{1}{4}$$

Since the c/a ratio also correlates with the difference of the electronegativities of the two constituent, components with the greatest differences show the largest departure from c/a ratio [73]

i) Mn- doped ZnO

According to theoretical prediction from Sato's and Dietl's works, ZnO is a potential candidate for present ferromagnetism at RT when are doped with different transition metal. On the base of these prediction, in the ZnO, the equilibrium solubility limit of 3d transition metal such as Mn is larger than 10 mol %, and the electron effective mass is as large as $\sim 0.3m_e$ is free- electron mass [29-30]. Therefore the amount of injected spins and carriers can be large, which make Mn -doped ZnO ideal material for application in spintronics devices.

The confirmations to the theory by Dietl *et al* come with the report by Fukumura *et al* [30] where the incorporation of Mn into ZnO also was investigated by the technique of pulse laser deposition where the solubility of Mn into ZnO exceeded the equilibrium limit ($\sim 13\%$) and showed that Mn atoms could be doped into ZnO up to 35% without phase of segregation. As result of this increment of Mn the parameter of the lattice constant a and c of wurtzite $Zn_{1-x}Mn_xO$ augmented and the band gap expanded. However report of ferromagnetism alone is not sufficient, reason why which becomes necessary to take another measurement as FC and ZFC. Recently, Fukumura *et al* [31] measured the temperature dependence of magnetization in $Zn_{0.64}Mn_{0.36}O$ thin film grown by pulsed-laser deposition showing a spin-glass behavior with the large magnitude of the negative Curie-Weiss temperature correspond to a stronger antiferromagnetic exchange coupling. This behavior is consistent with the *ab initio* calculation by Sato and Katayama- Yoshida [10, 27-28] who predicted a transition from the antiferromagnetic state to the ferromagnetic state only with the introduction of holes.

Absence of ferromagnetic behavior was observed at 2 K by H- W. Zhang *et al* [32]. The magnetization was found to be contributed from both free spin and spins associated with antiferromagnetic cluster. The antiferromagnetic was confirmed by fitting a Curie-Weiss function. No ferromagnetic behavior has been observed at temperature 5 K in $Zn_{0.93}Mn_{0.07}O$ thin film deposited by RF magnetron sputtering [33]. The Auger spectroscopy showed that Mn is uniformly distributed throughout the film. The ferromagnetic property has been concluded as paramagnetic because the field dependent magnetization can be described well with Curie-Weiss law. Ueda *et al* [34] prepare by pulsed-laser deposition technique $Zn_{1-x}TM_xO$ ($x=0.05-0.25$: Mn) thin film, and any evidence of ferromagnetic behavior were not observed. Tiwari *et al* [46] did not find any ferromagnetism in their Mn- doped ZnO film grown on sapphire substrate using PLD.

On the other hand Jung *et al* [35]. reported on the discovery of ferromagnetism at low temperature in Mn- doped ZnO on epitaxial film prepared by laser molecular-beam epitaxy (LMBE) where the XRD pattern reveal an orientation preferential in the c-axis. Nevertheless the peak position shifted at lower angle when the concentration of manganese increased possibly due to substitution of Mn ions with a large ionic radius of 0.91 Å of for Zn (0.83 Å). The transition temperature obtained from magnetization measurement (M-T at 0.1T) was 30 K and 45 K, for a fraction of dopant of 0.1 and 0.3, respectively. In this research the coercive field (H_c) was 300 Oe at 5 K. Production of wurtzite-type tetrapods nanostructure [36] was prepared by evaporation of Zn metal under humid argon flow. After fabrication, Mn was doped into ZnO nanostructures by diffusion at 600 °C. The XRD pattern did not show any extra peak, which indicated the complete formation of structure. Magnetic measurement showed that the sample exhibited very large coercivity $H_c=5500$ Oe at 5.5 K. However, the FC and ZFC measurement at 100 Oe showed a Curie temperature of 43 K, which is consistent with Curie temperature of Mn_3O_4 . On the other hand, Secondary Ion Mass Spectrometer (SIMS) confirmed the existence of Zn^{+2} in the

surface and $(\text{Zn,Mn})\text{Mn}_2\text{O}_4$ which exhibited similar properties to Mn_3O_4 , and should be responsible to the magnetism of the Mn- doped ZnO nanostructure.

Heo *et al* [37] deposited Mn- doped ZnO by pulse laser deposition on sapphire substrate. They claimed that the saturation magnetization and coercivity of the implanted single-phase film were both a strong function of the initial annealing temperature ($600\text{ }^\circ\text{C}$), suggesting that carrier concentration alone could not account for the magnetic properties of ZnO:Mn.

The previous result were consistent with the work of Theodoropoulou *et al* [38] who found that FM in ZnO thin films deposited by reactive magnetron sputtering was strongly dependent of parameters such as growth temperature, O_2 partial pressure, and type of substrate (only films deposited on Al_2O_3 substrate were FM). Yan *et al* [39] fabricated thin film of $\text{Zn}_{1-x}\text{Co}_x\text{Al}_{0.01}\text{O}$ with a dopant concentration 'x' of 0.15 and 0.3 and $\text{Zn}_{0.7}(\text{Mn}_{0.15}\text{Co}_{0.15})\text{O}$ on Al_2O_3 substrate by pulsed laser deposition. All three doped ZnO films showed ferromagnetism a RT (290 K). The same group also reported that the successful doping of Co and (Mn, Co) co-doping in ZnO without forming second phases could only be realized at a low deposition temperature ($400\text{ }^\circ\text{C}$) and low oxygen pressure ($5 \times 10^{-5}\text{ Pa}$) and suggested under high deposition temperatures and oxygen pressures, cobalt will not substitute Zn in the lattice.

Only few synthesis processes of colloidal nanoparticles have been reported in the literature. Colloidal nanocrystals should form ideal hosts for strongly-confined artificial atoms, i.e. configuration of one to a few electrons occupying the conduction energy levels in the nanocrystal. Such nanocrystals can be obtained in molar quantities by wet chemical synthesis with increasing control of the size, shape and surface electronic properties.

Gamelin *et al* [40] reported the synthesis of colloidal Mn^{+2} - doped ZnO ($\text{Mn}^{+2}:\text{ZnO}$) quantum dots at room-temperature and the preparation of

ferromagnetic nanocrystalline thin films by hydrolysis and condensation reaction in DMSO under atmospheric conditions. Gamelin's group proposed that direct chemical syntheses of ZnO DMSs can provide better control over material composition than is obtained with some high-temperature vacuum deposition or solid-state synthesis techniques. The same group reported robust, high- T_c in thin films of these nanocrystals prepared by spin coating at 300 K. The corresponding coercivity was 92 Oe, approximately.

ii) Co- Doped ZnO

Several reports of ferromagnetism in Co-doped ZnO produced by different techniques have been reported. Magnetic properties of epitaxially grown in $Zn_{1-x}Co_xO$ thin film synthesized by pulsed laser deposition were investigated by Kim *et al.* [41]. The substrate was sapphire and the films were deposited under different growth temperature and oxygen gas pressure. The substrate temperature (T_s) varied from 300 to 700 °C and the O_2 pressure (P_{O_2}) from 10^{-6} to 10^{-1} Torr. When T_s was relatively low (<600 °C), homogeneous films with wurtzite structure were grown and evidenced predominant paramagnetism in contrast with ferromagnetic behavior in inhomogeneous film. This evident ferromagnetism was attributed to Co clusters. Lee *et al* [42], claimed high-temperature ferromagnetism in Co-doped ZnO thin films fabricated by sol-gel method grown on sapphire. Secondary phase was detected when the fraction of dopant was 0.25 which could correspondent to Co_2O_3 or Co_3O_4 . Although below of this concentration any extra pick was not detected by XRD, the author did not exclude the possibility of the formation of clusters which could have contributed to the observed ferromagnetic behavior.

Ueda *et al* [34] used the pulsed laser deposition technique to produce thin films of Co-doped ZnO deposited onto sapphire. The films showed the maximum solubility limit of 50% above which separation phase of ZnO and CoO was observed clearly. Some of the synthesized films exhibited ferromagnetic behavior

with a Curie temperature higher than room temperature (280 K, for $x=0.05$ and 300 K for $x=0.15$); however the mechanism of ferromagnetism was not clear enough. The reproducibility of the method was poor (less than 10%).

Magnetic and structural properties of cobalt implanted ZnO single crystal were investigated by Norton *et al* [43]. Single-crystal Sn-doped ZnO substrates were implanted at ~ 350 °C with Co to yield a dopant concentration of 3-5 at. %. The magnetization versus magnetic field for a 5 at % of Cobalt-doped sample was taken at 5 K and showed a clear hysteresis loop with coercive fields of less than 300 Oe. However, the Co-implanted material showed clear evidence of isolated Co precipitates that were identified by XRD analyses.

Ando *et al.* [44] observed strong magneto-optical effect of $Zn_{1-x}Co_xO$ near the optical band gap. Magnetic circular dichorism (MCD) and Faraday rotation for ($x=0.012$ and 0.016) at 5 K were two orders higher than for bare ZnO. These magneto-optical effects disappeared at room temperature. On the other hand Jin *et al* [45] fabricated epitaxial thin film by combinatorial laser molecular-beam epitaxy (MBE) method. Films were doped with all transition metal ions and found that both the ionic radius and valence state are thought to be important factor in determining the solubility behavior of the dopant. In agreement with this Mn^{+2} and Co^{+2} are favorable to have a high solubility limit among all the $3d$ ion species. The MCD measurements suggested a strong coupling interaction of the sp bands of ZnO with $3d$ electron of Mn^{+2} and Co^{+2} .

The advances in vacuum deposition methods have allowed preparation of many new nanoscale DMSs the have unique magnetic, magneto-optical, and magneto-electronic properties. Gamelin *et al* [47, 48] reported the influence of Co^{+2} and Ni^{+2} ions on the homogeneous nucleation of ZnO nanoparticles by direct chemical synthesis route. Using *ligand-field electronic absorption spectroscopy* as a dopant-specific optical probe to monitor incorporation during nanocrystal growth and to verify internal substitutional doping in Co^{+2} -, Ni^{+2} -

doped ZnO DMS QDs. The spectroscopic measurements revealed that Co^{+2} and Ni^{+2} ions were quantitative excluded from the ZnO critical nuclei but incorporated nearly isotropically statistically in the subsequent growth layers. These behaviors suggested that many dopants are expected to reside on the nanocrystal surfaces due to their high surface-to-volume ratios and also resulting in crystallites with pure ZnO cores and $\text{Zn}_{1-x}\text{Co}_x\text{O}$ shells.

iii) Other TM- doped ZnO systems

Saeki *et al.* [74] report curie temperature higher than 350 K for V- doped ZnO films (n-type for a concentration of $x= 0.05-0.15$) grown by PLD. They found out that only those samples with carrier concentration as high as 10^{18} cm^{-3} showed ferromagnetism, while the insulating ones were not ferromagnetic. Hong *et al* reported on magnetic properties of V- doped ZnO thin films grown below 650°C (V concentration 8.3 to 11.1%). These films showed ferromagnetic behavior at room temperature and spin-glass a low temperature, as observed from FC and ZFC magnetization. An increase of the substrate temperature above 650°C seems to favor a secondary phase, which resulted antiferromagnetic.

Magnetic properties of Ni-doped ZnO thin films were also studied by Wakano *et al* [75]. Ni was found to get dissolved in ZnO up to 25% without precipitation. For films doped with 3-25% Ni, ferromagnetism was observed at 2K. Above 30K, superparamagnetic behavior was observed. Schwartz *et al* [76] observed robust ferromagnetism with T_c above 350 K in Ni- doped ZnO nanocrystalline thin films prepared using high-quality colloidal DMS quantum dots as solution precursor. In addition of ferromagnetism, substantial superparamagnetism was also evident from the ZFC and FC magnetization data. There were also efforts to produce ZnO DMS by doping double TM element such as (Fe, Co) or (Fe, Cu). Cho *et al* [77] observed room temperature ferromagnetism for $\text{Zn}_{1-x}(\text{Fe}_{0.5}\text{Co}_{0.5})_x\text{O}$ films fabricated using reactive magnetron co-sputtering. The samples seem to have the single phase of the same wurtzite

structure as pure ZnO up to $x=0.15$. A rapid thermal annealing under vacuum led to increases in T_c , magnetization and carriers concentration. Han *et al* [78] also observe ferromagnetism in $Zn_{1-x}(Fe_{1-y}Cu_y)_xO$ bulk samples with $T_c \sim 550$ K. the saturation magnetic moment was determined to be $0.75 \mu_B$ per Fe, and increased as the Cu- doping ratio increased up to 1%. In addition, a large magnetoresistance was observed below 100 K. The origin of ferromagnetism in $Zn_{0.95-x}Fe_{0.05}Cu_xO$ bulk samples was investigated using zero field Fe nuclear magnetic resonance and neutron diffraction [79]. This measurement revealed that at low concentration Cu doping into $Zn_{0.95-x}Fe_{0.05}Cu_xO$ caused the formation of $ZnFe_2O_4$ nanoclusters with inverted spinel structure exhibiting a ferrimagnetic behavior at room temperature.

2.4.2 TiO₂ – based DMSs'

Since of discovery of room temperature ferromagnetism in Co-doped anatase TiO₂ thin films [80], several efforts to study the nature of the magnetism in this material have been performed [81-82]. Noh *et al* [83] reported that Co cluster can be easily formed in the epitaxial anatase TiO₂ thin films grown by laser molecular beam epitaxy and that these clusters seemed to contribute the major portion of the FM observed. Kim *et al* [84] performed X-ray magnetic circular dichroism measurements on the films and showed that the FM signals coincided with that of Co metal. However, Chamber *et al* [82] argued that there was a profound difference between the films grown by different methods. Superparamagnetism observed in Co-implanted epitaxial anatase TiO₂ films, suggested the presence of ferromagnetic precipitates, which might be Co clusters. The blocking temperature (T_B) was around 25 K after implantation. Annealing of the samples under a proper oxygen pressure resulted in the increment in T_B , which implied an increase in the size of the precipitates. Magnetization versus magnetic field (M-H) measurements were carried out at 5 and 300 K using the magnetometer SQUID. At low temperatures, the film presented ferromagnetic behavior. Above 300 K the hysteresis disappeared. This behavior can be explained by

superparamagnetism of the film with nano-sized precipitates. Similar behavior was found by S. R. Shinde *et al* [86], in $Ti_{1-x}Co_xO_{2-\delta}$ films with $x=0, 0.01, 0.02$ and 0.04 grown by pulsed laser deposition on to $R-Al_2O_3$ substrate. Magnetization versus magnetic field measurements was carried out at 5 and 300 K for a Co fraction 0.02. Although hysteresis was observed at room temperature, the coercivity (H_c) and remanence (M_R) were very small. On the other hand, the film exhibits a large H_c (>230 Oe) and M_R ($\sim 33\%$) at 5 K. Zero field cooled field cooled data diverged substantially at low temperatures and the hump in ZFC curve progressively shifted towards lower temperatures with increasing magnetic field. These behaviors were not expected for a ferromagnet and suggested the presence of magnetic nanoparticles in the films or the spin-glass nature of the system. The superparamagnetism was attributed to direct observation of clustering and cluster size in the film carried out by TEM. From the electron diffraction pattern, these clusters were identified as cobalt metal.

CHAPTER 3. EXPERIMENTAL

3.1. MATERIALS

All reagents were of analytical grade and were used without further purification. Required weights of acetate salts of Zn as well as Mn, Co, Ni, Cu and Fe were dissolved in anhydrous ethanol at 65°C to produce a solution with a total concentration of metal ions of 0.01M. A solution of LiOH in ethanol was used as the precipitating agent. N-heptane was used to coagulate nanocrystals from their suspensions in ethanol.

3.2. SYNTHESIS OF BARE ZnO AND TM²⁺ DOPED ZnO NANOCRYSTALS

ZnO quantum dots were synthesized from starting solutions of acetates salts in ethanol under alkaline conditions according with the following reaction:



Where OAc= acetate ion

Doped ZnO nanocrystals were formed by precipitation in ethanol solution as reported by Spanhel and Anderson for bare ZnO [49]. In our case, the synthesis was carried out under ambient-temperature conditions. When the synthesis of doped-ZnO was attempted, the metal ions solutions were prepared for a specific fraction of dopant coexisting with Zn ions in starting solutions, 'x'. The metals and the hydroxide solutions in ethanol were mixed at room temperature under vigorous stirring for 10 minutes (contact stage). In order to follow the progress of the oxide formation, the suspension of nanocrystals were aged in their mother liquors at room temperature and without stirring (aging stage). Nanocrystals

prepared in this way were recovered by successive coagulation/redispersion cycles using n-heptane/fresh ethanol and submitted for characterization. The present synthesis procedure is simple and permits a very fast nucleation with minimum aggregation of the nanocrystals at a temperature as low as 25 °C. Ethanol was selected not only as a suitable solvent but, specifically, because of its dehydrating property. This de-hydrating capability plays an essential role in the removal of coordinated water from the precursor compound (basic zinc acetate) that promoted the formation of anhydrous oxide structure at room temperature.

3.3 CHARACTERIZATION TECHNIQUES

Structural analysis of ZnO nanoparticles was performed in a Siemens D5000 X-Ray diffractometer (XRD) using CuK α radiation (0.15405 nm). ZnO nanocrystal sizes were estimated from XRD measurements and determined by high resolution transmission electron microscopy (HRTEM) images collected in the department of Material Science and Engineering of the University of Wisconsin-Madison. It was used a PHILIPS CM200 UT transmission electron microscopy (200 kV) with a high brightness LaB₆ filament as an electron source. Copper grids coated with carbon amorphous were used to place the samples for HRTEM observations. The optical properties of nanocrystals were determined from UV-Vis spectra recorded with a Beckman Coulter DU800 spectrophotometer. Spectra from colloidal suspension were obtained with 1-cm quartz cell. Optical absorption spectra were attained for monitoring the band gap enlargement due to the quantum size effect, promoted for smaller nanocrystals sizes. FT-IR spectra were recorded with Digilab FTS 1000 Scimitar Series in ATR mode. Magnetic characterization was carried out using a Superconducting Quantum Interferometer Device (SQUID) Quantum Design MPMS XL-7 magnetometer in RSO mode.

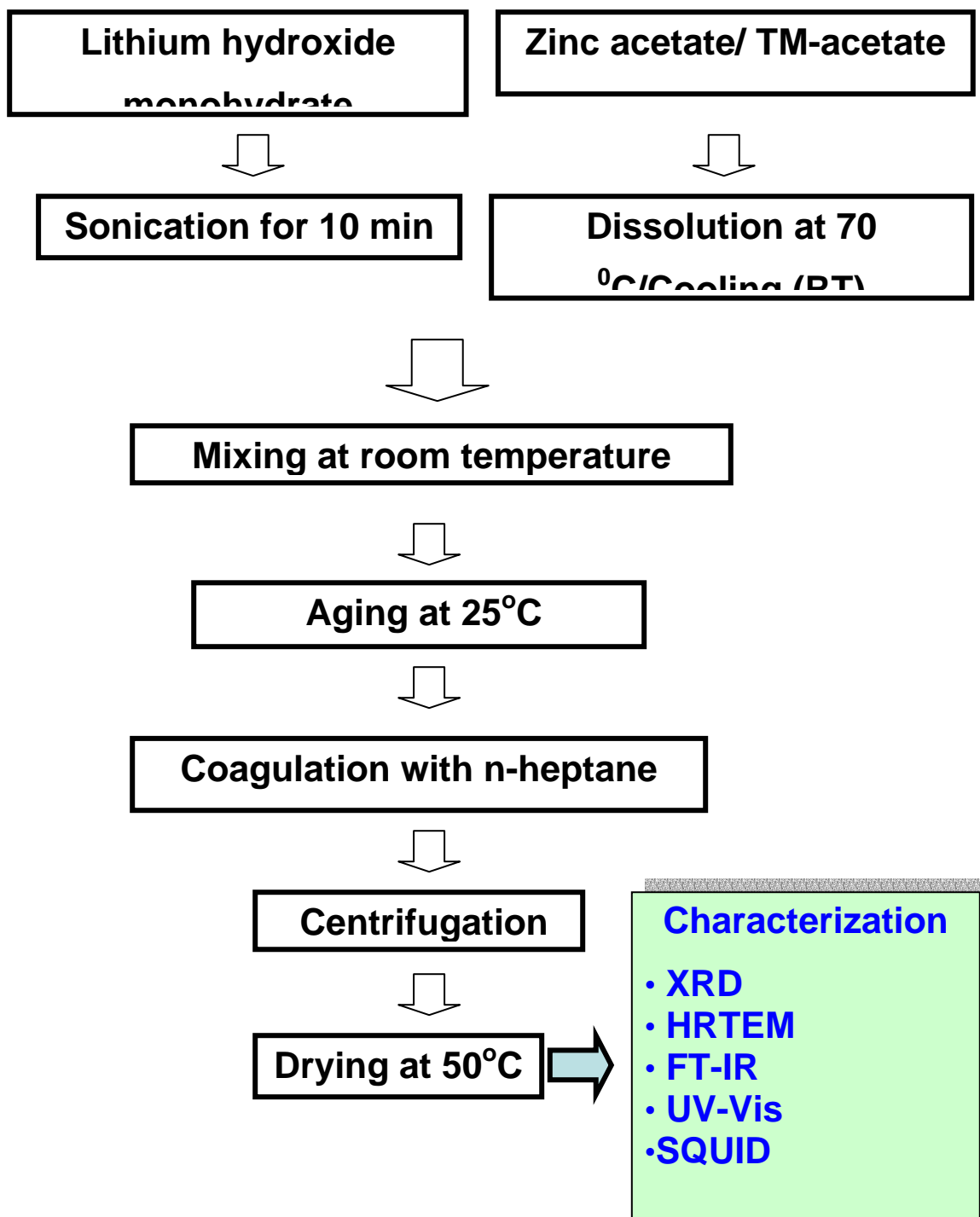


Figure 10. Flow chart of synthesis procedure of ZnO nanocrystals.

CHAPTER 4. RESULTS AND DISCUSSION

4.1 XRD CHARACTERIZATION

The fact that X-ray have a wavelength of the order of angstroms, which is suitable for inter-atomic distances in solids, makes this technique an excellent instrument to investigate the crystalline structure of the materials. In our case, the X-Ray diffraction patterns were obtained using a Siemens D-5000 X-ray diffractometer with $\text{CuK}\alpha$ ($\lambda=1.5406 \text{ \AA}$) radiation. All measurements were carried out at 35 kV and 30 mA in the range of $15^\circ \leq 2\theta \leq 75^\circ$. The scanning step and sampling time were 0.02° and one second, respectively.

4.1.1 Bare ZnO nanocrystals

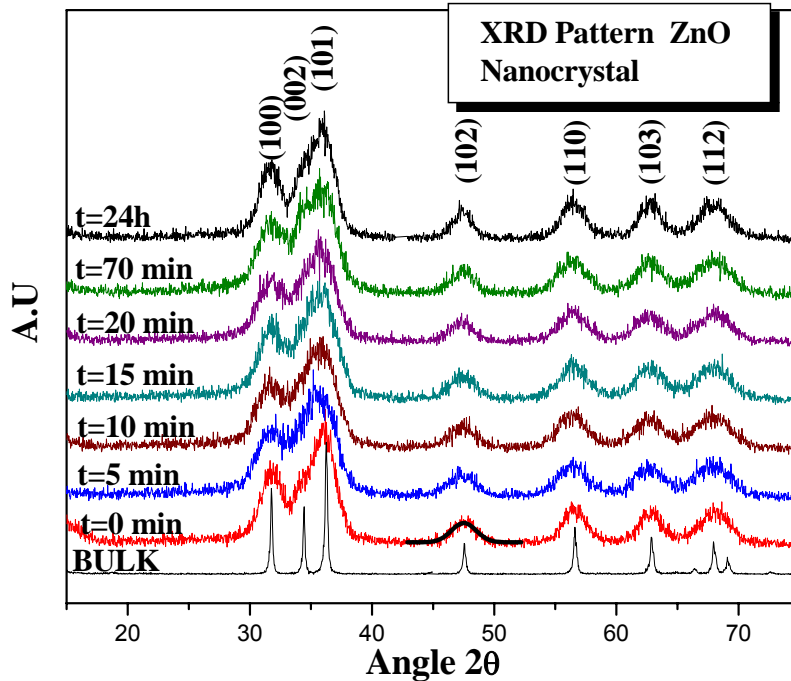


Figure 11. XRD patterns for bare ZnO synthesized at different aging times. All peaks correspond to ZnO wurtzite structure. ZnO was rapidly formed even right after 10 minutes of mixing without aging. The broadness of the XRD peaks reveals the nanocrystalline nature of the ZnO powders. The average crystallite size was estimated to be $\sim 6 \text{ nm}$ using Scherrer's equation.

Figure 11 shows the XRD patterns for ZnO powders produced at different aging times at 25°C. As seen, all XRD patterns correspond to a wurtzite structure. The ZnO structure was fully developed after a contact time as short as 10 minutes at room temperature even with no need for further aging. In turn, this broadening explain the overlapping of the (002) and (101) peaks in nanocrystalline ZnO. The average crystallite size $\langle d \rangle$ was estimated by using the by Debye-Scherrer's equation:

$$\langle d \rangle = \frac{0.95\lambda}{B \cos \theta} \quad (1)$$

In this equation, λ represent the wavelength of the X-ray radiation, B the full width at half maximum of the diffraction pick (in radians) and θ the maximum scatter angle. We use the (102) peak in the XRD patterns to calculate the average crystallite size. Obtained results are given in the following table as a function of aging time at room temperature.

Table 1. Average crystallite size of bare ZnO nanocrystals synthesized at different aging times.

<i>Aging time</i>	<i>Average crystallite size</i> <i>(nm)</i>
0 minutes	3.59
5 minutes	3.87
10 minutes	4.1
15 minutes	4.14
20 minutes	4.46
70 minutes	4.76
24 hours	5.39

Evidently, a further crystal growth (incorporation of zinc and oxygen ions into ZnO nuclei) took place during aging. The lattice parameter for hexagonal ZnO nanocrystals were estimated from the (102) plane using the equation:

$$\frac{1}{d_{hkl}^2} = \frac{4}{3} \left(\frac{h^2 + hk + k^2}{a^2} \right) + \frac{l^2}{c^2} \quad (2)$$

Being a and c the lattice parameters and h , k , and l the Miller indices and d_{hkl} the interplanar spacing for the plane (hkl) . This interplanar spacing can be calculated from:

$$2d \sin \theta = n\lambda \quad (3)$$

Where λ the wavelength of X-ray is, θ is diffraction angle, and n is the order diffraction ($n=1$). The corresponding lattice parameters were $a = 3.250 \text{ \AA}$ and $c = 5.265 \text{ \AA}$ for an aging time ($t=0$ minutes) which are very close to the theoretical result of the wurtzite phase of bulk ZnO ($a=3.24982 \text{ \AA}$, $c=5.20661 \text{ \AA}$).

4.1.2 TM- doped ZnO nanocrystals, (TM = Mn, Co, Ni, Cu, Fe)

Our previous results verified the rapid and direct synthesis (i.e., annealing was not needed for the development of the oxide phase) of high-purity ZnO structure. In the present section, we present the results on the synthesis of ZnO nanocrystals in presence of divalent dopant species. All synthesis conditions were the same as for the bare ZnO, with exception of the composition of the reacting solution that contained suitable amounts of dopant species. The effects of the atomic fraction of dopants in starting solution, 'x', and the length of the aging period under room temperature condition, were evaluated.

Mn-doped ZnO nanocrystals

Figure 12 and 13 show the XRD patterns corresponding to Mn-doped ZnO powders synthesized at different atomic fraction of Mn ions, 'x', after 30 minutes and 24 hours of aging, respectively. It must be remarked that, in contrast with the formation of bare ZnO nanocrystals, the complete development of the oxide structure demanded a long enough aging of the solids at room temperature; moreover, the higher 'x' the longer the aging time required to develop the host ZnO structure. As Figure 12 evidences, base ZnO structure can be fully developed only after 30 minutes of aging for 'x' values of 0.01 and 0.05. The absence of any extra XRD peak suggests the actual incorporation of dopant species into the ZnO structure.

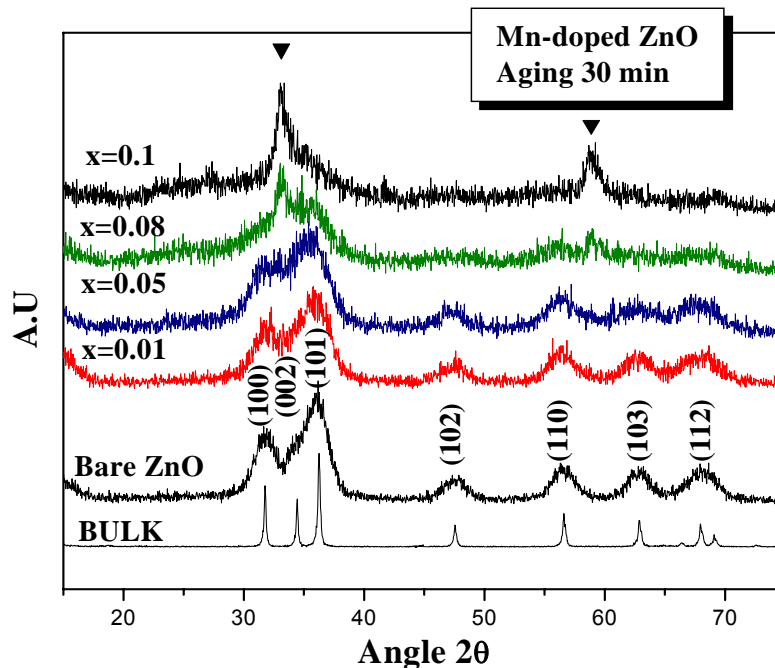


Figure 12. XRD of Mn-doped ZnO nanocrystals synthesized at different 'x' values (where 'x' is the nominal Mn fraction in starting solutions) and 30 minutes of aging at room temperature. The XRD spectra evidenced that an increase in the 'x' value delayed the formation of the ZnO host structure. The solid produced for x = 0.08 consisted of incipient ZnO coexisting with the precursor compound, for which XRD peaks are identified with a mark. The precursor compound can be considered to be $\text{Zn}(\text{OH})_2$ or a basic Zn acetate.

Once again, the peaks broadening reveal the nanocrystalline nature of the precipitates. The formation of the base ZnO did not take place for 'x' values above 0.08 at the end of the 30 minutes aging. In this case, a peak centered at 2θ 59.5° was clearly observed, which was attributed to a precursor compound. This precursor phase can be a bearing basic zinc acetate $Zn_4O(Ac)_6$ or Zinc hydroxide $Zn(OH)_2$ [50-51]. Accordingly, we propose that the actual incorporation of dopant species retarded the development of the host ZnO structure by promoting the stability of the intermediate compound and inhibiting the corresponding dehydration and atomic rearrangement involved with the formation of the oxide phase. A more detailed monitoring of the aging period allowed us to verify experimentally this statement.

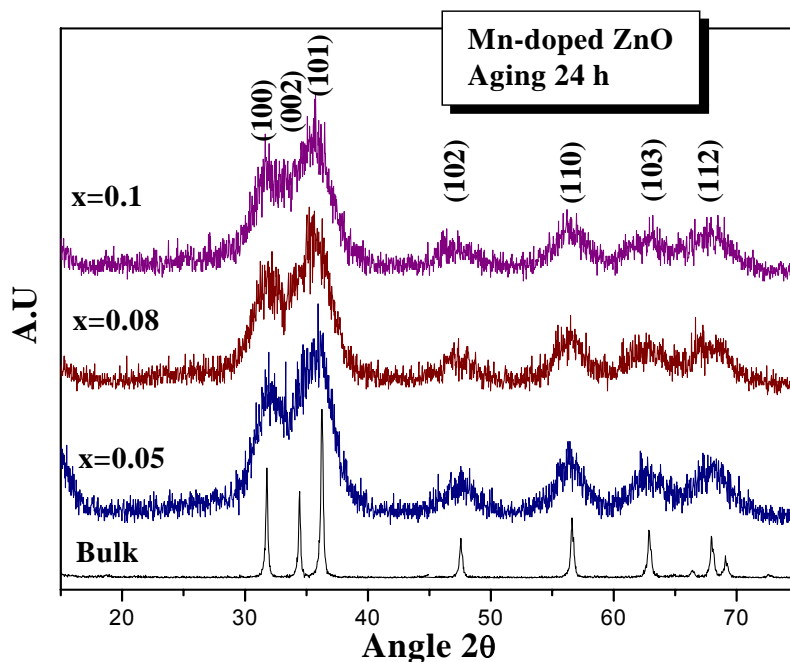


Figure 13. X-ray diffraction patterns of Mn- doped ZnO synthesized at different 'x' values and 24 hours of aging at room temperature. The complete formation of the wurtzite structure was achieved only after prolonging aging time. The XRD pattern of bulk ZnO is included only for comparison.

In order to get additional information about the role of dopant and the required length of aging, Mn- doped ZnO nanocrystals were aged in their mother liquors for prolonged times. In this regard, Figure 13 shows the XRD patterns for Mn-

doped ZnO nanocrystals aged for 24 hours. The most remarkable fact is the fully development of the ZnO structure even for 'x' values as high as 0.08 and 0.1. Evidently, longer aging times favored the conversion of the basic-Zn acetate intermediated (dehydration and atomic rearrangement) into anhydrous ZnO. Accordingly, we propose that doped ZnO nanocrystals can be synthesized under room-temperature conditions by a fine control of the aging period.

On this above basis, a more detailed monitoring of the aging stage was carried out. Figure 14 summarizes obtained results for 'x' 0.08. As observed, the non-aged solid (i.e., 0 minutes aging) consisted of incipient ZnO coexisting with precursor basic Zn-acetate, identified by vertical arrows. The intensity of the XRD corresponding to the intermediate compound decreased at prolonged aging. This evolution takes place with a simultaneous increase of the intensity for those peaks corresponding to ZnO.

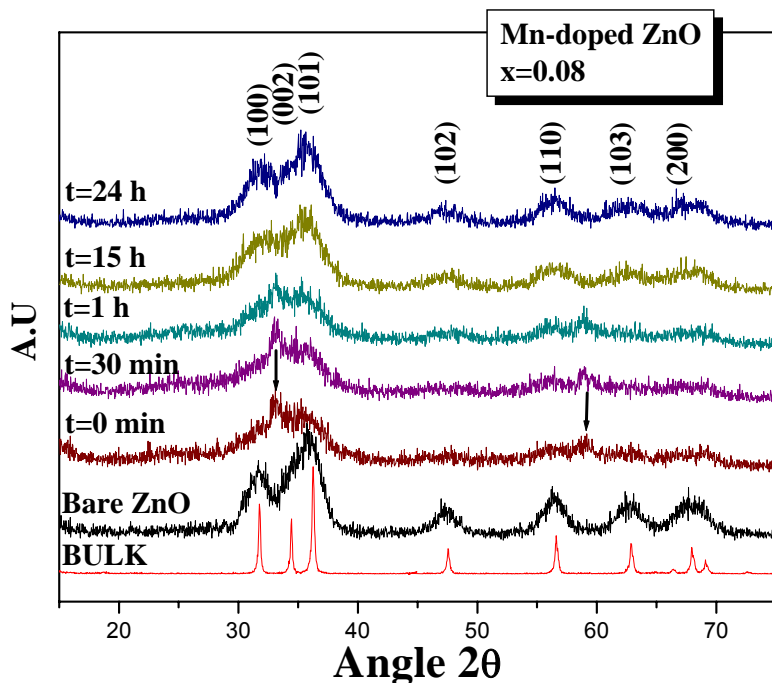


Figure 14. XRD patterns for Mn- doped ZnO nanocrystals synthesized at different aging times. The complete development of the host ZnO structure took place after 24 hours of aging for $x = 0.08$. For shorter aging times, incipient ZnO coexisted with precursor basic Zn acetate (XRD peaks are identified with arrows).

The peak of the intermediate compound was not observed after 15 hours of aging, suggesting its conversion into the oxide structure has been completed. Therefore, the above proposed inhibiting effect of the dopants on the development of the anhydrous oxide structure was confirmed. The average crystallite size of Mn-doped ZnO nanocrystals were estimated used Equation 1 and are presented in Table 2.

Table 2. Average crystallite size at different nominal Mn fraction, 'x', in ZnO and 24 hours of aging.

<i>Mn atomic fraction 'x'</i>	<i>Aging time (hours)</i>	<i>Average crystallite size (nm)</i>
0.0	24	5.4
0.05	24	3.4
0.08	24	3.3
0.1	24	3.2

The previous calculations, suggest that the presence of dopant not only inhibited the development of the oxide but also limited crystal growth, as suggested by the observed different in crystallite size with respect to bare ZnO.

Co- doped ZnO nanocrystals

Figure 15 show the X-Ray diffraction patterns corresponding to Co- doped ZnO nanocrystals synthesized at different 'x' values and aged for 24 hours. Similarly to the Mn- doped ZnO system, the presence of cobalt ions inhibited the development of the base ZnO structure. The strong dependence of nucleation on small dopant-concentrations can be attributed to the incorporation of those ions into the basic acetate cluster precursors where these impurity ions directly inhibit the nucleacion process of ZnO nanocrystals, and affecting considerably the formation of the host oxide structure.

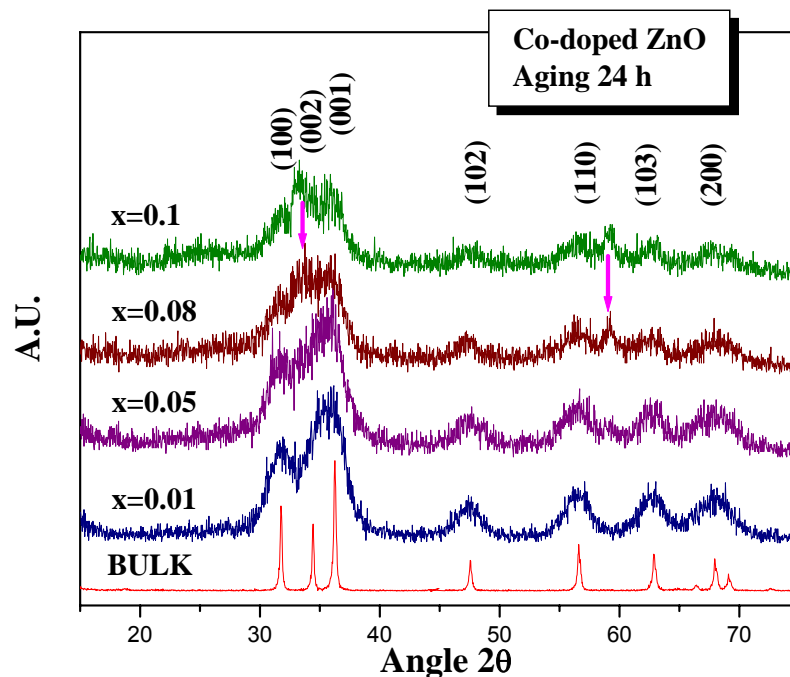


Figure 15. XRD patterns for Co-doped ZnO synthesized at different nominal atomic fractions of Co, 'x', and 24 hours of aging. Bare ZnO was formed even with no need of aging. However, a delay on the formation of host ZnO was observed when Co (II) ions were contained in starting solutions ('x' is the fraction of dopant ions in starting solutions). The precursor compound (indicated by arrows) co-existed with ZnO for $x = 0.08$ even after 24 hours of aging.

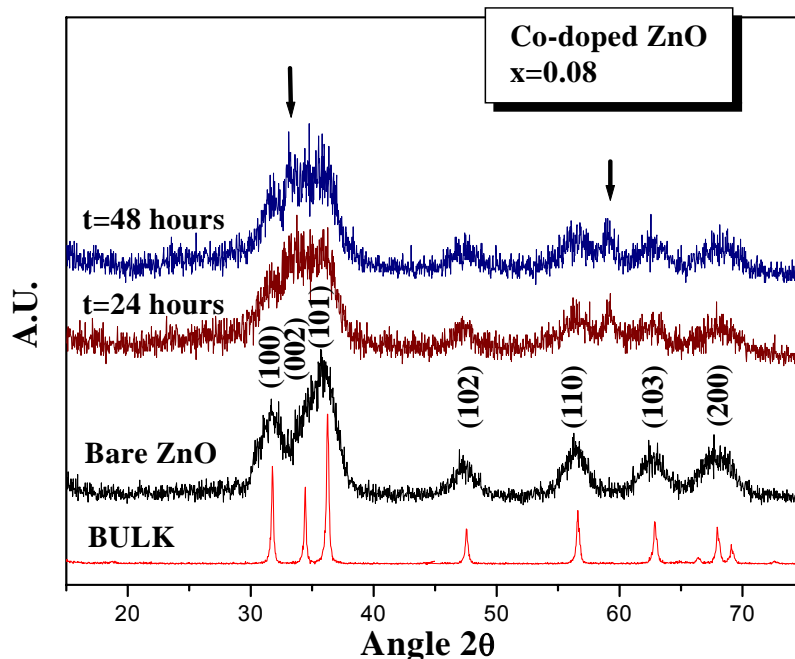


Figure 16. The delay in the complete conversion of the intermediate (black arrows) into ZnO host was even longer for $x=0.08$. Incipient ZnO coexisted with the intermediate even after 48 hours of aging at room temperature.

The intermediated compound was found in the solid for 'x' values of 0.05 and after 24 hours of aging. This intermediate was stable even after 48 hours of aging at room temperature when 'x' was 0.08 (Figure 16). For 'x' values 0.01 and 0.05 the complete development of the ZnO host structure only takes place after of 5 minutes and 24 hours, respectively. The corresponding average crystallite sizes for Co-doped ZnO powders are presented in Table 3.

Table 3. Average crystallite size for Co- doped ZnO for different 'x' values and aging time of 24 hours.

<i>Co atomic fraction 'x'</i>	<i>Aging time (hours)</i>	<i>Average crystallite size (nm)</i>
Bare ZnO	24	5.4
0.01	24	4.4
0.05	24	4.3

Ni-, Cu- and Fe- doped ZnO nanocrystals

In the case of Ni- doped ZnO system, the stability of the intermediate compound is very high even at low 'x' values. As Figure 17 evidences, the exclusive formation of the ZnO structure takes place only after 6 days aging for 'x' 0.01 and 0.02. In agreement with these results, one remarkable aspect of the involved chemistry is the sensitivity of the nucleation reaction to such a minor perturbation as replacement of Zn^{2+} by Ni^{2+} . This delay in the formation of ZnO structure can be attributed to the formation immediate precursor compound is more stable in early stage of the particle growth, as was confirmed by XRD. In the systems involving Mn^{2+} and Co^{2+} ions, for similar 'x' values, the conversion of the intermediate compound take place after an aging time as short as 30 minutes at room-temperature.

The considered intermediate compound is a basic zinc acetate (BZA) cluster which is formed by addition of base to starting zinc acetate salt. In presence of the dopant species, this BZA should have incorporated the dopants forming a mixed metal BZA that serve as immediate molecular precursor to TM^{2+} : ZnO. The presence of the dopant destabilizes ZnO critical nucleus inhibiting the ZnO nucleation, and hence the oxide development. The rate of the particle growth is governed by the concentration of precursor or conversion of dissolved species and their reactivity. This conversion should have taken place through a dissolution-recrystallization process, where the intermediate compound should have been dissolved and recrystallized as the anhydrous oxide. This type of mechanism is very common when a solid highly hydrated intermediate phase is involved with the formation of a final anhydrous phase. In the case of the Ni-doped ZnO nanocrystals, the mixed BZA seemed to be more stable even at lower concentrations of the dopants, delaying the development of the oxide phase.

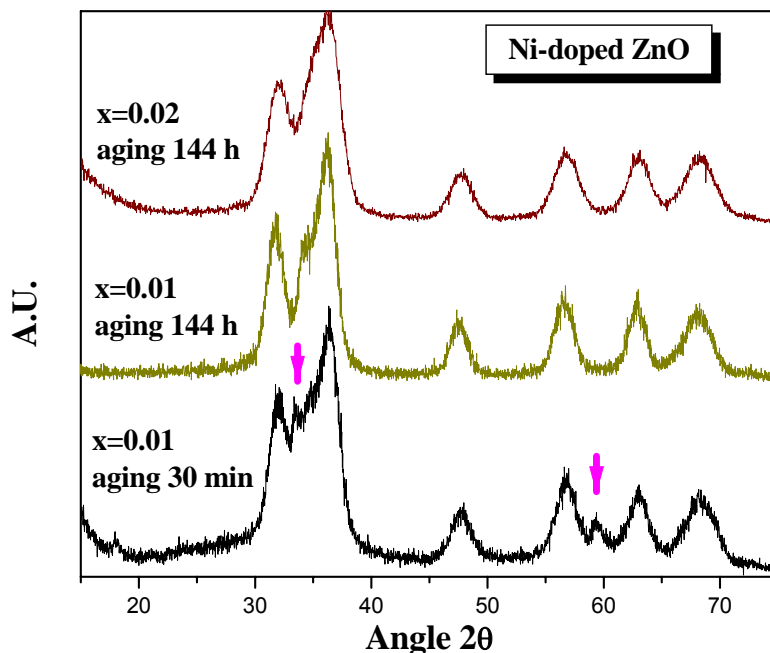


Figure 17. XRD patterns of Ni- doped ZnO nanocrystals synthesized at different 'x' values and aging times. The ZnO host structure was delayed when 'x' was increased. The complete formation of the wurtzite structure no achieved after prolonging aging (6 day). For higher 'x' values, longer aging time required to fully develop the zinc oxide structure.

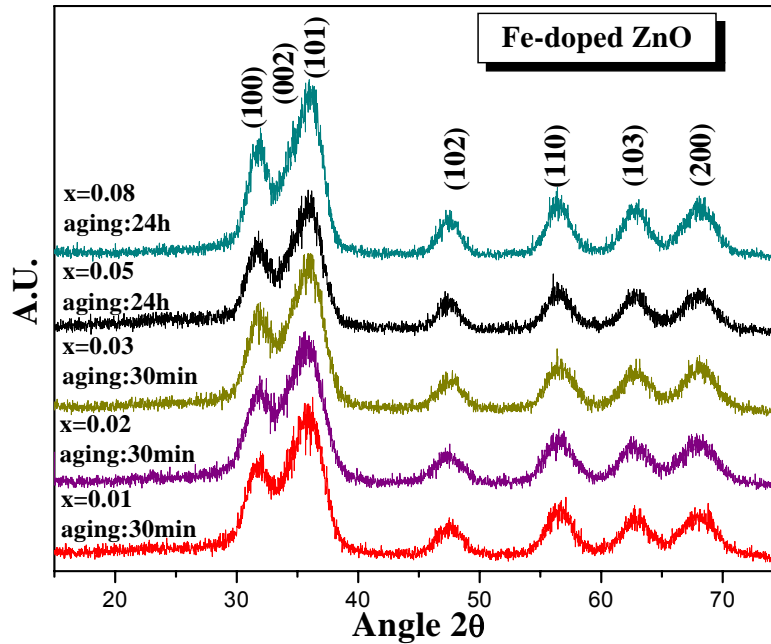


Figure 18. XRD patterns of Fe- doped ZnO nanocrystals synthesized at different 'x' values and aging times. The complete formation of the Fe-doped ZnO wurtzite structure took place even after an aging time as short as 30 minutes. The formation of intermediate phases was not evidenced for this time of aging.

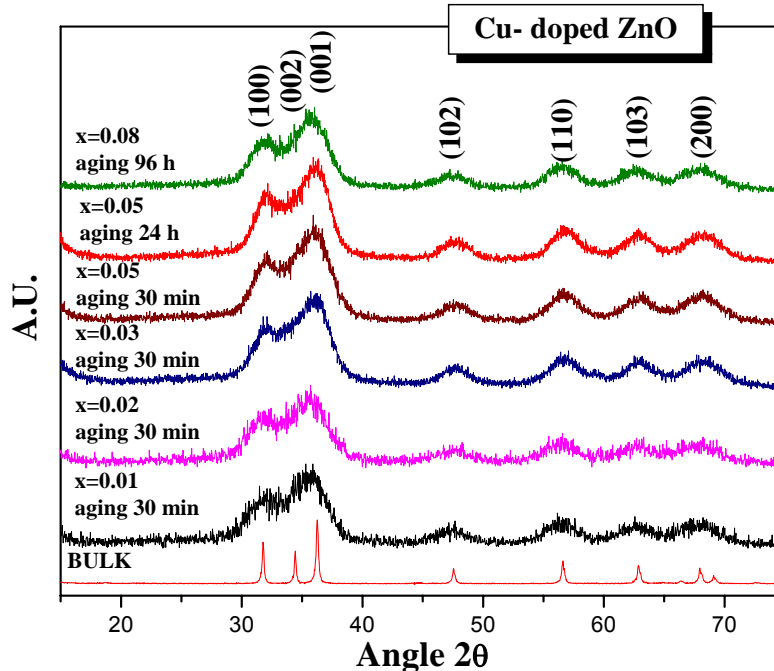


Figure 19. XRD patterns for Cu- doped ZnO synthesized at different 'x' values and aging times. The formation of intermediate phases was not evidenced for this time of aging.

Figure 18 and 19 show the XRD patterns corresponding to Cu- and Fe-doped ZnO nanocrystals, respectively. In contrast with the Ni-doped ZnO system, the formation of the base ZnO structure took place with no need for long aging. An aging time of 30 minutes was enough to fully develop the oxide structure for 'x' values as high as 0.08 in both systems. No peak of the intermediated phase was observed. We think that Cu- and Fe-bearing mixed BZA should have exhibited similar room-temperature solubility in ethanol as in Co- and Mn-systems. The estimated average crystallite sizes are presented in Table 4.

Table 4. Average crystallite size for of Ni- doped ZnO for different 'x' values and 144 hours of aging.

<i>Ni atomic fraction 'x'</i>	<i>Aging time (hours)</i>	<i>Average crystallite size (nm)</i>
0.0	24	5.4
0.01	144	4.8
0.02	144	3.8

The estimated average crystallite sizes are presented in Tables 5 and 6.

Table 5. Average crystallite size of Fe- doped ZnO for different 'x' values and 30 minutes of aging.

<i>Fe atomic fraction 'x'</i>	<i>Aging time (minutes)</i>	<i>Average crystallite size (nm)</i>
0.0	20	4.5
0.01	30	3.4
0.02	30	3.3
0.03	30	3.2

Table 6. Average crystallite size of Cu- doped ZnO for different 'x' values and aging time of 30 minutes.

<i>Cu atomic fraction 'x'</i>	<i>Aging time (minutes)</i>	<i>Average crystallite size (nm)</i>
0.0	20	4.5
0.01	30	3.4
0.02	30	3.2
0.03	30	3.1
0.05	30	3.0

The above presented results suggest the strong influence of the type and amount of dopants on the nucleation and growth processes involved with the development of the ZnO structure. The observed effect on the length of aging needed to achieve the oxide structure and the estimated average crystallite sizes, which were always smaller than for bare ZnO, can be attributed to the incorporation of the dopant ions into the oxide structure. The immediate precursor to ZnO nucleation has been identified as basic zinc acetate (BZA) cluster which form with addition of base (LiOH) [47].

During synthesis, the addition of the hydroxide is thus likely consumed to form mixed metal BZA that serves as molecular precursor to the oxide. The presence of BZA will be predominant in early stages of particle growth, as was confirmed by our XRD measurements. The enhanced stability of the intermediate compound in presence of dopant ions can be attributed to the very small dimensions of the critical nuclei which are responsible for the predominance of the less crystalline and more hydrated intermediate compound. Therefore, subsequent crystal growth during aging should have favored the stability of the crystalline phase, ZnO in this case.

The introduction of the different transition metal in the reaction has a large impact on the yield of the reaction. Reaction produced as a function of the dopant concentration and aging time reveal a decrease in ZnO produced with increasing dopant concentration. This is one of the manifestations of ZnO critical nucleus are destabilization by dopant ions it can be attributed to the inability of mixed-metal BZA cluster to nucleated the wurtzite lattice structure. For instance, in the Ni- doped ZnO system the complete formation of the ZnO host structure was only achieved after six days of aging, for a nominal ‘x’ value as low as 0.02. This result contrasts with those observed for the other studied systems (Mn-, Co-, Cu-, and Fe- doped ZnO) where complete conversion of the intermediate compound into the oxide phase took place after only 30 minutes of aging for a similar ‘x’ of 0.02.

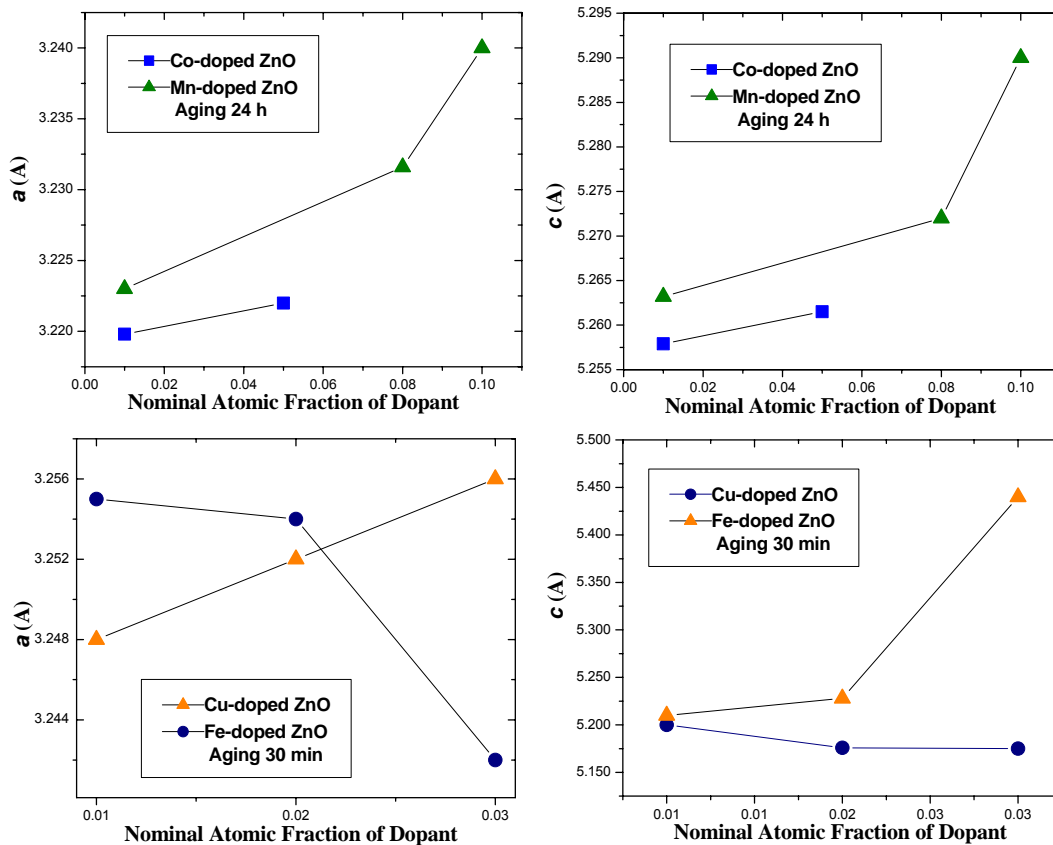


Figure 20. Lattice parameters a and c for wurtzite phase determined from XRD patterns for TM-doped ZnO nanocrystals. Lattice parameters for bare ZnO were $a = 3.250 \text{ \AA}$ and $c = 5.20 \text{ \AA}$.

The generalization of this conclusion can be supported by comparison of lattice parameters calculated for different transition metal doped ZnO powders. Despite the very small difference of tetrahedral ionic radii of dopant species ($\text{Mn}^{2+} \sim 0.8 \text{ \AA}$, $\text{Co}^{2+} \sim 0.72 \text{ \AA}$, $\text{Ni}^{2+} \sim 0.72 \text{ \AA}$, $\text{Cu}^{2+} \sim 0.69 \text{ \AA}$ and $\text{Fe}^{2+} \sim 0.74 \text{ \AA}$) with that of host Zn^{2+} ($\sim 0.74 \text{ \AA}$), it is large enough to control the course of the reaction in the early stage of the aging stage. Then, the substitution of dopants to the ZnO lattice can induce a strain that would manifest itself as a distortion of the unit cell of the host ZnO on dopant concentration.

Lattice parameters in bare and doped-ZnO nanocrystals

When a material is actually doped there is no appearance of new X-ray diffraction peaks, but instead gradual shifts in the angular positions of the XRD peaks corresponding to the host material are observed. These shift evidences changes in the lattice parameters of the host by incorporation of the dopant ions into the basic unit cell. The shift in XRD peaks position can also occur from the strain induced in the unit cell when the dopant is incorporated into the periodic lattice. On this basis, we have calculated the variation in lattice parameters of host ZnO as a function of the amount and type of dopant. The results can be summarized in the Figure 20.

The variation in the lattice parameters with dopant concentration in the crystal can be understood as a phase transition or actual incorporation of dopant into the unit cell of the host structure. This variation of lattice parameters with dopant concentration can be explained by the Vegard's rule. This rule holds that a linear relation exists, at constant temperature, between the crystals lattice constant of an alloy and the concentration of the constituent elements [93]. Although we are using the nominal 'x' nominal value (atomic fraction of dopant in starting solutions) and not the actual 'x' value in the solids, we could use the Vegard's law only on a qualitative basis. Therefore, the dopant-induced strain in doped

ZnO quantified by determination of the lattice constants $a_{Zn_{1-x}TM_xO}$ and $c_{Zn_{1-x}TM_xO}$ as a function of 'x' is presented in Figure 20.

The a and c -axis lattice parameters were calculated for Co- and Mn-doped ZnO nanocrystals aged for 24 hours. The (102) peak position of the Co- and Mn-doped ZnO shifted to lower angles when increasing Mn and Co concentration. As the data given in table 20 indicates, a larger c -axis lattice parameter was observed for Mn-doped in comparison with Co-doped samples. Although this behavior is expected according to the difference between ionic radii r of tetrahedral coordination Mn^{2+} (0.8 Å) with respect to Zn^{2+} (0.74 Å), the large variation of a and c – parameters ('x'= 0.01) could be due to formation of another phase transition or segregation at this highest concentration which was not detected by XRD analysis. For the case of cobalt a slight increment in the lattice parameters a and c was observed when increased the concentration of the magnetic ion. Based on the size compatibility between Co and Zn ions (Co^{2+} ionic radii, 0.74 Å), this dependence of lattice parameters with the amount of dopant species can be attributed to an actual incorporation of the dopant species into ZnO structure.

It must be emphasized that for nanocrystals the interpretation of calculated lattice parameters and the precise positioning of broad XRD peaks is a very challenging task. Therefore, we can not discard some error of appreciation in our calculations. In the case of Cu- and Fe- doped ZnO nanocrystals, a slight but systematic decrease in a and c parameters was observed. This decrease in the lattice constant can be attributed to actual incorporation of Cu in the ZnO structure. This behavior was to be expected since the ionic radius of Cu^{2+} (0.64 Å) is smaller than the Zn^{2+} (0.74 Å). Similar behavior but with increment in the lattice parameters was observed for the case of Fe- doped ZnO system. The ionic radius of Fe^{2+} is 0.74 Å. The similitude between ionic radius of Fe and Zn ions explains the rapid incorporation of these species into the ZnO unit cell;

however, probable strains due to this incorporation could be related to the observed shifts in the angular position of the XRD peaks.

4.2 HRTEM ANALYSES OF SYNTHESIZED NANOCRYSTALS

ZnO nanocrystals were grown for a suitable aging time, coagulated by n-heptane and redispersed in fresh ethanol solution. Once nanocrystals were redispersed, two drops were placed on a grid of amorphous carbon and dried slowly at room temperature.

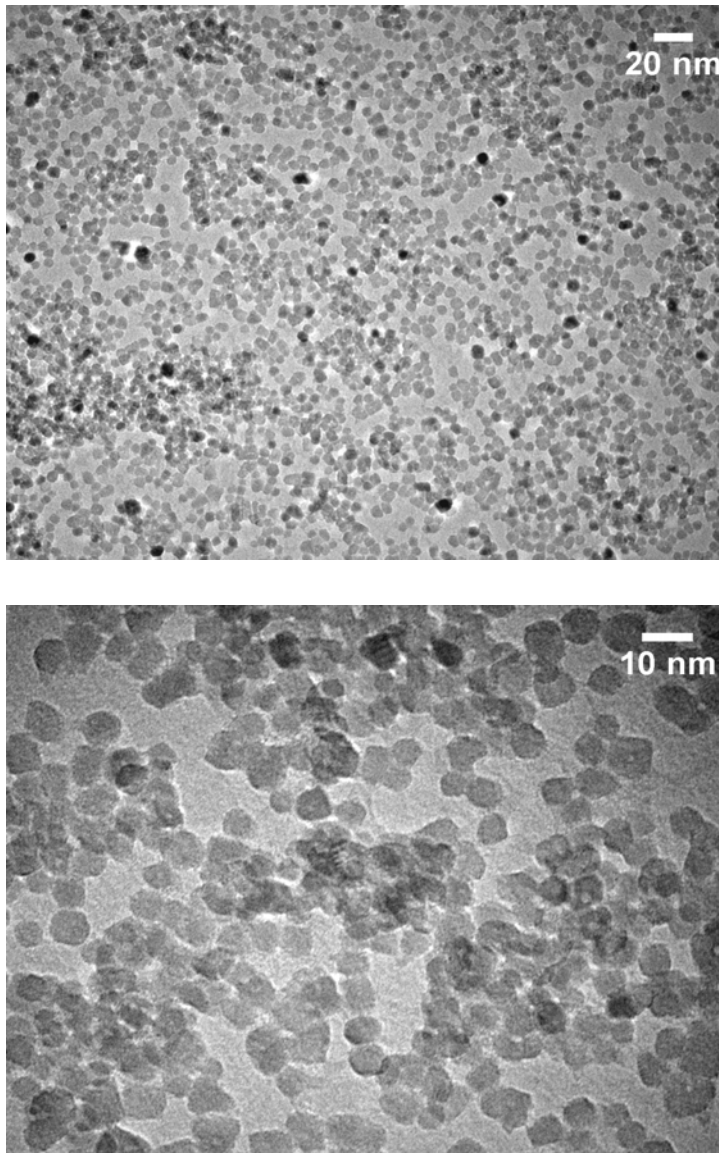


Figure 21. HRTEM micrograph of ZnO nanocrystals produced after 20 minutes of aging time. The picture evidenced the high monodispersity of the 5-8 nm nanocrystals.

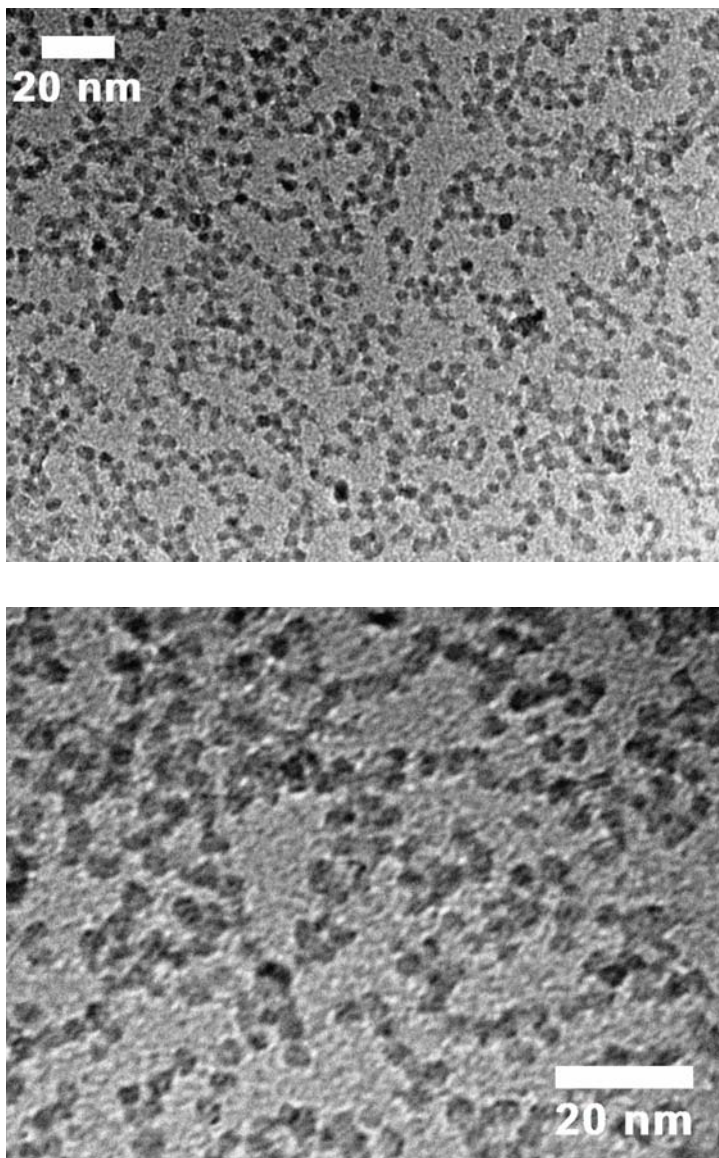


Figure 22. HRTEM pictures of 24 hours-aged Mn- doped ZnO ($x=0.05$) nanocrystals. The high monodispersity is also observed in the 3-5nm particles.

Figures 21 and 22 correspond to bare ZnO and Mn- doped ZnO nanocrystals synthesized for $x = 0.05$ and aged for 20 minutes and 24 hours, respectively. The particle size was estimated to be between 5 - 8 nanometers for bare ZnO nanocrystals and 3-5 nm for Mn- doped ZnO. These values are in excellent agreement with XRD estimations, which suggests each individual is a single crystal. Moreover, the nanocrystals were highly monodisperse. The nanometric

size and the sharp size distribution is a consequence of a very fast nucleation rate, coupled with a protective net charge on the surface of nanocrystals caused by the adsorption of acetate species (as suggested by FT-IR measurements to be discussed in the following section).

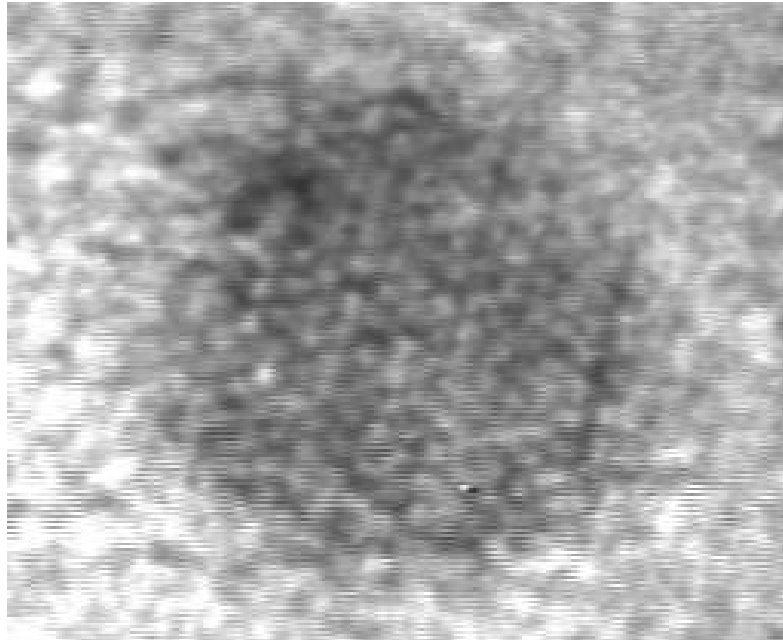


Figure 23. HRTEM micrograph evidences the highly crystalline nature of a single ZnO crystal; the lattice image can be clearly observed.

The Figure 23 shows the HRTEM image of a single crystal of ZnO. The crystalline nature of ZnO nanoparticle is evidenced by the clearly observed lattice features.

4.3 FT-IR MEASUREMENTS

Infrared (IR) spectroscopy is one of the most common spectroscopic techniques used by organic and inorganic chemists, which has become a powerful tool used for determined the structural elucidation and chemical functional groups in the sample.

4.3.1 FT-IR measurements for bare ZnO nanocrystals

FT-IR measurements were undertaken in order to confirm the formation of crystalline ZnO nanocrystals and identify any adsorbed species onto the crystals surface. Figure 26a shows the IR spectra for bare ZnO nanocrystals without and with washing with fresh ethanol solutions. The spectrum for bulk ZnO is also included only for purposes of comparison. Bulk ZnO is commonly produced at high temperatures (far above 200 °C).

Bands at 525 cm^{-1} is assigned to the stretching vibrations of Zn–O ($\nu_{\text{Zn-O}}$). In addition to those bands, another strong one was observed between 1350 cm^{-1} and 1600 cm^{-1} . These bands persist even after intense washing with ethanol. These three intense bands were centered at 1342 cm^{-1} , 1420 cm^{-1} and 1574 cm^{-1} and are attributed to the stretching vibration of C=O ($\nu_{\text{C=O}}$), C=C ($\nu_{\text{C=C}}$) and C–H ($\nu_{\text{C-H}}$) groups in acetates species, which suggests its presence as adsorbed species in the surface of nanocrystals. The broad absorption peak centered 3418 cm^{-1} correspond to –OH group of H₂O, indicating of existence of water absorbed on the surface of nanocrystals. Based on our results, we can attribute the high monodispersity observed in the nanocrystals to the fast nucleation in ethanol medium, coupled with electrostatic repulsion arising from negatively charged impurities coming from adsorbed acetate species on the surface of the nanocrystals (Figure 24). These adsorbed species should provide a net negative surface charge of the nanocrystals, which restricted crystal growth and aggregation due to repulsive electrostatic interactions.

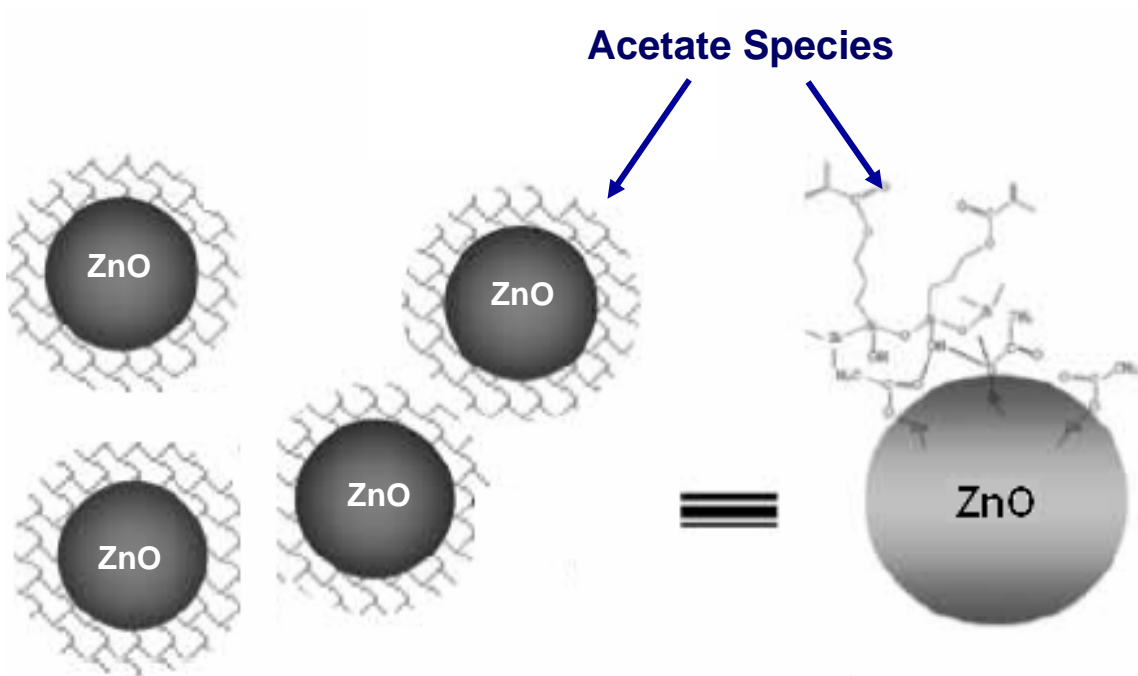


Figure 24. The high monodispersity exhibited by bare and doped-ZnO nanocrystals can be attributed to the acetate species strongly adsorbed on the surface of the nanocrystals.

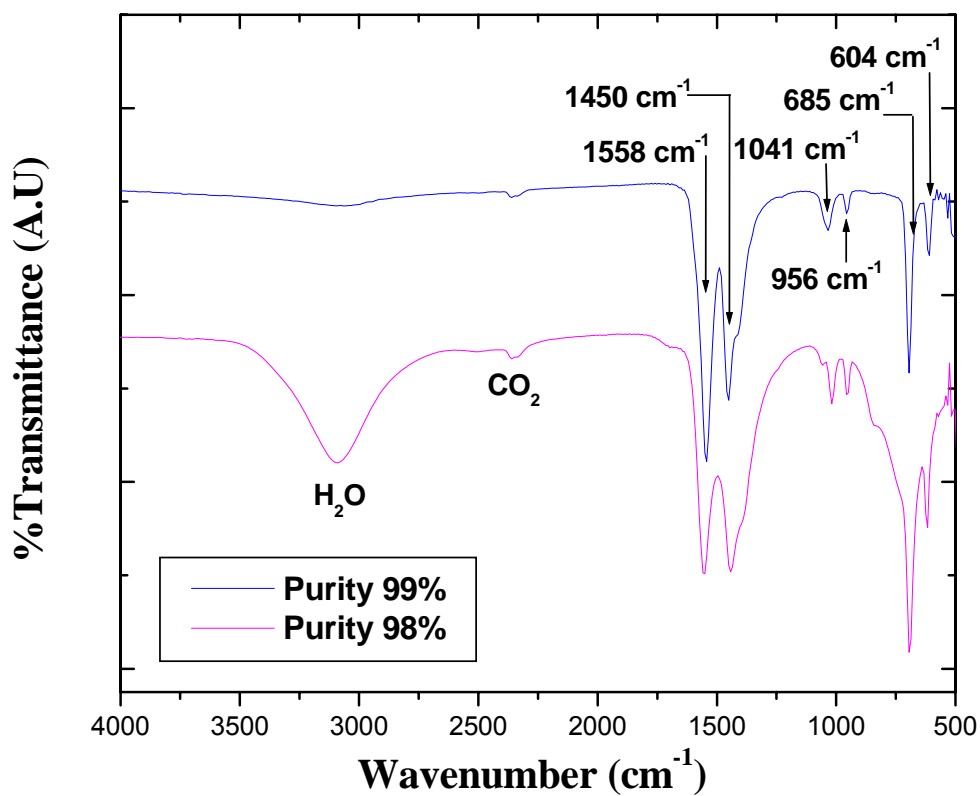


Figure 25. FT- IR spectra of two types of zinc acetate.

4.3.2 Doped ZnO nanocrystals

ii) Effect of type of dopant

The FT-IR spectra for the doped-ZnO nanocrystals showed similar features for the bare ZnO. Figure 26b shows the FT-IR spectra for doped ZnO samples produced at $x = 0.01$ and 30 minutes of aging. Spectra were recorded in air at room temperature. The bands around 3400 cm^{-1} correspond to the O–H mode in molecular water. The presence of this band can be attributed to the adsorption of some atmospheric water during FT-IR measurements. Also in this case, the presence of band corresponding to acetate species are clearly observed in washed samples.

iii) Effect of aging time: the case of Mn-ZnO

Mn- doped ZnO nanocrystals, $x = 0.08$ (Figure 27), were selected to investigate the effect of aging. The basic information is the same as discussed previously. However, it was observed a systematic rise in the intensity of the Zn-O band by prolonging the duration of the aging stage, which is a clear evidence of the enhancing effect of aging on the crystallinity of the ZnO host structure; i.e., the longer the aging time, the more ordered (larger crystals) the oxide structure. This statement is in excellent agreement with the information provided by XRD measurements.

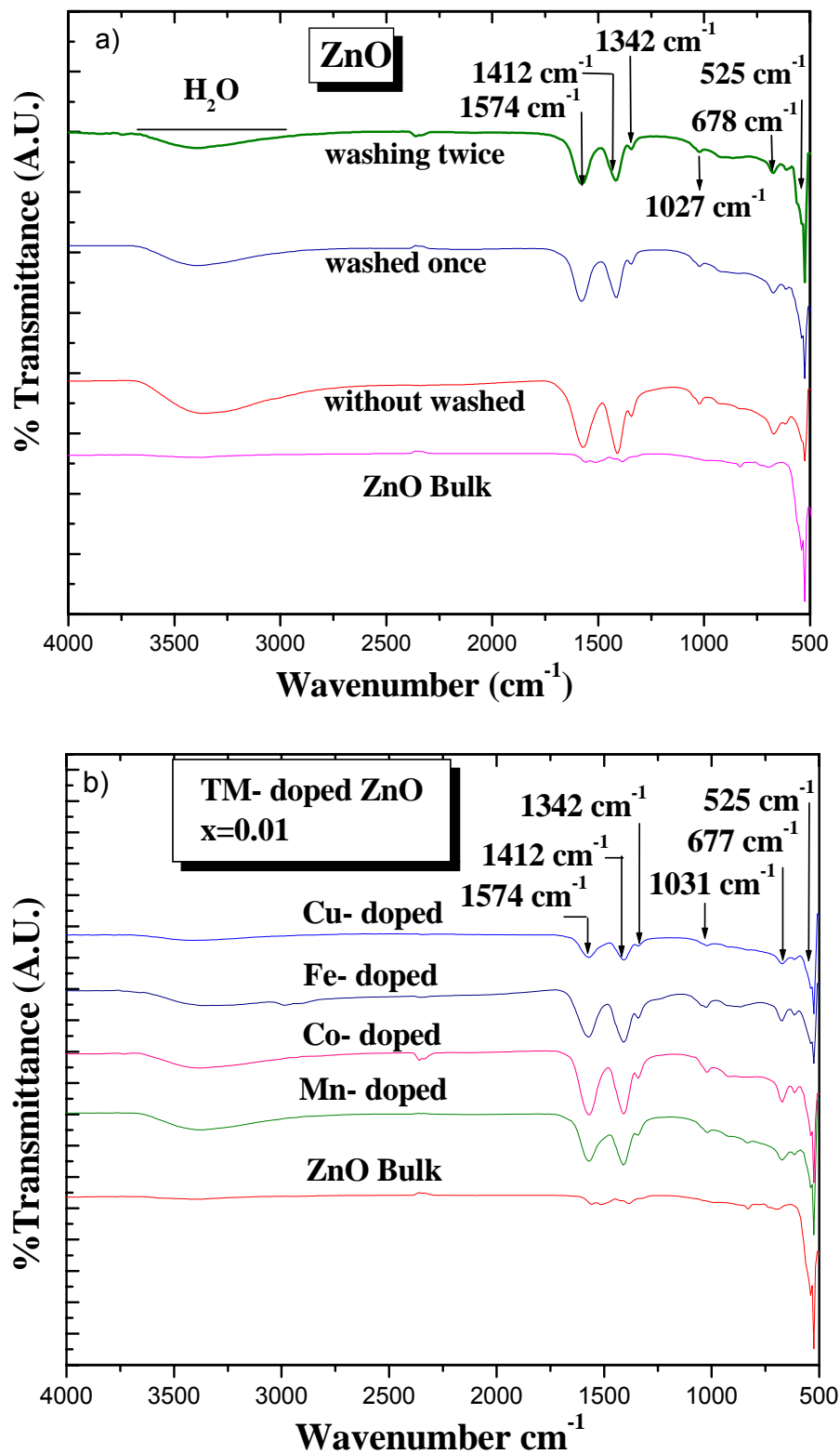


Figure 26. a) FT-IR spectra ZnO nanoparticles. b) FT-IR measurement of TM– doped ZnO. The presence of acetate species coexisted even after intense washed for bare and TM doped ZnO.

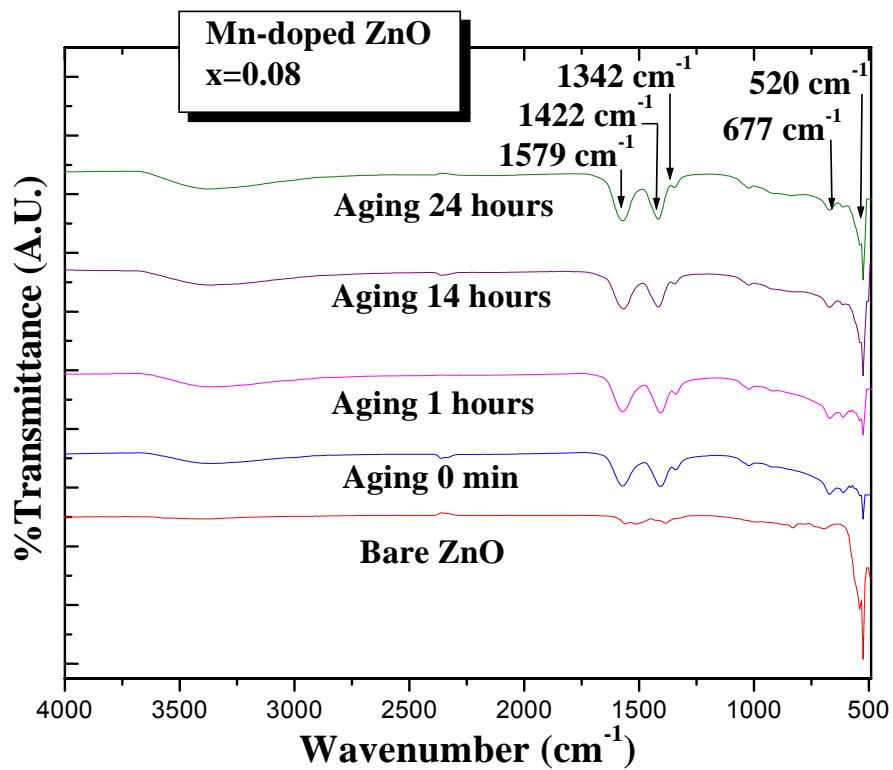


Figure 27. FT-IR spectra of Mn-doped ZnO nanocrystals ($x = 0.08$) synthesized at different aging times. As seen, prolonged aging favored the development of the ZnO structure. The bands of acetate species were detected even after intensive washing of the solids, suggesting the acetate is present as adsorbed species.

4.4 ULTRAVIOLET-VISIBLE ABSORPTION SPECTROSCOPY

A solid material can be categorized as metal or semiconductor depending on their ability to conduct electrical charge. On a microscopic level, this implies that the metal exhibits a strong overlapping between the valence and conduction bands, which allows the electron to move freely through the material, and thus given rise to charge conduction. Semiconductor materials have fully filled valence band and the entirely empty conduction band. The valence and conduction band, are found separated by a region of forbidden range energy. Semiconductors behave very differently, in comparison with bulk, when their crystal sizes are reduced down to the order of a few nanometers. One of the most significant characteristic in these materials is the variation of the band gap when the sizes of nanocrystal decrease below this Bohr exciton radius a_B .

This technique is used because the electronic band structure of semiconductors and metals are determined by their optical properties. The optical absorption is a result of interaction between the material and light. When a frequency of light is on resonance with the energy difference between states the transition allowed or partly allowed by selection rules, and photon is absorbed by the material which is reflected as a decrease of transmission or an increase in absorbance of the light passing through the sample. By measuring the transmission or absorbance of sample as a function of the frequency of the light, one can obtains a spectrum characteristic of the material.

4.4.1 Crystal growth monitoring.

Bare ZnO nanocrystals

In order to monitor the crystal growth during aging, UV-Vis absorption spectra were recorded at room temperature from stable transparent suspensions of aged ZnO nanocrystals in ethanol. UV-Vis absorption spectra provide a convenient

way to investigate the particle growth. It is well established that when the particle size of a semiconductor becomes to the Broglie wavelength of an electron or hole, the three dimensional quantum confinements, imposed by the dimensions of the nanocrystal, occurs. This influence of nanocrystals size on the electronic structure of semiconducting materials is represented by a marked increased in the band gap, which is attributed to the so-called quantum confinement effect.

Ten minutes after mixing the zinc acetate with the LiOH solution the absorbance spectra show a well-defined exciton peak, which suggests a very fast nucleation. Besides, a meaningful red-shift in the absorption peak was observed when the aging time varied from zero to 24 hours (Figure 28 a). The change between the corresponding two absorption peaks was ($\Delta E=0.249$ eV). This significant red-shift is attributed to the fast crystal growth during the early formation stage of the bare ZnO nanocrystals.

On the other hand, UV absorption measurements can also provide a qualitative indication of the crystal size distribution. The sharp excitonic peak in the absorption spectra in the case of small nanocrystals (Figure 28 b) is indeed indicative of the narrow size distribution of the nanocrystals in the sample, as confirmed by TEM analyses. In case the size distribution is broad, there would be a number of exciton peaks appearing at different energies corresponding to different sized nanocrystals and overlapping with each other. Accordingly, sharp excitonic features will not be appreciated in the absorption spectra, but only a broad and featureless absorption edge. The crystal growth observed during aging time could be stopped by coagulation with n-heptane and subsequent redispersion in ethanol. To verify the restriction on crystal growth, UV-Vis measurement was carried out on redispersed nanocrystals coagulated after 5 minutes, 1.5 hours and 3 hours of aging (Figure 29). Each curve in the figure corresponds to five observations performed in 15 minutes intervals. The inhibition in crystal growth was evidenced by the invariable position of the absorption peak for each sample.

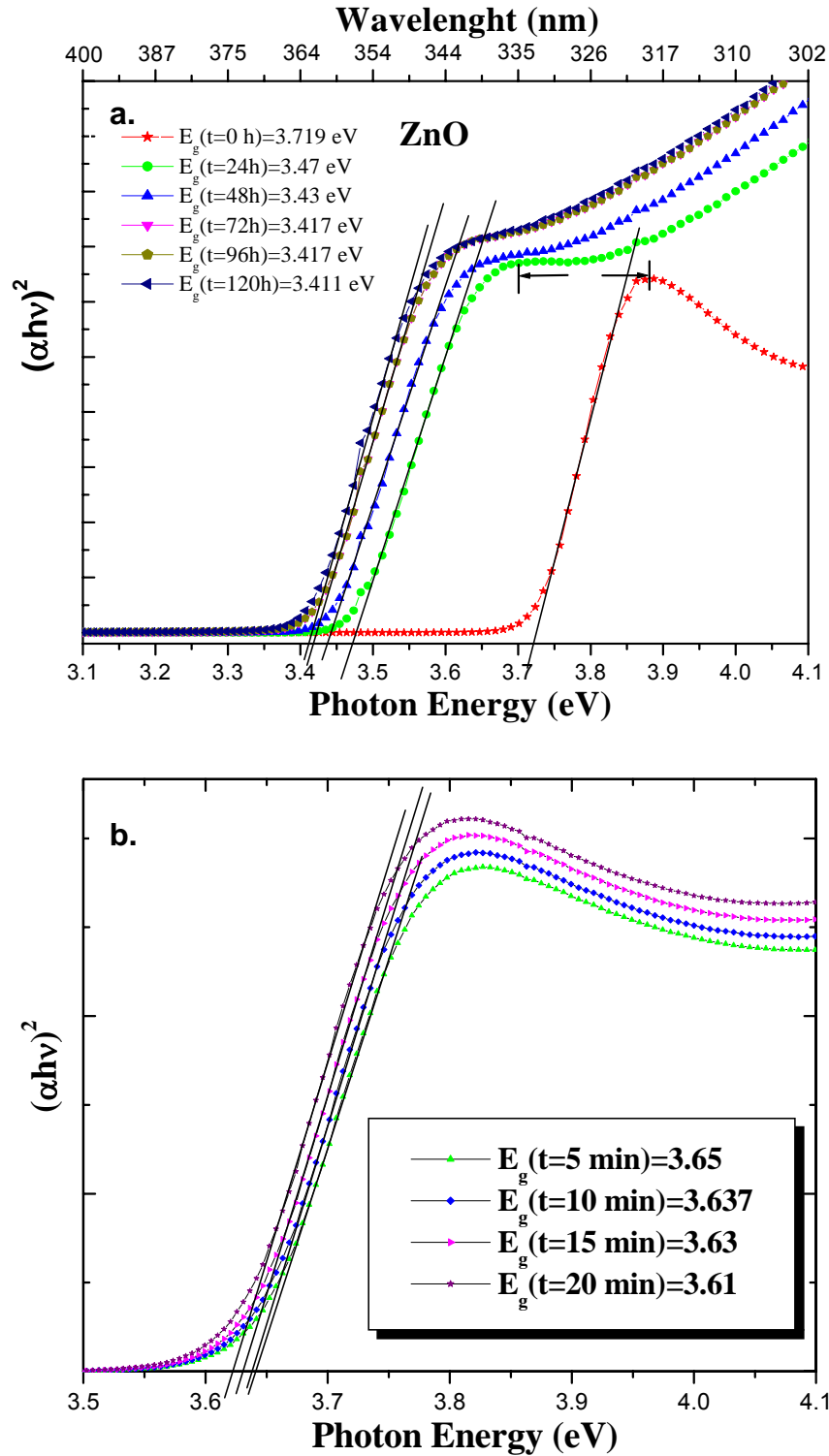


Figure 28 (a) and (b). ZnO absorption spectra taken at various aging time. Red-shift in the absorption pick was observed between interval time 0 minutes and 24 hours (the change between two absorption position pick was $\Delta E=0.249 \text{ eV}$), which indicated a fast particle growth for early stage of formation of the nanocrystals.

Table 7. Estimated band gap energies and corresponding nanocrystal sizes as a function of aging time. A marked decrease in confinement energy by increasing particle size became evident.

<i>Aging time</i>	<i>Energy gap (eV)</i>	<i>Nanocrystal size (nm)</i>
0 minutes	3.719	3.59
5 minutes	3.65	3.87
10 minutes	3.637	4.1
15 minutes	3.63	4.14
20 minutes	3.618	4.46
24 hours	3.47	5.39

The shoulder in the absorption spectrum is attributed to optical transition to the excitonic stated (electronic transition from the top of the valence band to the bottom of the conduction band). The most important thing to notice is that between the occupied bands and the empty bands there is a gap, this is energy difference between the full and empty electron state. These filled states are called the *valence band*, and the energy at the top of the valence band is conventionally the zero of energy and is called the *valence band edge*.

The empty states above the gap are called the *conduction band*. The lowest point in the conduction band is called the *conduction band edge*. For the ZnO the conduction band edge is located at $k=0$, the Γ - point, which is also the k -value of the valence band edge. Since for ZnO the valence band and the conduction band edges occur at the same k -value, the material is called a direct band gap.

For each spectra we have calculated the band gap energy for samples at different aging times for those conditions where the valence band maximum and conduction band minimum occur at the same wave vector (i.e., at $k=0$) the energy gap dependence of the absorption constant can be considered proportional to the density of final state

$$\alpha(h\nu) = A(h\nu - E_g)^{m/2} \quad (4)$$

Where α is the absorption coefficient, $h\nu$ is the photon energy, A is a constant and $m=1$ represents a direct transition between bands (valence band and conduction band). E_g was calculated from the UV-Vis spectra by extrapolating a straight line from the absorption curve to the abscissa axis. When α is zero, then $E_g=h\nu$.

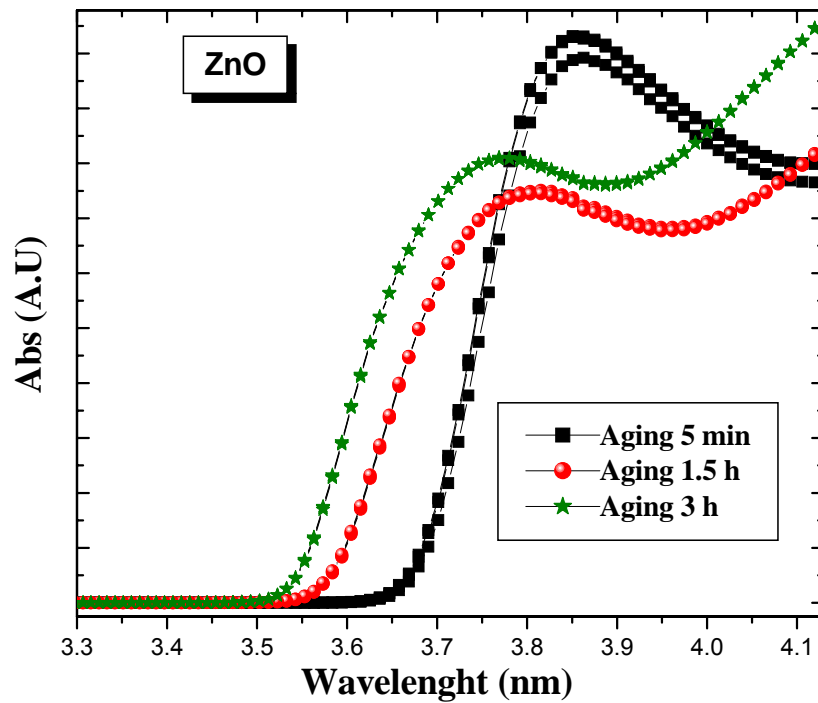


Figure 29. UV-visible analyses confirmed the inhibition of crystal growth when the ZnO nanocrystals were rapidly coagulated by n-heptane and redispersed in fresh ethanol solutions.

Doped-ZnO nanocrystals

Figure 30a shows the absorption spectra for suspensions of nanocrystals of different doped ZnO for 24 hours of aging and 'x' = 0.01.

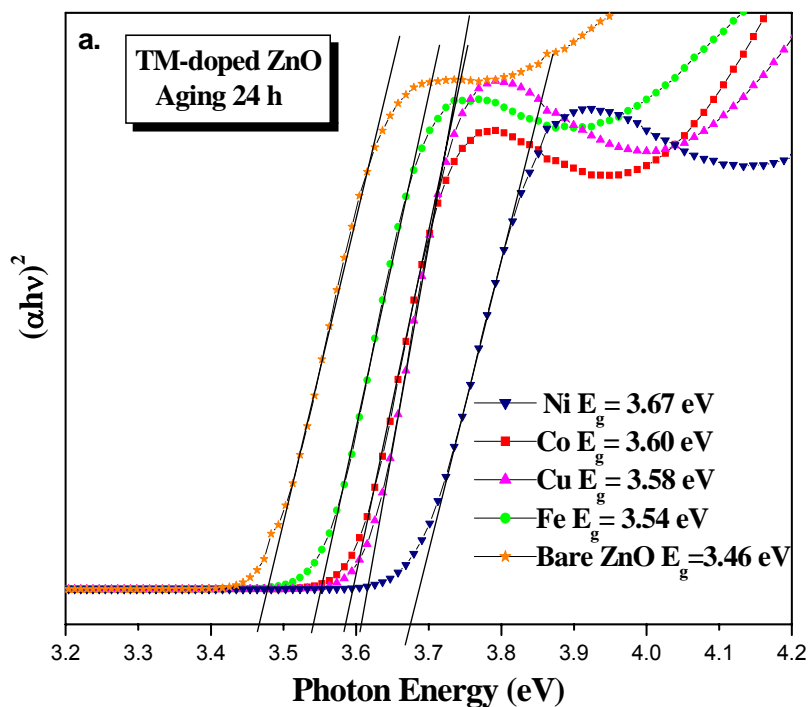


Figure 30a. UV-Vis spectra absorption spectra of suspension of TM- doped ZnO nanocrystals for a dopant atomic fraction of 1% and 24 hours of aging.

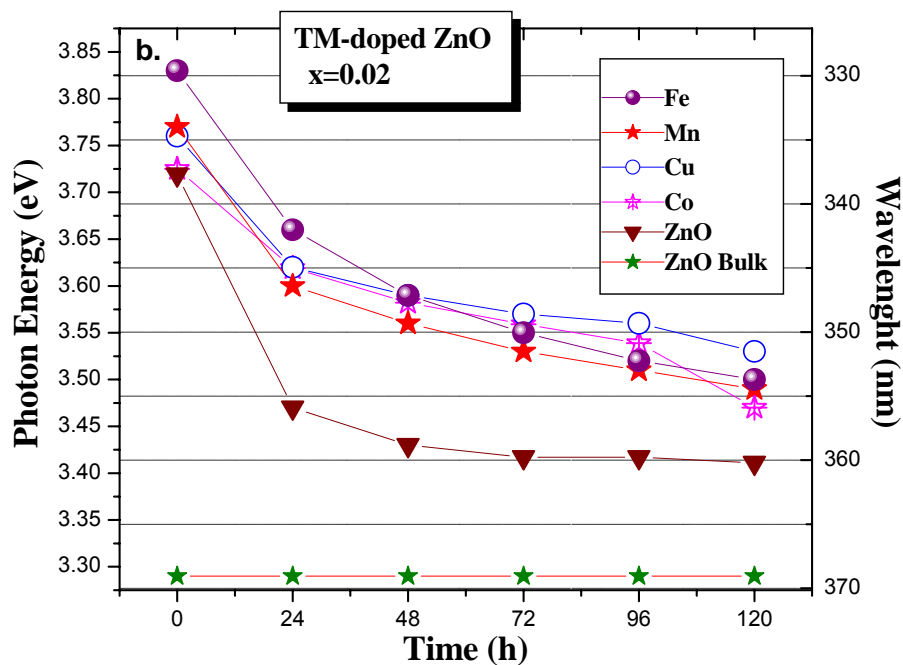


Figure 30b. Variation of band gap with aging time in TM- doped ZnO nanocrystals. Large energy gap was observed as a consequence direct from the strong quantum confinement of the electron due to the reduced particle size. After of 24 hours of aging an abrupt change in the optical band gap to lower energy was observed for all systems. This change correspond to a blue shift with respect to the energy of the bulk material, which can be attributed to the slowly growth of the particle.

Figure 30b. describes the variation of the energy gap in function of aging time, for all doped ZnO nanocrystals synthesized for $x = 0.02$. A clearly effects is visible from these spectra. A continuous decrease of the photon energies by prolonging the length of the aging period and on the other hand, the continuously particle grow.

It is clearly observed a shift of the absorption peak toward higher energies, in comparison with bare ZnO. In the case of Ni- doped ZnO, the band gap energy was estimated in 3.67 eV (338 nm) for an aging time of 24 hours, a large value in comparison with that for bare ZnO 3.46 eV (358 nm) under similar aging conditions. This behavior suggests the inhibition of crystal growth by incorporation of dopant ions into ZnO host structure.

The band gap values determined for bare ZnO and Co-, Cu-, Mn- and Fe- doped nanocrystal with no aging time (i.e., right after 10 minutes of contact) were 3.71 eV (334 nm), 3.725 eV (332 nm), 3.76 eV (329 nm), 3.77 eV (328 nm) and 3.83 eV (323 nm) respectively. The values corresponding for samples aged for 24 hours were 3.47 eV (357 nm), 3.62 eV (342 nm), 3.61 eV (343 nm), 3.6 eV (344 nm) and 3.66 eV (338 nm). Second, at early stages of particle growth in all case the absorption spectra exhibited a distinct maximum directly after the onset absorption. This feature becomes less pronounced as the aging process progresses. Both defects can be understood in terms of a decrease in quantum confinement upon particle growth. As the particle increase, the band gap gradually shifts towards the value for bulk ZnO (~3.2 eV).

A noticeable change in the excitonic emission was observed as consequence of the confinement of the wave function; when the concentration of dopant was increased. Figure 31 shows the band gaps of TM- doped ZnO nanocrystals, obtained from the extrapolation of the linear part until intercept of energy axis versus concentration. In agreement with our previous result we can point out that ZnO nucleation is sensitive to the chemical properties of dopant impurities. This

sensitivity can be studied quantitatively by comparison of ZnO band gap intensities, of absorption spectra corresponding to these nanocrystals (which show a monotonic increment of the band gap with relation to the dopant concentration) measured from synthesis with and without dopants, under identical conditions.

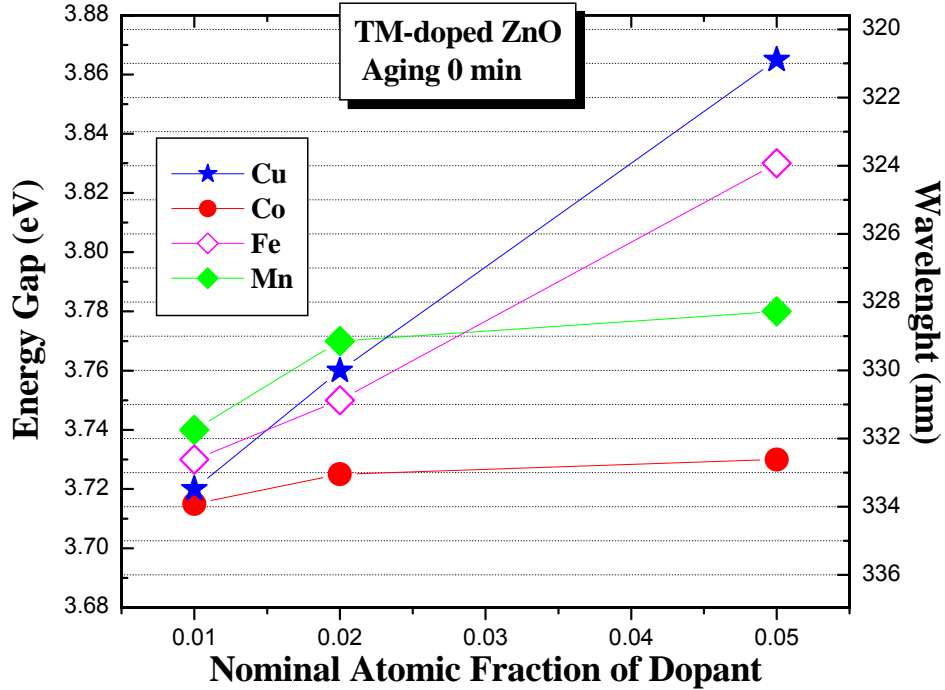


Figure 31. Variation of band gap with the percentage of TM doping in nanocrystals.

As shown in Figure 31, the number of nucleated nanocrystals depends very strongly on the initial dopant ion concentration when increase the atomic fraction dopant in starting solution. Accordingly, we can conclude that the impurity ions directly inhibit the nucleation of ZnO nanocrystals, as has also been suggested from our XRD data. On the other hand, band gap energies obtained in the presence of dopants are significantly greater than those values for bare ZnO nanocrystals synthesized under identical conditions. These results may indicate that the resulting nanocrystal dimensions are reduced by doping at early stages

of the formation of the ZnO structure. As we say before the actual gap is much larger and consequently smaller particles are present. Another reason for the observed rise in the band gap energies with doping can be a lattice mismatch caused by the dopant incorporation, which can introduce strain during the growth of ZnO nanocrystals in presence of the dopants, resulting in the accumulation of large strain energies. Strain energy is released by breakdown in growth through the formation of dislocations, for example, which can result in crack formation. This naturally curtails the growth of ZnO particles in the presence of dopants.

4.4.2 Excitonic properties and the Bohr radius

Exciton is a very important term and appears often in semiconductor nanocrystal analysis. The exciton often takes residence in mini-bands or entirely discrete levels in the nanocrystal when sufficient optical excitation is applied to the nanocrystal.

On the other hand, the band gap of a semiconductor is, by definition, the energy necessary to create an electron and hole at rest with respect to the lattice and far enough apart so that their Coulomb attraction is negligible. If one carrier approaches the other, they may form a bound state, also called a *Wannier exciton*. A free exciton is a bound electron – hole pair that has a binding energy of a few meV. If optical excitations are of sufficiently high frequency, they impart enough energy to ionize an electron previously in the valence band of the crystal, which allows that it jumps to the conduction band. As consequence of electron transition, a vacancy (a hole) is left behind in the position where the electron previously resided.

Such excitons, which are not spatially bound to a region smaller than their natural separation distance (the Bohr radius), are free to move within the crystal. For the free exciton, it is more appropriated to think of the e-h pair as not being

localized at all. Rather, it is more relevant to consider the exciton to be a feature of the electronic crystal, a superposition of states among all crystal atoms.

The natural separation distance (e-h) may be easily calculated by balancing the centripetal force on the electron (m_{0V_0}/r_n) to the coulombic attraction force $q^2 / 4\pi\epsilon_0 r_{ex}^2$ between the electron and its associated vacancy. Keeping in mind that via the Bohr postulate angular momentum L may be expressed mathematically as $m_{0V_0} r_n = n\hbar$, we have

$$r_{ex} = \frac{\epsilon\epsilon_0 \hbar^2}{m^* q^2} \quad (5)$$

Here for the case of an exciton in semiconductor we must replace the mass of the electron with the effective mass of the exciton.

$$m^* = \frac{m_e m_h}{m_h + m_e} \quad (6)$$

q is the electronic charge, ϵ_0 is the permittivity of free space and r_{ex} is the spatial separation of the electron and hole. The dielectric constant ϵ scale ϵ_0 accounts for the electron and hole interaction through an attractive Coulombic force, which is screened by the dielectric constant of the crystal. Using the Bohr hydrogenic model, it then follows that the energy of the excitonic bound state is given by:

$$E_{ex} = \frac{m^* / m_0}{(\epsilon / \epsilon_0)} \frac{e^2}{4\pi\epsilon_0 a_0 n^2} = \frac{13.6 m^* / m_0}{(\epsilon / \epsilon_0) n^2} eV \quad (7)$$

Where m_0 is the electron rest mass and a_0 is the Bohr radius fundamental constant

$$\begin{aligned}
 a_{exc} &= \frac{4\pi \epsilon_0 \hbar^2}{mq^2} \cdot \epsilon \cdot \left[\frac{1}{m_h} + \frac{1}{m_e} \right] \\
 &= a_{exc} \cdot \epsilon \cdot \left[\frac{1}{m_h} + \frac{1}{m_e} \right]
 \end{aligned}
 \tag{8}$$

Where m_h and m_e are the conduction band and valence band effective mass respectively. On the base of these relations we can calculate approximately the Bohr radius ($a_0 = 0.529 \text{ \AA}$). This model requires that r_{ex} (excitation distance) be large in comparison to the lattice constant of the host material. For the case of semiconductors, since they tend to have relatively small effective masses and large dielectric constants compared to insulator, it is reasonable to assume this requirement to be satisfied.

The significance of the excitonic Bohr radius is that it provides a threshold value below which the confinement regime becomes relevant. That is, excitons in a nanocrystal will no experience confinement for a spatial dimension larger than its own electron-hole spatial separation. In other words, confinement energy will not be imparted to energy levels available to the exciton unless the e-h spatial separation is reduced below the excitonic Bohr radius.

Below this threshold value begins the exhibition of quantum sizing features, such as distinct variation of density of states with nanocrystal size. Table 8 gives calculates values of excitonic Bohr radii for various semiconductor materials.

Table 8. Calculated Excitonic Bohr Radii for Various Materials

Materials	Excitonic Bohr radii (Angstroms)
Cadmium Sulfide	315
Zinc Sulfide	50
Cadmium Selenide	61
Zinc Oxide	254
Indium Antimonide	540

Quantum Confinement Effect

There has been amount of effort towards understanding the changes in the electronic properties in the structure of the material when this change of size. The physic behind the quantum size effect can be qualitatively understood as a particle-in-box model [55]. This confinement of charge carriers (electron and hole) in the restricted volume of small particle produces that the spaces in the energy levels are increased when the dimensions of the box is reduced (see Figure 32).

This simple idea (Figure 32) provides us with the basis of a qualitative understanding in the band gap with a decrease in the particle size. When the particle is confined to a limited space, its kinetic energy can only have discrete values that are determined by the mass of the particle and the dimension of the box. With this model, it can be expected that the properties of the charge carrier in solid will show a size dependence when de dimension of the solid become sufficiently small.

A quantum well is a potential well that confines particles, which were originally free to move in three dimensions, in one dimension, forcing them to occupy a planar region. The effects of quantum confinement take place when the quantum

well thickness becomes comparable at the Bohr exciton or the Broglie wavelength of the carrier (generally electrons and holes).

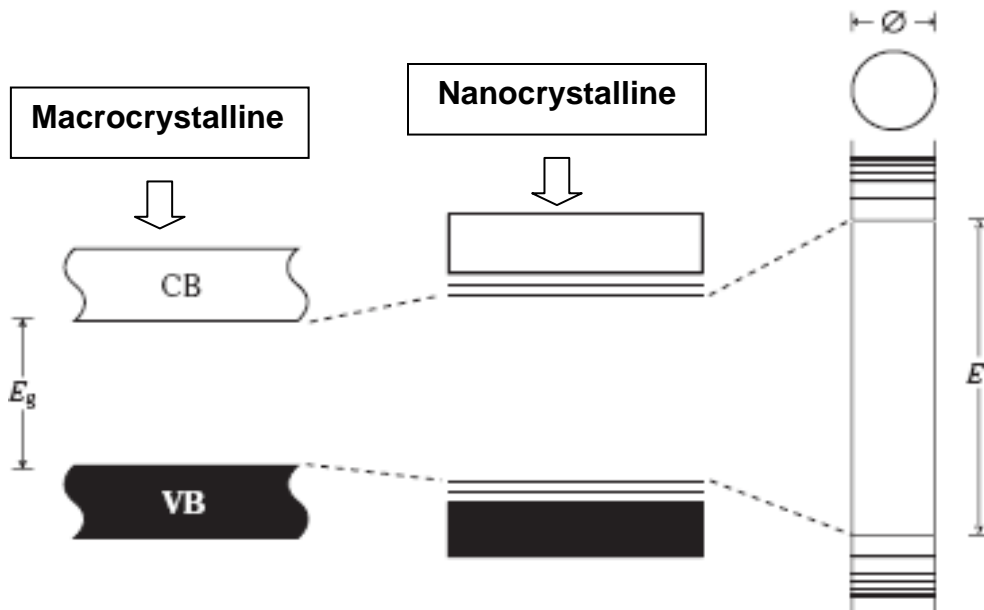


Figure 32. Representation of the gradual change of the electronic properties when the size of a semiconductor decreases (from left to right). The left correspond the energy band diagram for a microcrystalline semiconductor. The middle picture, the size of the semiconductor is comparable to the size of the exciton while the picture of the right represents the situation when de dimensions of the semiconductor are smaller than those of the exciton [51].

The particle in a box (or the infinite potential well or infinite square well) (see Figure 33) is a simple idealized system that can be completely solve within quantum mechanic. It is the situation of a particle confinement within a finite region of space (the box) by an infinite potential that exists at the walls of the box.

The particle experiences no forces while inside the box, but is constrained by the walls to remain in the box. The quantum behavior in box includes: a) energy of quantization- it is not possible for the particle to have any arbitrary definite energy. Instead only discrete definite energy levels are allowed (if the state is not a steady state), however, any energy past zero-point energy is allowed on average; b) Zero-point energy- the lowest possible energy level of the particle,

called the zero point energy, is nonzero (it is the energy ground state of the system); c) Nodes- in contrast to classical mechanics the Schrodinger's equation predicts that for some energy levels there are nodes, implying positions at which the particle can never found.

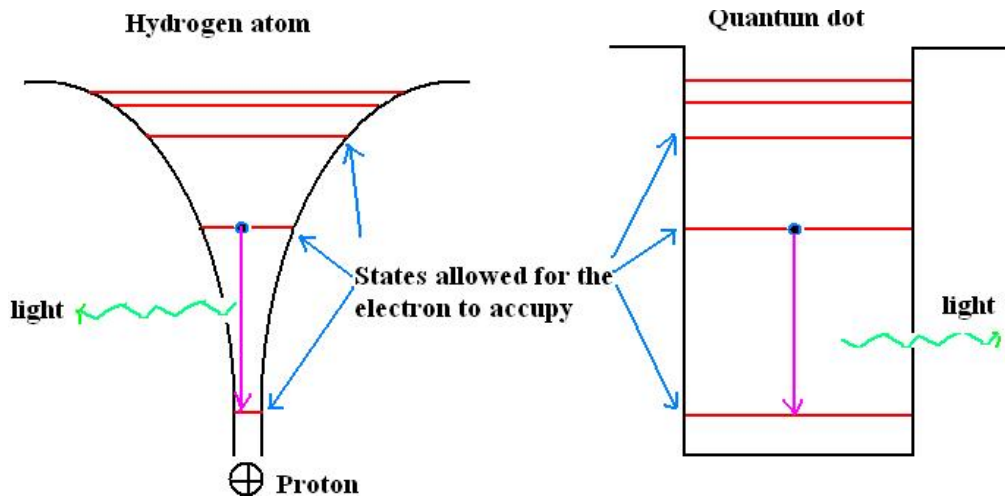


Figure 33. The quantum size confinement can be qualitatively understood like a particle-in-a-box, the energy levels spacing decreases with increasing box size. Therefore, as the number of atoms increase from a single atom or molecule to a cluster of particles of atoms and finally bulk solid, the special size of the system increases and the energy level spacing decreases.

For either a free particle or one which is confined to a periodic potential, the energy and the momentum may well-defined, but simultaneously the particle is not defined. From the well-known Schrödinger equation, energy eigenfunctions are produced through the Hamiltonian operating on the wave function. This energy Eigen's functions of the localized particle can be viewed as superposition of k states associated with the bulk. For the case of an extended solid (electron no localized), there is a definite relationship between energy and momentum the change in energy as a function of size can be estimated through the fact that the energy of the confined particle arises via superposition of bulk k state of energy.

For a free particle move through potential well in 1-D the values of the allowed energy are found by solving the Schrödinger equation and is present in the Equation (9)

$$E_n = n^2 \frac{\pi^2 \hbar^2}{2mL^2} \quad (9)$$

We can observed that the energy levels are proportional to n^2 , and separation of levels increase when n increase. The dependence of energy on well width has a direct consequence of the variation of optical properties with nanocrystal size.

4.5 SQUID CHARACTERIZATION

The magnetization curves were measured using a commercial SQUID (Superconducting Quantum Interference Device) magnetometer Quantum Design MPMS. This piece of equipment allows a base temperature of 2 K and a maximum magnetic field of 7 Tesla.

The SQUID magnetometer (Figure 34) is the most sensitive device available for measuring magnetic fields, and, although the SQUID in the MPMS is the reason for the instrument's remarkable sensitivity, it does not detect directly the magnetic field from the sample. Instead, the sample move through a system of superconducting detection coils which are connected to the SQUID unit with superconducting wires, allowing the current from the detection coils to be inductively coupled to the SQUID sensor. When properly configured, the SQUID electronics produce an output voltage which is strictly proportional to the current flowing in the SQUID input coil. Hence, the thin film SQUID device operates as an extremely sensitive current-to-voltage convector.

A measurement is performed by SQUID-MPMS by moving a sample through the superconducting detection coils, which are located outside the sample chamber and at the center of the magnet. As the sample moves through the coils, the magnetic moments of the sample induce an electric current in the detection coils. Because the detection coils, the connecting wires and the SQUID input coil form a closed superconducting loop. Then, any change of magnetic flux in the detection coils produces a change of the current in the detection circuit. This current is proportional to the change in the magnetic flux. Since the SQUID works as a highly linear current-to-voltage convector, the current variations in the detection coils produce a corresponding variation in the SQUID output voltage, which is proportional to the magnetic moment of the sample. In a fully calibrated system, the measuring of voltage variation from the SQUID detector provides a highly precise measurement of the sample's magnetic moment. The system can

be accurately calibrated using a small piece of material having a known mass and magnetic susceptibility.

SYSTEM COMPONENTS (superconducting components shown in blue)

- | | | |
|-----------------------------|---------------------------------------|--------------------------------|
| 1. Sample Rod | 8. SQUID Capsule with Magnetic Shield | 15. Console Cabinet |
| 2. Sample Rotator | 9. Superconducting Pick-up Coil | 16. Power Distribution Unit |
| 3. Sample Transport | 10. Dewar Isolation Cabinet | 17. Model 1822 MPMS Controller |
| 4. Probe Assembly | 11. Dewar | 18. Gas/Magnet Control Unit |
| 5. Helium Level Sensor | 12. HP Thinkjet Printer | 19. HP Vectra Computer |
| 6. Superconducting Solenoid | 13. Magnet Power Supply | 20. Monitor |
| 7. Flow Impedance | 14. Model 1802 Temperature Controller | |

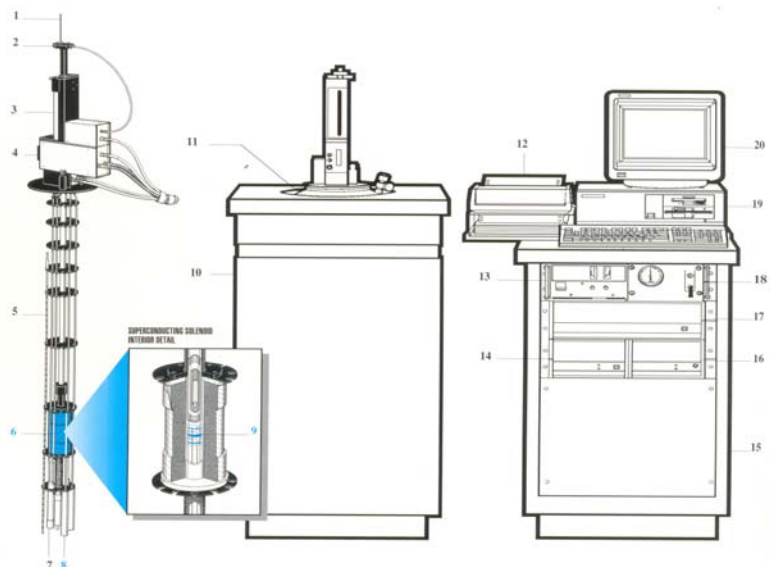


Figure 34. Components of SQUID ("Superconducting Quantum Interference Device") Quantum Design MPMS ("Magnetic Property Measurement System") Model XL5 [64]

4.5.1 M-H measurements for bare ZnO nanocrystals

Figure 35 shows the dependence of magnetization with applied magnetic field (M-H curves) for bare ZnO nanocrystals at 2 K and 300 K. A typical diamagnetic behavior was observed. The diamagnetic behavior of ZnO is due to the paired electrons of its *d* orbital, which is responsible for the absence of a permanent net magnetic moment per atom. Then, when electrons are paired together, their opposite spins cause the magnetic fields to cancel with each other. Accordingly, when an applied magnetic field is acting on this atom slightly unbalances their

orbiting electron and creates small magnetic dipoles within the atoms which oppose the applied field. This action produces a negative magnetic effect.

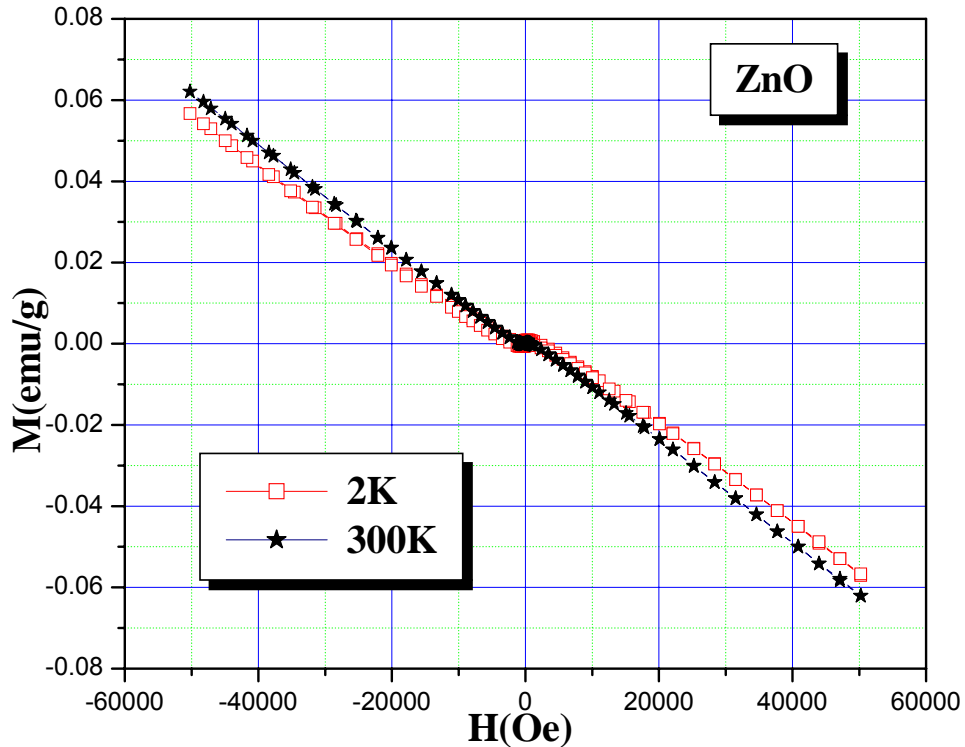


Figure 35. M vs H curves measured at 2 K and 300 K temperatures for bare ZnO nanocrystals.

4.5.2 M-H measurement for doped ZnO nanocrystals

iii) Mn-doped ZnO nanocrystals

Figure 36 shows the magnetic-field dependence of the magnetization (M versus H) at room temperature for 30 minutes ($x=0.01$) and 24-hours ($x=0.05$, 0.08) aged Mn-doped nanocrystals. The nominal atomic fractions of the dopant were 0.01, 0.02 and 0.08. Observed paramagnetic behavior can be attributed to the actual incorporation of Mn ions into the otherwise diamagnetic ZnO structure; although the precipitation of an anti-ferromagnetic phase can not be ruled out.

Though no ferromagnetic component was observed even after increasing the ‘x’ values, the paramagnetic moment increased monotonically. To establish the paramagnetic nature of our samples zero field cooled-field cooled (ZFC/FC) measurements were also undertaken for these samples. The corresponding results will be discussed latter.

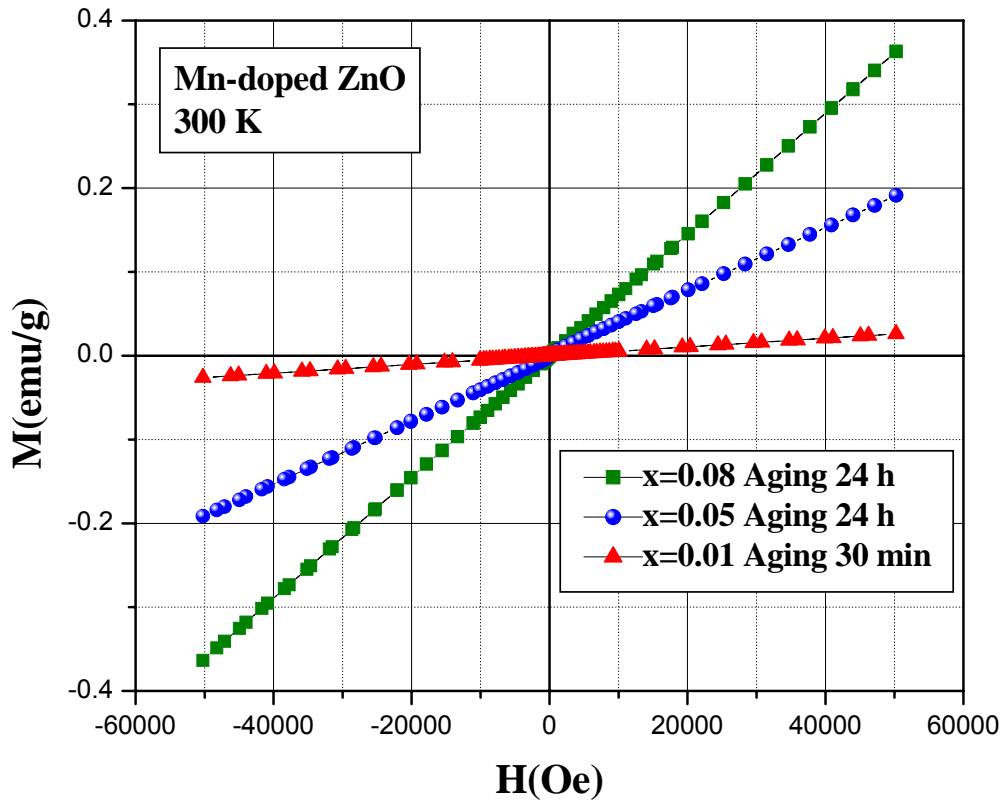


Figure 36. M-H curves at room temperature of Mn- doped ZnO nanocrystals. A linear paramagnetic behavior is observed, which could be attributed to the incorporation of the Mn atoms.

ii) Co- doped ZnO ($x=0.01, 0.02$)

As the data showed in Figure 37 indicates, the magnetic behavior of Co- doped ZnO nanocrystals was considerably different when compared to the Mn- doped ZnO system. The shape of the M-H curves for as-synthesized Co- doped ZnO at ‘x’ = 0.01 suggests a ferro- or ferrimagnetic behavior rather than a paramagnetic one. The inset in the same figure is a magnification of the M-H values around the origin and shows a small, though noticeable, coercivity

(15 Oe). It could be attributed to a weak ferromagnetism at room temperature at least for low magnetic fields. A similar behavior was observed when the Co-doped ZnO was synthesized for 'x' = 0.02 (Figure 38). In this case, a clear hysteresis loop was observed at 300 K with a coercivity field (H_c) of 120 Oe and magnetization of remanence of 4.1×10^{-4} emu/g. Also in this sample paramagnetism was predominant at higher magnetic fields. The establishment of the paramagnetism at higher magnetic fields also explains the no-saturation of the M-H curves at low fields. The small coercivity and the small area under the hysteresis loop are consistent with those reported for other ferromagnetic ZnO and nanocrystalline DMS-quantum dots [46, 47, 48, and 76].

The strong paramagnetic behavior at high fields can be attributed to the presence of magnetic dipoles located on the surface of nanocrystals that exhibited a minimum interaction with their neighbors inside of the crystal. Consequently, the interchange energy in those magnetic dipoles would be reduced increasing their freedom to get re-oriented. Therefore, since diminishing the crystal size will increase the crystal surface to crystal volume ratio, the population of dipoles ordered in the same direction will decrease. Thus, the sum of the total amount of dipoles oriented along the same direction will also decrease. In short, and from a magnetic ordering viewpoint, the crystal surface will usually be less magnetically ordered than the center of the nanocrystal.

Our results are in good agreement with those reported by Gamelin et al. [76], who synthesized ZnO-based nanocrystals by a similar route in ethanol. However, in our case all magnetic characterizations were carried out on as-synthesized nanocrystals, i.e., with no further post-treatment. Gamelin's approach involved a post-treatment of synthesized nanocrystals by the formation of core-shell structures by the isocrystalline core/shell procedure. This route involved a complete encapsulation of any surface-bound dopant by promoting the growth of pure ZnO shell around doped ZnO nanocrystals.

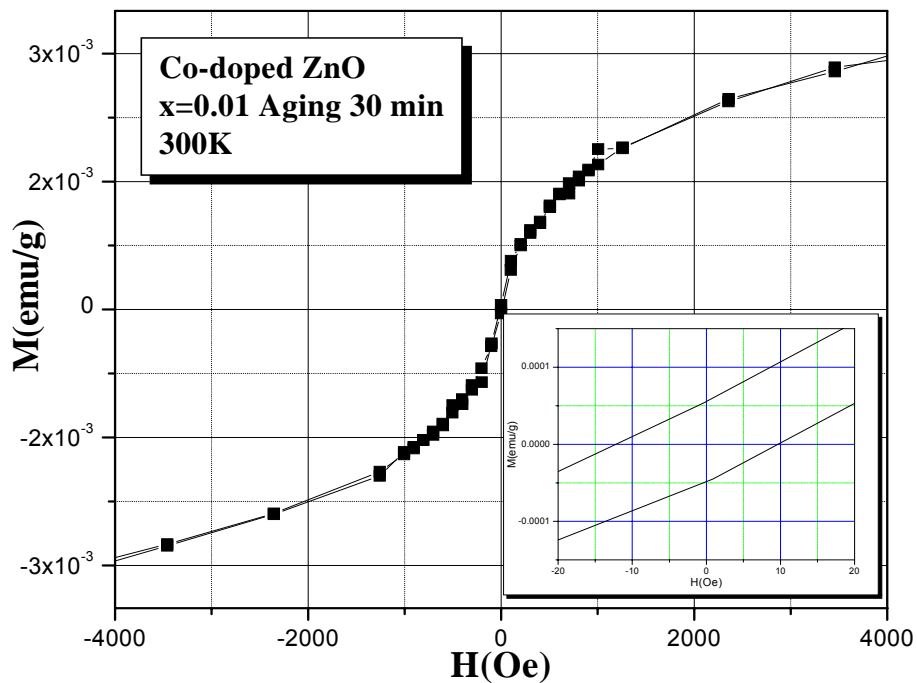


Figure 37. Room temperature M-H loop for as-synthesized Co- doped ZnO nanocrystals ($x = 0.01$, 30 min aging) at 300 K. The inset is a magnification of figure at the origin showing a small hysteresis, which suggests a weak ferromagnetism at room temperature.

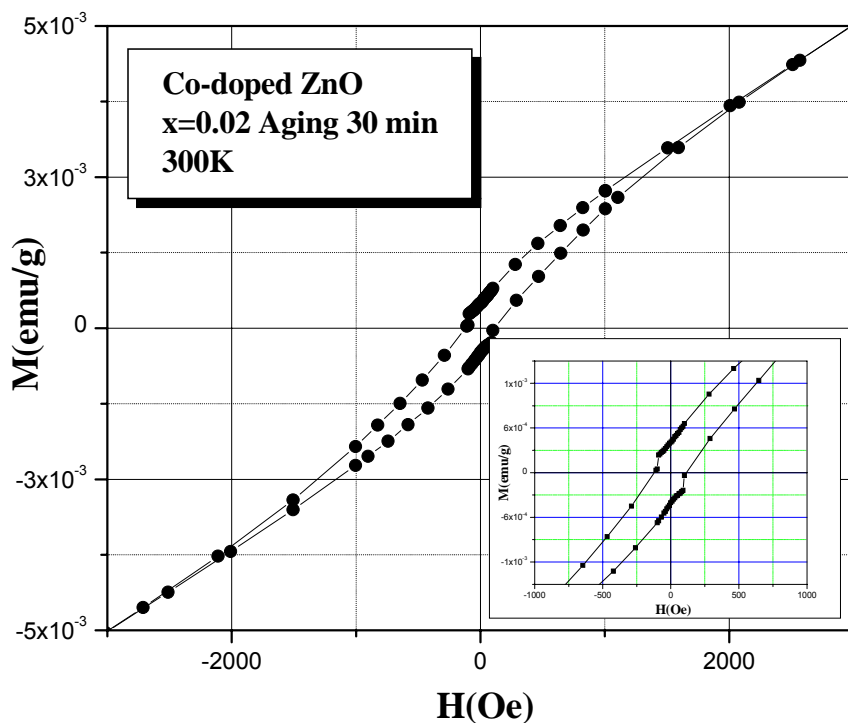


Figure 38. Room temperature M-H loop for Co- doped ZnO sample ($x=0.02$). The inset shows the M-H plot at the origin. Hysteresis is clearly observed in this curve at low magnetic fields.

On the other hand, Pearton *et al.* [37] reported an evidence for ferromagnetism with a Curie temperature of ~ 250 K in thin films ZnO co-doped with Mn and Sn. The coercivity of the 3 at. % Mn- doped sample was 250 Oe at 10 K. The corresponding value at room temperature was estimated in 50 Oe and a magnetization of saturation around 5.8×10^{-5} (emu). The same author synthesized Co- doped ZnO thin films (5 at % Co) onto (110)-oriented single-crystal Sn- doped ZnO substrates. Hysteresis was clearly observed at 5 K, with a coercivity of 300 Oe. However at room temperature, no hysteresis was observed and only superparamagnetic behavior was revealed in the magnetization versus field data. The corresponding magnetization of saturation was 1×10^{-4} (emu) a room temperature.

The origin of the ferromagnetism in Co- doped ZnO nanocrystals deserves much consideration. One of possibilities of this ferromagnetic behavior can be attributed to the formation of second phases such as CoO, but this possibility can be easily abandoned since CoO is antiferromagnetic material with small positive susceptibility having T_N of 293 K. Besides, an extra XRD peak corresponding to this compound was not detected in the corresponding patterns. Another probable cause of the weak ferromagnetism could be the presence of clusters of metallic cobalt. This possibility can be ruled out in our system since ethanol, the media in which the solid is formed, does not exhibit strong enough reducing potential to reduce cobalt (II) ions to the elemental state.

On the other hand, spinel oxides of the type Co_3O_4 can not be formed under our experimental conditions since the formation of this solid would require a partial oxidation of Co (II) into Co (III), which can not take place under our reducing synthesis conditions. Moreover, the presence of the metal cobalt was not detected by XRD even at high concentrations of Co dopants. Therefore, we can attribute the observed ferromagnetism to actual incorporation of magnetic ions into the diamagnetic ZnO host structure. In this regard, Sato *et al* [10] suggest n-type doping in ZnO, and the ferromagnetism arises from a competition

between the double-exchange interaction and the antiferromagnetic super-exchange interaction in this material. Evidently, more detailed characterization including MDC and measurement of the Hall Effect could provide additional information on this apparent intrinsic ferromagnetism at room temperature.

iii) Ni- doped ZnO (x=0.02)

Because of the extremely slow formation of the host ZnO structure in presence of Ni ions, we only characterized the Ni-doped nanocrystals synthesized for $x = 0.02$ and aged for 144 hours (when the ZnO structure was fully developed). The development of the host ZnO structure was verified by XRD and FT-IR measurements (sections 4.1.2 and 4.3 of the present thesis) for this nominal composition. Figure 39 shows the corresponding room-temperature M-H plot for the Ni- doped ZnO nanocrystals. Also in this case, a weak but evident coercivity was observed at low magnetic fields suggesting room-temperature ferromagnetism. The value of their saturation of (M_s) and H_c were 0.012 emu/g and 20 Oe, respectively.

The low magnetization and coercivity values measured for our samples can be considered typical of nanocrystalline dilute magnetic semiconductors. Radovanovic [47] suggested the formation of dense aggregates of Ni-doped ZnO nanocrystals as responsible for observed ferromagnetism. In his procedure, the synthesis was carried out at 65°C in order to accelerate nucleation and aged for two weeks at room-temperature.

Also in this case, a post-treatment of the nanocrystals consisted in their coating by ZnO was considered. The same work proposed that since colloidal nanocrystals showed no dopant mobility and appeared to be stable indefinitely under aggregation, secondary phase (e.g., NiO or Ni) could be unambiguously excluded as the source of observed ferromagnetism.

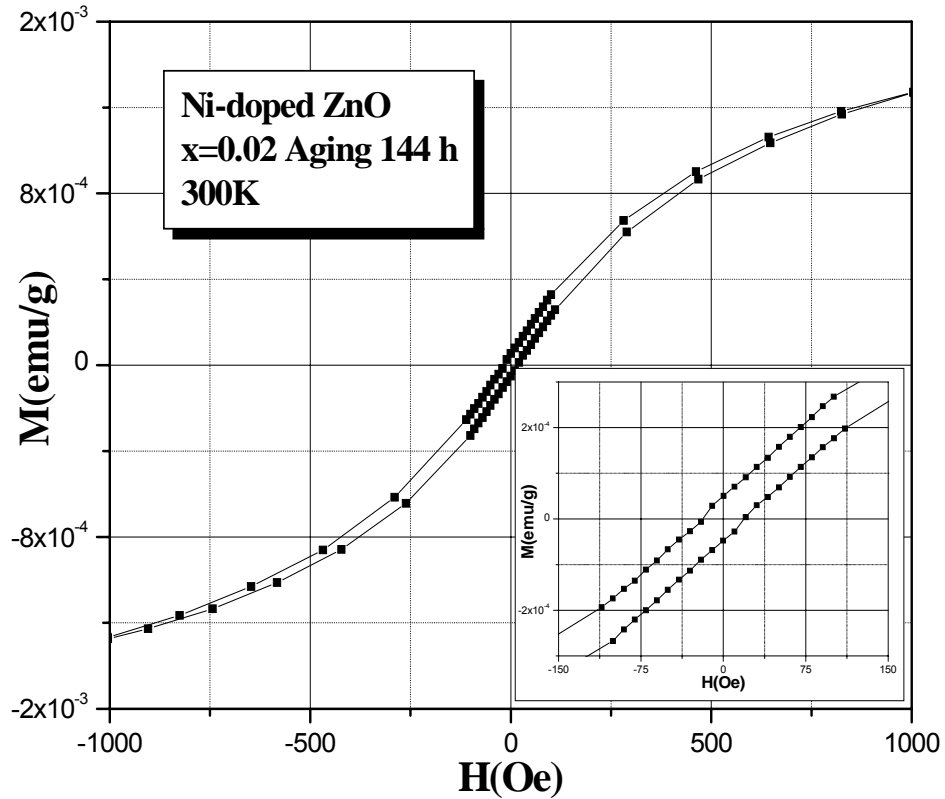


Figure 39. Room-temperature M-H curve for Ni- doped ZnO ($x=0.02$). Hysteresis is clearly observed at low magnetic fields.

On the above basis, the ferromagnetic behavior observed in our as-synthesized nanocrystals can also be attributed to aggregation of nanocrystals promoted by extremely large aging times (144 hours for $x = 0.02$) in our experiments. In agreement with Rodavonic's work, two factors can be considered essential for the conversion of paramagnetic Ni- doped ZnO into ferromagnetic structure: the increase in both domain volumes and carrier concentration [47]. Hence, observed ferromagnetism can be attributed to the generation of defects in domain volumes upon and the generation of defects at interfaces between nanocrystals and reaction-limited aggregation of the nanocrystals, which increases the carrier concentration and the generation of lattice defects upon aggregation.

iv) Cu- doped and Fe- doped ZnO nanocrystals.

Cu- doped ZnO nanocrystals

Cu doped ZnO materials have been predicted to exhibit room-temperature ferromagnetism. Because metallic copper is not magnetic, and neither Cu₂O nor CuO is ferromagnetic, Cu- doped ZnO has the possibility of being free of ferromagnetic isolated precipitates and hence form an unambiguous DMS. Initial theoretical studies carried out by Sato and Katayama-Yoshida of ZnO doped with 25% Cu predicted nonmagnetic behavior [27, 28]. However, complementary theoretical studies at lower dopant concentrations revealed that ZnO doped with 6.25% [87] and 3.125% [88] Cu should be ferromagnetic at room temperature. Those differing expectations can be reconciled by noting the proximity of the copper dopant atoms with respect to each other, in the different studies. The results of those simulations presented by [27, 28] are based on supercells that contain 8 or 16 molecules of ZnO in order to obtain the doping concentration of interest. For simulations involving 6.25% and 3.125% Cu, the nearest-neighbor copper atoms were at least 6.1 Å apart.

In Sato and Katayama-Yoshida's work (25% Cu concentration), it was necessary to place Cu atoms such that they were both above/below each other in adjacent basal planes separated by the *c*-lattice parameter constant of 5.20 Å and adjacent cationic positions within a single basal plane separated by the *a* - lattice parameter constant of 3.25 Å. Feng *et al* looked at the effect of copper separation and the stability of the ferromagnetic state in Cu-doped ZnO [89]. For the case where the copper atoms were separated along the *c*-axis with a Cu-Cu distance of 5.20 Å, the ferromagnetic state was favored, but in the other case where the copper atoms were separated by 3.25 Å within the basal plane, the antiferromagnetic state was the one to be expected. Hence, the calculations by Sato and Katayama-Yoshida may be viewed as consistent with the later theoretical calculations and mutually establishing the importance of copper-atom

placement in the doping development and replacing the suitable number of Zn atoms with Cu.

Figure 40 shows the M-H curves at 300 K for Cu- doped ZnO ('x'= 0.05, 0.08) aged for 24 hours and 96 hours, respectively. To the best of our knowledge this is the first report on magnetic properties of Cu- doped ZnO nanocrystals synthesized by solution phase route. Figure 40 evidences a clear discrepancy for a pure paramagnetic behavior, particularly at low magnetic fields, for the sample synthesized at 'x' = 0.05. A very weak coercivity was observed in this case ($H_c \sim 25$ Oe). However for a higher 'x' value, the material was exclusively paramagnetic.

Furthermore, the almost linear field dependence of magnetization within the applied magnetic field range is considered typical of an antiferromagnetic compound. As discussed above, the results from the theoretical modeling of the Cu-doped ZnO system clearly states that the location of the copper atoms relative to each other, would strongly affect the material magnetic behavior. It seems to be true even at the nanoscale. On the other hand, H. J. Lee *et al* [91] investigated the magnetic properties of bulk Cu- doped ZnO synthesized by technique.

The corresponding ferromagnetism could be explained by one of the Goodenough-Kanamori-Anderson (GKA) rules [90], which suggests the possibility of a weak ferromagnetism in the case of a 90° -exchange interaction between (half)-filled orbitals. The magnetic behavior can also be a consequence of the indirect exchange interaction through the carrier-mediated model. Generally, it has been reported that the magnetic ordering in a diluted magnetic system could be explained by the indirect exchange interaction through the spin-polarized carrier. The existence of the spin-polarized carrier in our samples could be verified by the measurement of either quantum Hall effect or magnetoresistance effect.

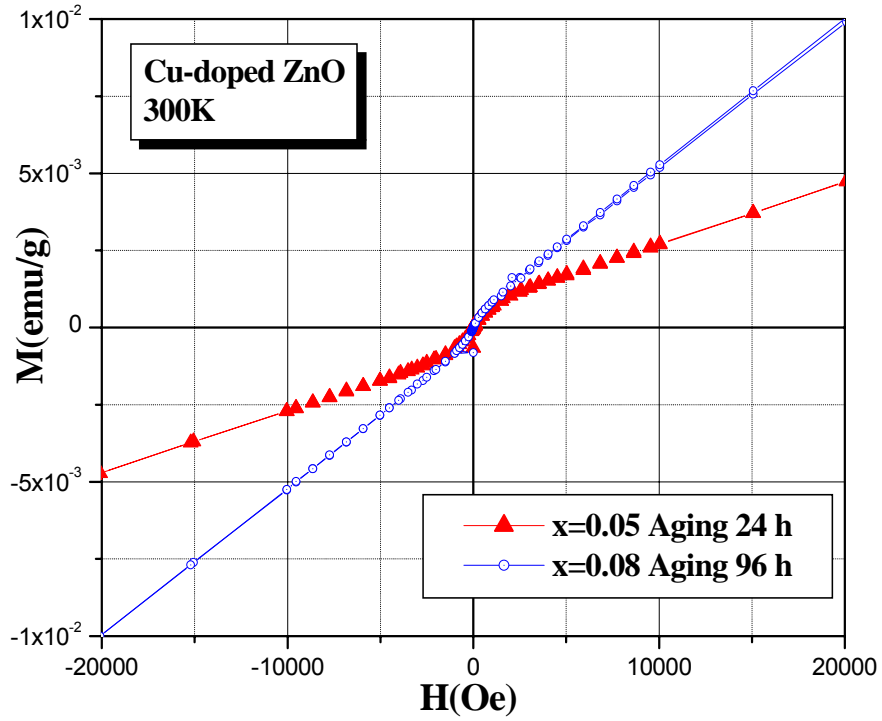


Figure 40. Room temperature M-H loops of Cu- doped ZnO ($x= 0.05$ and 0.08) aged for 24 hours and 96 hours, respectively.

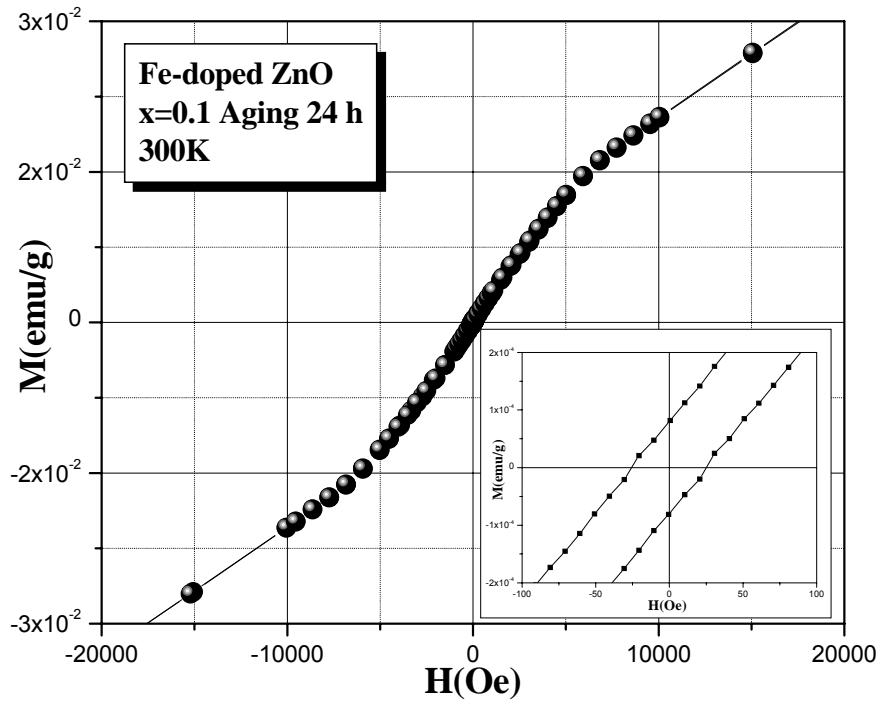


Figure 41. Room temperature M-H loop for Fe- doped ZnO ($x=0.1$). The inset shows the M-H data around the origin.

Fe-doped ZnO nanocrystals

Figure 41 presents the room temperature M-H curve for Fe- doped ZnO nanocrystals ($x=0.1$, aging time 24 hours) . Once again, a weak coercivity was observed (30 Oe), which is still above the experimental error in our SQUID system. Again, a dominant paramagnetic behavior is observed at high magnetic fields. According to Sato *et al* [27, 28], it is very likely that a $3d$ band should have been formed by Fe ions and, ferromagnetism would occur within this band via double exchange.

4.5.3 ZFC/FC for Mn- doped ZnO nanocrystals

ZFC/FC measurements were carried out for Mn-doped ZnO nanocrystals in order to get a better understanding of the paramagnetic or antiferromagnetic behavior in our materials. There are two types of measurement modes in SQUID: dc and ac susceptibility modes. The dc measurement mode can provide information on the irreversibility of the magnetic moments and can also be used to identify spin glass features. In addition, ac susceptibility measurement can help to distinguish between superparamagnetic and spin glass behavior. ZFC/FC measurements were carried out by cooling the sample down to the lowest value (4K in our SQUID unit) in absence of an external magnetic field.

Once stabilized, a magnetic field is applied (100 Oe, in our case) and operated in dc mode. The corresponding moment is measured as a function of temperature up to the highest desired temperature. Next, the sample is cooled in this same field to the lowest temperature and again measured as a function of temperature. This FC part can also be done by collecting data as the sample is cooled; however, most cryogenic systems are more time efficient when data is collected on warming [64].

The temperature dependence of magnetic susceptibility (χ) and its inverse were calculated from the ZFC measurement for three nominal concentrations of dopants (Figure 42a and 42b). These plots showed the typical behavior observed in other TM-substituted ZnO samples [68-71, 92]. The ZFC and FC curves were practically overlapped one to each other. As seen, the magnetization exhibits a drastic drop when the temperature varies from 2 K to 40 K. This trend is followed by slight diminution of the magnetization when the temperature increases from 40 up to 300 K. the plot of the inverse of magnetic susceptibility versus temperature resembled a typical Curie-Weiss behavior at high temperature.

A significant curvature in the $1/\chi$ -T profile was observed at lower temperatures. Furthermore there is a systematic variation in the high temperature magnetization with the 'x' values. The sample with smallest value (x=0.01) show larger values of $1/\chi$, and the inverse susceptibility decreases monotonically with increasing 'x' as has been observed previously [86, 91].

In order to analyze such data, we fit the high temperature inverse susceptibility-temperature data to a linear Curie-Weiss model. This approach is motivated by previous work on dilute magnetic semiconductors (DMS) [12,68] which predicts that high temperature magnetization should be follow a modified Curie-Weiss law. For a Curie-type paramagnet, there is a force that tries aligning the magnetic moment on atoms with the magnetic field. The $1/T$ (or Curie) temperature dependence is a result of a competition between the force aligning the moment parallel to the field and the tendency for heat to disrupt the alignment. As the temperature increases, the associated increase in heat reduces the relative effect of the field. What is different in a Curie-Weiss paramagnet is that, in addition to the interaction with the magnetic field, there is an interaction between the magnetic moments on different atoms. The interaction

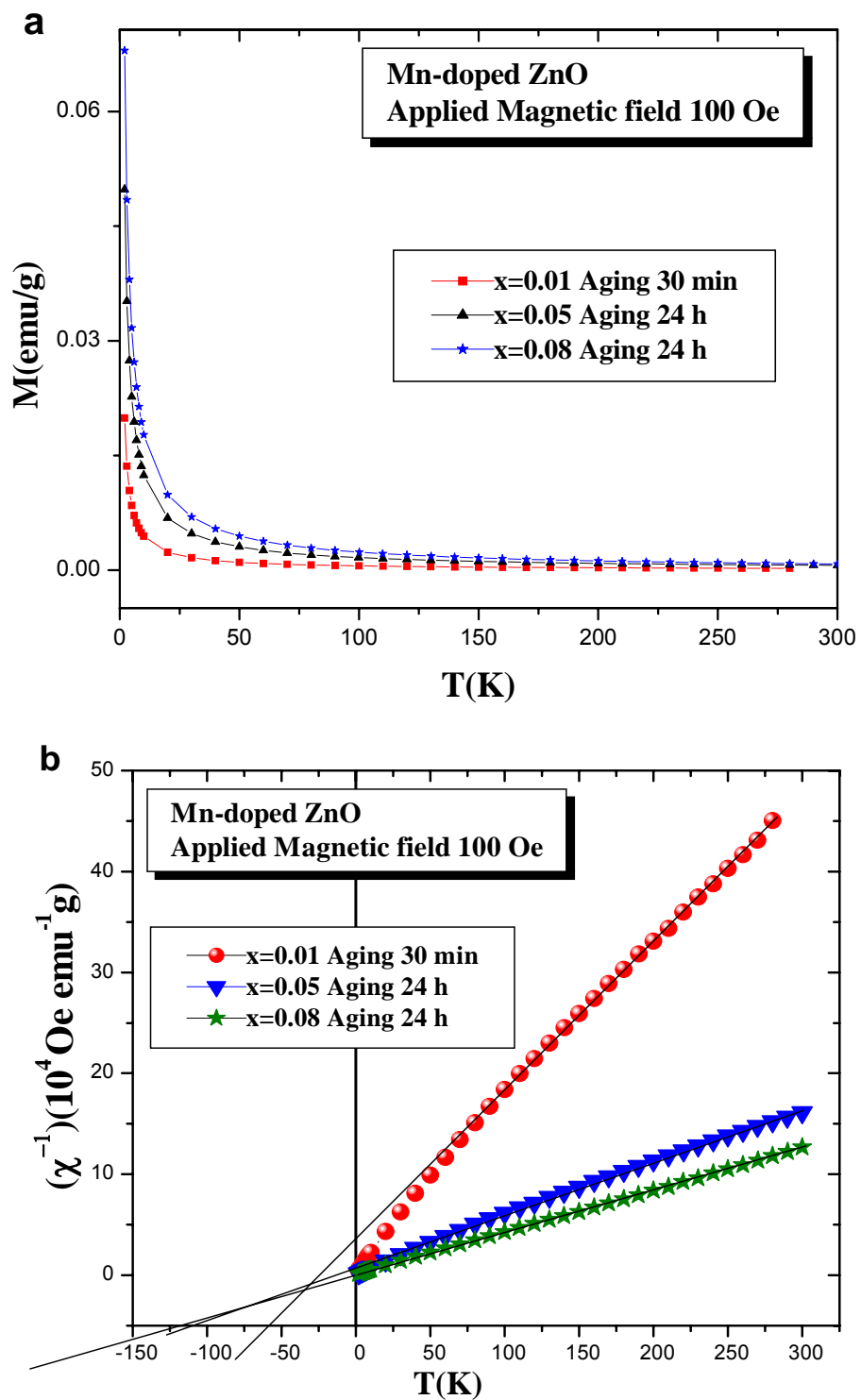


Figure 42. a) Magnetization versus Temperature curve for Mn-doped ZnO nanocrystals synthesized at different 'x' values and 100 Oe of external applied field; b) M vs T and $\frac{1}{\chi}$ vs T curves. The solid lines represent the fitting using the Curie-Weiss' law.

between moments also well-known as exchange interaction can help the alignment between adjacent moments in the same direction or it can help align neighboring moments in opposite direction. In our case, to determine the effective exchange constant between Mn-Mn atoms and assuming that Mn ions distribute randomly and interact with each other through the Heisenberg exchange $U = -2JS_i \bullet S_j$, the susceptibility χ in the high-temperature limit can be expressed as [71-72]:

$$\chi_{CW} = \frac{M}{H} = \frac{C_M(x)}{T - \Theta(x)} = \frac{C_M(x)}{T + \Theta(x)} \quad (10)$$

Where $C_M(x) = C_0x$ is the Curie is constant, which is defined as:

$$C_0 = \frac{N_{Av} (g_{eff} \mu_B)^2 S(S+1)}{3k_B} \quad (11)$$

In Equation (11), N is the number of cations per unit volume, g_{eff} is the effective gyromagnetic factor of the transition metal ion (TM), $S=5/2$ is the magnitude of the atomic spin of Mn^{2+} , k_B is the Boltzmann constant *and* in Equation 12 and $\Theta_0(x) = \Theta_0.x$, is called the Curie-Weiss temperature. Θ_0 constant is related to the exchange integral between the nearest Mn neighbor's j_1 [71].

$$\frac{2J_1}{k_B} = \frac{3\Theta}{zS(S+1)} \quad (12)$$

Where $z = 12$ is the number of nearest neighbors in the wurtzite structure of Mn- doped ZnO. The Curie temperature is related to the strength of the interaction between moments, and its sign depends on whether the interaction helps align adjacent moments in the same direction or opposite one another.

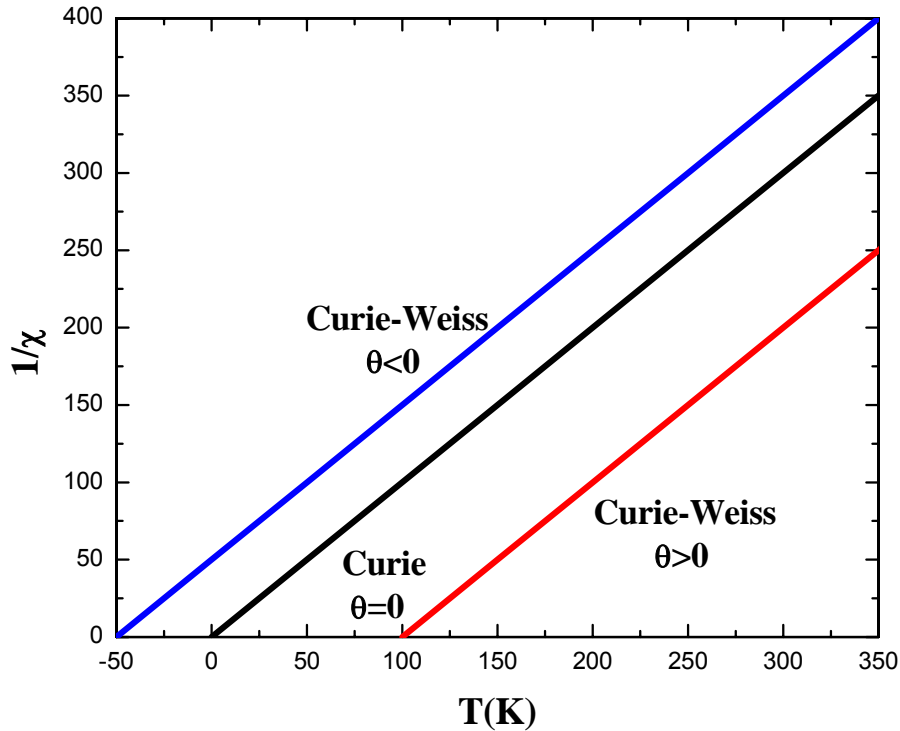


Figure 43. The inverse of χ as a function of T for systems exhibiting Curie ($\chi = C/T$) and Curie-Weiss behavior ($\chi = C/(T - \theta)$). When $\theta > 0$ the interaction between moment helps to align neighboring moment in the same direction and when $\theta < 0$ moment are aligned in opposite directions. When $\theta = 0$ the moment act completely independent of one another.

Using the definition in Equation 12, the interaction helps to align the adjacent moments in the same direction for $\theta > 0$, whereas for $\theta < 0$, the interaction helps to align adjacent moments opposite to each other. In other words, for $\theta > 0$ there will be a net ferromagnetic interaction between moments. In turn, a net antiferromagnetic interaction between moments for $\theta < 0$. In Figure 43 discusses these behaviors

In agreement with the Heisenberg model, J is the exchange integral and is related to the overlapping between charge distributions of atoms i and j . The charge distribution of a system of two spins depends on whether the spins are parallel or antiparallel according to Pauli's principle excludes two electrons of the same spin from being at the same place at the same time. It does not exclude two electrons of opposite spin. Thus the electrostatic energy of a system will

depend on the relative orientation of the spins: this difference of energy is defined the *exchange energy*.

As said before, considering nearest neighbor interaction only, the dominant exchange integral j between nearest neighbors by Equation 12, where $z = 12$ corresponding to the number of nearest neighbors in the wurtzite structure of Mn-doped ZnO a linear fit was carried out to our inverse susceptibility data in the temperature range 50 to 300 K. This linear fit, when extrapolated down to lower temperatures, intersects the $\chi^{-1} = 0$ axis at a negative temperature which indicates that interaction between Mn ions is antiferromagnetic.

In turn, the large negative value of the Curie-Weiss temperature confirms the strong antiferromagnetism exchange coupling in the Mn- doped ZnO compound which is consistent with the theory of superexchange. This result indicates the presence of antiferromagnetism interaction in the Mn- doped ZnO samples. Temperatures lower than 100 K, inverse susceptibility deviates from the linear dependence toward a temperature close to zero. This decreasing from linearity is a result of additional antiferromagnetic interaction between the next-nearest-neighbor Mn ions [68-69]. Assuming only nearest-neighbor interactions and Mn ions to be 5/2 spin state. The exchange integral values can be calculated from Equation 12. Obtained results are present in Table 9.

Table 9. Curie-Weiss parameter determined from $1/\chi$ vs. T curves for Mn-doped ZnO nanocrystals. The applied field was 100 Oe.

Dopant nominal concentration, 'x'	Curie – Weiss $\Theta(x)$	$\Theta_0(K)$	$2J_1/k_B(K)$
0.01	-56	-5600	-53.3
0.05	-112	-2232	-21
0.08	-126.4	-1580	-15

This analysis of the magnetic properties of Mn substituted ZnO revealed several features. According to the Curie-Weiss temperature values $\Theta(x)$ that the dominant spin-spin interactions are antiferromagnetic. The type (ferro-antiferro) of the magnetic interaction will depend on the Mn-Mn distances. In a random mixture of Zn and Mn ions, some Mn ions could be at a shorter distances than other, resulting in antiferromagnetic coupling; thus, increasing the Mn content will reduce Mn-Mn distances and reinforce antiferromagnetic interaction, consistent the theory of superexchange [71]. As shown in the Table 9, the absolute value of Θ_0 and $(2j/K_B)$ decrease with the manganese content, suggesting that the antiferromagnetism order of the Mn- doped ZnO are strongly weakened with the Mn content 'x'.

5. CONCLUSIONS

The present work was focused on the synthesis of highly monodisperse bare and TM-doped ZnO nanocrystals (where TM= divalent Mn, Co, Ni, Fe and Cu) in ethanol solutions at room-temperature and their structural, optical and magnetic characterization.

Preliminary results confirmed the rapid and complete formation of bare ZnO host structure at room temperature, with no need for any further annealing. The formation of the ZnO host structure was delayed when magnetic ions co-existed in starting solutions. In this case, an increase in the length of the aging period favored the complete formation of the host oxide. High resolution transmission electron microscopy (HR-TEM) verified the synthesis of a highly monodisperse system with a narrow size distribution. The nanometric size and the monodispersity of the particles were a consequence of a very fast nucleation rate in ethanol medium, coupled with a protective negative charge on the surface of nanocrystals by adsorption of acetate species. This fact was confirmed by FT-IR measurements on intensively washed samples.

UV absorption measurements for ZnO at room temperature showed the increase in particle size as a function of aging time, as evidenced from the red shift in absorption peak. UV-visible analyses also confirmed the inhibition of crystal growth when the nanocrystals were doped with transition metal ions. The variation in the band gap energy with aging time of TM-doped ZnO nanocrystals was also verified. The enhancement of the band gap energy was attributed to the strong quantum confinement of the electron at the nanoscale as well as the incorporation of dopant ion into the ZnO host structure.

SQUID measurements of as-synthesized Mn-doped ZnO nanocrystals evidenced their predominant paramagnetic behavior at room-temperature in contrast with

the diamagnetic nature of bare ZnO. The magnetic susceptibility at high temperature displayed a typical Curie-Weiss behavior. According to the Curie-Weiss temperature values, $\Theta(x)$, the dominant spin-spin interactions were of the antiferromagnetic type. This antiferromagnetic interaction was consistent with the theory of superexchange. In turn, weak, but evident coercivity was detected in Co doped ZnO nanocrystals synthesized at $x=0.01$ and aged for 30 minutes. A more robust ferromagnetism was observed in Co-doped ZnO nanocrystals for $x=0.02$. Our analysis suggests that this noticeable ferromagnetism can be attributed to actual incorporation of magnetic ions into the diamagnetic ZnO host structure. Also, Ni- doped ZnO nanocrystals exhibited weak but evident ferromagnetic behavior for a concentration of $x=0.02$ and 30 minutes of aging. Hence, observed ferromagnetism can be due to the generation of defects in domain volumes by aggregation of the nanocrystals, favored at longer aging times, which should have increased the carrier concentration. A noticeable coercivity was also reported by Cu- and Fe-doped nanocrystals. All our samples presented a strong paramagnetic behavior at high fields which can be attributed to the presence of magnetic dipoles located on the surface of nanocrystals that exhibited a minimum interaction with their neighbors inside of the crystal. Consequently, the interchange energy in those magnetic dipoles would have been reduced and their freedom to get re-oriented, promoted.

6. REFERENCES

- [1] Ohno. F. Matsukura and Y. Ohno. JSAP International. Vol 5 (2002), 4
- [2] S.J. Pearton, C.R. Abernathy, D.P. Norton, A.F. Herbard, Y.D. Park, L.A. Boather, J.D. Baudai, Mat Sc. And Engg., Vol R40 (2003),137
- [3] S. Das Sarma, American Scientist, Vol 89 (2001) 516
- [4] H. Ohno, Science, Vol 281 (1998), 951
- [5] Mauger A and Godart C 1986 *Phys. Rep.* 141 51
- [6] R. Janisch, P. Gopal and N. A. Spaldin. *J. Phys: Condens Matter* Vol 17 (2005) R657-R689.
- [7] H. Ohno, Science, Vol 281 (1998), 951
- [8] H. Ohno, H. Munekata, T. Penney, S. von Molnar, L. L. Chang, *Phys. Rev. Lett.* Vol 68 2664 (1992).
- [9] H. Ohno, A. Shen, F. Matsukura, A. Oiwa, A. Endo, S. Katsumoto and Y. Iye, *Appl. Phys. Lett.* Vol 69 363 (1996).
- [10] H. Katayama-Yoshida, K Sato / *Jpn. J. Appl. Phys B* 39 (2000) L555.
- [11] [11] T. Dietl, H. Ohno, F. Matsukura, J. Cibert. & D. Ferrand, *Science*, Vol 287 (2000), 1019
- [12] Furdyna J. K. 1988 *J. Appl. Phys.* 64 R29-R64 (1988)
- [13] J.H. Kim, H. Kim, Y.E. Ihm, & W.K. Choo, *J. Appl. Phys.*, Vol 92, (2002). 6066
- [14] P. Sharma, K. Sreenivas, and K. V. Rao, *J. Appl. Phys.*, Vol 93, (2003) 3963
- [15] S.N. Khanna, B.K. Rao, P. Jena, M. Knickelbein, *Chemical Phys. Letts.*, 378 (2003) 374
- [16] S.J. Pearton et al. / *Physica B* 340–342 (2003) 39–47
- [17] M. Baibich, J. Broto, A. Fert, F. v. Dau, F. Petroff, P. Etienne, G. Greuzet, A. Friederich, and J. Chazelas, “Giant Magnetoresistance of (001)Fe/(001)Cr Magnetic Superlattices,” *Phys. Rev. Lett.* Vol 61, 2472 (1988).
- [18] G. Binash, P. Grunberg, F. Saurenbach, and W. Zinn, “Enhanced Magnetoresistance in Layered Magnetic Structures with Antiferromagnetic Interlayer Exchange,” *Phys. Rev. B.* Vol 39, 4828 (1989).
- [19] . S. S. P. Parkin, Z. G. Li, and D. J. Smith, “Giant Magnetoresistance in Antiferromagnetic Co/Cu Multilayers,” *Appl. Phys. Lett.* Vol 58, 2710 (1991); S. S. P. Parkin, R. Bhadra, and K. P. Roche, “Oscillatory Magnetic Exchange Coupling Through Thin Copper Layers,” *Phys. Rev. Lett.* Vol 66, 2152 (1991).
- [20] B. Dieny, V. S. Speriosu, S. S. P. Parkin, and B. A. Gurney, “Giant Magnetoresistance in Soft Ferromagnetic Multilayers,” *Phys. Rev.* Vol B 43, 1297 (1991).
- [21] S. A. Wolf, A. Y. Chtchelkanova, D. M. Treger, *IBM Journal of Research and Development. Spintronic* Vol 50 Number 1, 2006
- [22] <http://www.pcguides.com/ref/hdd/op/heads/techGMR-c.html>
- [23] Datta and Das, *Appl. Phys. Lett.*, Vol 56, (1990) 665
- [24] Zutic, J. Fabian, S. D. Sarma. *Reviews of Modern Physics.* Vol 76, 2004.

- [25] Dietl T, Ohno H, Matsukura F, Cibert J and Ferrand D 2000 Science 287 1019.
- [26] Dietl T, Ohno H, Matsukura F Phys Rev B, Vol 63, 195205
- [27] K Sato and Katayama-Yoshida Semicond. Sci. Technol. 17 (2002) 367-376
- [28] K Sato and Katayama-Yoshida, Physica B 308-310 (2001) 904-907
- [29] Ü. Özgür, Ya. I. Alivov, C. Liu, A. Teke, M. A. Reshchikov, S. Doğan, V. Avrutin, S. –J. Cho, and H. Morko J. Appl. Phys. Vol 98, 041301 (2005).
- [30] T. Fukumura, Z. Jin, A. Ohtomoto, H. Koinuma, M. Kawasaki. Appl. Phys. Lett., vol 75 (1999), 3366.
- [31] T. Fukumura, Z. Jin, M. Kawasaki, T. Shono, T. Hasegawa, S. Koshihara, and H. Koinuma., Appl. Phys. Lett., vol 78, 958 (2001).
- [32] H-W. Zhang, E-W. Shi, Z-Z. Chen, X-C. Liu, Bing Xiao., Vol 137 272-274 (2006).
- [33] X. M. Cheng and C. L. Chien., J. Appl. Phys. Vol 93, 7876 (2003).
- [34] K. Ueda, H. Tabata, T. Kawai. Appl. Phys. Letters, Vol 79, 988-990 (2001)
- [35] R. K. Zheng, H. Liu, and X. X. Zhang, V. A. L. Roy, A. B. Djurišić. Appl. Phys. Letters. Vol 85, 2589-2591 (2004).
- [36] S. W. Jung, S. –J. An, and Gyu- Chul Yi. Appl. Physic. Letters, vol 80, 4561-4563 (2002).
- [37] Y. W. Heo, M. P. Ivill, K. Ip, D.P. Norton, S. J. Pearton, J. G. Kelly, R. Rairigh, A. F. Hebard, T. Steiner., Appl. Phys. Letters, Vol 84, 2292-2294, (2004).
- [38] N. Theodoropoulou, G. P. Barera, V. Misra, P. LeCalir, J. Philip, J. S. Moodera, B. Satapi, and T. Som (unpublischted).
- [39] L. Yan, C. K. Ong, X. S. Rao., J. Appl. Phys., Vol 96, 508-511 (2004)
- [40] Gamelin et al J. Am. Chem. Soc., Vol 126, 9387-9398 (2003)
- [41] J. H. Kim, H. Kim, D. Kim Y. E. Ihm, W. K. Choo. J. Appl. Phys. Vol 92, 6066-6071 (2002)
- [42] H. J. Lee and S-Y. Jeong, C-R. Cho, C-H. Park. Appl. Phys Letters. Vol 81, 4020-4022 (2002)
- [43] D. P. Norton, *et al.*, Appl. Phys. Letters, Vol 83 5488-5490.
- [44] K. Ando, H. Saito, Zhengwu Jin, T. Fukumura, M. Kawasaki, Y. Matsumoto, H. Koinuma., J. Appl. Phys., Vol 78, 2700 (2001).
- [45] Z. Jin et al., J. Appl. Phys., Vol 78, 3824-3826 (2001).
- [46] Tawari, C. Jin, A. Kvit, D. Kumar, J. F. Muth, J. Narayan. Solid State Comm., Vol 121, 371 (2002).
- [47] P. Radovanovic, and D. Gamelin., Phys. Rev. Lett Vol 91, 157202-1 (2003)
- [48] D. Schwartz, N. S. Norberg, Q. P. Nguyen, J. M. Parker, and D. Gamelin., J. Am. Chem. Soc. Vol 125, 13205-13218 (2003).
- [49] L. Spanhel, M. Anderson., J. Am. Chem. Soc. Vol 113, 2826-2833, (1991)
- [50] H. Zhou *et al.* Appl. Phys. Lett. Vol 80, 210-212, 2002
- [51] Meulenkamp, E. A. J. Phys. Chem. B. Vol. 102, 5566-5572, (1998)
- [52] J. Daniel Bryan, D. A. Schwartz, and D. Gamelin. J. Nanotechnology
- [53] E. Hosono, S. Fujihara, T. Kimira and H. Imai, J. Sol-Gel Science and Technology, Vol 29, 71-79, 2004
- [54] N. Yao, Z. L. Wang, "Handbook Microscopy for Nanotechnology", p 427
- [55] L. E. Brus, J. Chem. Phys. Vol 79, 5566 (1983)

- [56] L. E. Brus, J. Chem. Phys. Vol 80, 4403 (1984)
- [57] L. E. Brus, J. Chem. Phys. Vol 90, 2555 (1986)
- [58] Y. Kayanuma, Phys. Rev. B, Vol 42, 7253 (1990)
- [59] Al. L. Efros and A. L. Efros, Sov. Phys. Semicond. Vol 16, 772 (1982)
- [60] S. Monicone, R. Tufeu, and A. V. Kanaev. J. Phys. Chem. B. Vol 102, 2854-2862 (1998)
- [61] N. S. Pesika, Z. Hu, K. J. Stebe and P. Searson. J. Phys. Chem. B. Vol 106, 6985-6990 (2002)
- [62] N. S. Pesika, K. J. Stebe and P. Searson, Adv. Mater. Vol 15, 1289-1291 (2003)
- [63] J. E. Raynolds, M. LoCascio. IEEE J. of Quantum Electronics (submitted)
- [64] MPMS XL-7 Quantum Design SQUID Manual
- [65] Berger, L. I. Semiconductor material; Shionoya, CRC: Boca Raton, FL, 1997; p.184
- [66] Sze, Physics of Semiconductor Device; Wiley: New York 1981 p.184
- [67] S. Shionoya in Phosphor Handbook; Shionoya, S.; Yen, W. M., Eds.; CRC: Boca Raton, FL, 1997
- [68] J. Spalek, A. Lewicki, Z. Tarnawski, J. K. Furdina, R. R. Galazka, and Z. Obuszko, Phys. Rev B Vol 33, 3407 (1986).
- [69] A. Lewicki, J. Spalek, J. K. Furdina, , R. R. Galazka, Phys. Rev. B. Vol 37 1860-1863 (1988)
- [70] S. W. Jung, S. J. An, G. C. Yi, C. U. Jung, S. I. Lee, and S. Cho, Appl. Phys. Lett. Vol 80, 4561 (2002).
- [71] J. Spalek, A. Lewicki, Z. Tarnawski, J. K. Furdina, R. R. Galazca, and Z. Obusko, Phys. Rev. B Vol 33, 3407 (1986)
- [72] C. Kittel, Introduction to Solid State Physics, Eighth edition, p324
- [73] E. Kisi and M. M. Elcombe, Acta Crystallogr., Sect. C: Cryst. Struct. Commun. Vol C45, 1867 (1989)
- [74] H. Saeki, H. Tabata and T. Kawai, Solid State Commun. Vol 120 (2001) 439
- [75] T. Wakano, N. Fujimura, Y. Moriga, N. Abe, A. Aschida and T. Ito *Physica E* Vol 10, 260 (2001)
- [76] D. A. Shwartz, K.R Kittilstved and D. R. Gamelin, Appl. Phys. Lett. Vol 85, 1395 (2004)
- [77] Y. Cho, W. K. Choo, H. Kim, D. Kim and Y. E. Ihm, Ibid Vol 80, 3358 (2002)
- [78] S. J. Han, J. W. Song, C. – H. Yang, S. H. Park, J. –H. Park, Y.H. Jeon and K. W. Rhie, Appl. Phys. Lett. Vol 81, 4212 (2002)
- [79] J. Shim. T. Hwang, S. Lee, J. Park, S. Han and Y. H Jeong, Appl. Phys. Lett. Vol 86, 082503 (2005).
- [80] Y. Matsumoto, Science Vol 291, 854 (2001).
- [81] Y. Matsumoto, *et al.* Japan J. Appl. Phys. Vol 40 L1204.
- [82] Chamber *et al.* Appl. Phys. Lett. Vol 79 3467.
- [83] D. H. Kim *et al.* 2003 J. Appl. Phys. Vol 93 6125.
- [84] D. H. Kim *et al.* 2003 Phys. Rev. Lett. Vol 90 017401.
- [85] Shinde *et al.* Phys. Rev. B Vol 67, 115211 (2003).
- [86] A. S. Risbud *et al* PHYSICAL REVIEW B Vol 68, 205202 ~2003
- [87] M. S. Park and B. I. Min, Phys. Rev. B Vol 68, 224436 (2003)

- [88] C.-H. Chien, S. H. Chiou, G. Y. Gao, and Y.-D. Yao, *J. Magn. Magn. Mater.* Vol 282, 275 (2004).
- [89] X. Feng, *J. Phys.: Condens. Matter* Vol 16, 4251 (2004).
- [90] J. B. Goodenough, *Phys. Rev.* 100, 564 (1955).
- [91] Hyeon-Jun Lee¹ *et al* *phys. stat. sol. (b)* 241, No. 7, 1533–1536 (2004)
- [92] Luo *et al.* *J. Appl. Phys.* Vol 97 086106 (2005).
- [93] A. R Denton, N. M. Ashcroft. *Phys Rev A.* Vol 43. 3161-3164